Fabrication of Low-cost perovskite-based solar cells that use recycled lead and lead compounds from depleted sealed-lead acid batteries

By

Malevu, Thembinkosi Donald
(M.sc)

A thesis submitted in fulfilment of the requirements for the degree

PHILOSOPHIAE DOCTOR

in the

Faculty of Natural and Agricultural Science
Department of Physics

at the

University of the Free State
Republic of South Africa

Promoters

R.O Ocaya and Dr. K.G Tshabalala

April 2018

DECLARATION

I hereby declare that the work contained in this thesis is entirely my own and where necessary credit is given to materials and sources that have been referred to.

Dedicated to my family

Acknowledgements

Pursuing this study has been an exciting and enjoyable journey largely due to the good support I have received. Many credits go to various individuals for their efforts, even though they are not mentioned directly. I am grateful for the support and knowledge that I have gained over the last two years.

First of all I would like to pay my appreciation to my promoters Dr. R.O Ocaya and Dr K.G Tshabalala, for their patient guidance, support and constant encouragement. I have been astonished to have such mentors who gave me a room to explore things on my own way and at the same time the guidance to recover when my steps faltered.
I hope that one day I would become a good promoter to my students as you have been to me. Thank you R.O Ocaya once again for always being there for me, listening and giving me brotherly advice. I reflect back on brotherly advice you gave me during my honors studies (14 March 2011) when I wanted to quit because of financial and background implications. On that day, you showed so much faith and "prophecy " over my future. I would also like to thank my parents K.M Malevu, S.N Hlatshwayo and J.J Malevu, my daughter Lubambo Malevu for their valuable support, love and understanding. I would also like to thank all my current and previous staff and students of the Departments of Physics and Chemistry, particularly Dr L.F Koao, Dr S.V Motloung, Dr N Debelo, Dr L Tesfaye, Dr M, Winfred, S.J Motloung, M Lephoto, J Ungula, M Lebeko, and C Clarke for all assistance rendered. B.S Mwankemwa from UP, brother, I am very grateful for your encouragement, for numerous discussions on related topics that helped me improve my knowledge in the area of solar cells and most important I am more thankful about the sleepless night you took just to be with me in the laboratories you are a man in need and a man indeed.

It would not have been possible to carry out this research without the financial support of the NRF-DST Innovation Grant No. 94944, Thuthuka Post-PhD grant No. UID99378 and the University of the Free State for financial support.

Many thanks go to the NRF-DST for nominating me at the *Research Excellence Nomination of Next Generation Researcher 2017* .

Above all to the Lord, God. May your Name always be praised.

Table of Contents

List of Figures

List of Tables

Abstract

Perovskite solar cells have been found as promising candidates to offset carbon emissions while providing an alternative way to meet increasing demand in energy consumption. In this thesis, we have successfully fabricated perovskite-based solar cell using cheaper materials and environmentally friendly methods. The investigation of these perovskite solar cells covers the operation starting from Synthesis and characterization of high-quality PbI_2 nanopowders from depleted sealed acid batteries. On the other hand, synthesis and characterization of the nanocrystalline TiO_2 and CH_3NH_3I compounds are also carried in fabricating the perovskite solar cells. By utilizing the proposed method, we possibly find alternative ways of improving the power efficiency of the existing solar cells fabricated in ordinary atmospheric conditions. A high-quality lead iodide (PbI_2) nanoparticles were synthesized from both anode and cathode of a discarded sealed lead-acid accumulator as starting materials. The structure, morphology, chemical composition and optical properties of washed PbI_2 were investigated using X-ray diffraction, field emission scanning electron microscope, photoluminescence and energy-dispersive X-ray spectrometer. The XRD measurements indicated the presence of pure hexagonal PbI_2 nanoparticles. Application of the Scherrer equation indicates crystal sizes between 13.70 and 14.32 nm. SEM indicated the presence of spherical particle agglomerations between 1.50 and 3.50 μm in diameter. The measured band gap using two methods (cathode and anode) was consistent at 2.75 eV. EDS results suggest the absence of impurities in the synthesized nanoparticles. The overall results suggest that discarded sealed lead-acid accumulators can source pure hexagonal-phase lead iodide nanoparticles with potential applications in perovskite solar cells. By investigating the effects of annealing time and post-melting temperature

on the structure and optical properties of synthesized product it was found that PbI_2 nanoparticles consist of the rare 6R polytype which has never been evaluated for a potential applications in photovoltaic. Subjecting this 6R polytype PbI_2 nanoparticles to temperatures higher than the melting point a phase transformation was observed through XRD peaks and the various changes on stoichiometries gave interesting future directions in attempts to enhance solar cell performance. Furthermore, high-quality TiO_2 nanocrystals were successfully synthesized using hydrothermal method. The as-prepared samples were subjected to a subsequent annealing at temperatures (AT) ranging from 200 to 600 ^oC to investigate the effect of AT on the structure, morphology and optical properties of TiO_2 nanocrystals. XRD as well as Raman studies suggested the presence of anatase and rutile phases with no traces of other TiO_2 phases such as brookite or srilankite as confirmed by Raman Spectroscopy. SEM showed that the preferred facet for TiO_2 nanaocrystals at high temperature is (101) and (001) facet and selected area diffraction (SAED) patterns confirmed high crystal quality of the synthesized TiO_2 and are monocrystalline. PL data showed three main emission peaks appear at about 407, 416 and 493 nm which are attributed to photoexcited electronhole pairs, band-edge free excitons and bound excitons and oxygen vacancy defects, respectively. UV-Vis data showed a decrease in the band-gap from 3.08 to 2.73 eV over the 400–600 ^{o}C temperature range.

In diode device: To evaluate 6R polytype PbI_2 nanoparticles contribution in photovoltaic applications, two sets of devices were fabricated i.e diodes and solar cells. A comparison between 6R polytype and common 12R polytype were made. Current–Voltage measurements for both samples show good rectifying behavior of the resulting heterogeneous Schottky diodes. The ideality factors and barrier heights were found to be 4.07/4.09 and 0.500/0.496 eV for the 6R/12R polytypes, respectively. The 6R polytype devices appeared to show improved I-V characteristics in comparison to the 12R polytype thus suggesting an avenue to enhance the performance of $MAPbX_3$ pevoskite devices.

In solar cells: A perovskite solar cells based on TiO_2 nanocrystalline was prepared and its photovoltaic performance as a function of annealing

temperature was investigated. The optical properties and morphology of the perovskite films were correlated with changes in device performance. It was shown that device efficiency is strongly dependent on annealing temperature. Increasing annealing temperature of perovskite films from 60 ^oC to 100 ^oC led to agglomeration of perovskite island in perovskite films, thus increasing the efficiency of the cells from 1.59 % to 2.63 %. At the optimal temperature of 100 ^oC, ITO/TiO_2/$CH_3NH_3PbI_3$/PDOT:PSS/Ag solar cell was found to have a power efficiency of 2.62 %.

Chapter 1

Introduction

1.1 Overview

The technology of photovoltaics (PVs), whereby energy from the sun is converted into electricity, offers the possibility of a clean source of electricity without the pollution concerns of gas or coal-fired power stations, or the safety concerns associated with nuclear energy. Photovoltaics, the direct generation of electricity from sunlight, is one of the technologies that can contribute to reduction of carbon emissions from fossil-based energy sources paving the way to clean energy production. PV is predicted to be able to contribute 11% towards global electricity production by the year 2050 [6]. This can only be achieved if all existing PV technologies are further improved and new technologies are developed.

The excessive cost of conventional solar cells based on inorganic semiconductors has however prohibited this technology from having a significant impact on global energy production. Although crystalline silicon and multijunction gallium based solar cells have demonstrated efficiencies of up to 25% and 32% respectively [7], there are several key processes involved in the operation of an organic–inorganic solar cell. These include light absorption, charge separation, and charge transport [8]. By investigating each of these processes individually, a more detailed knowledge of the materials and how they function in an

organic–inorganic solar cell may be obtained. The material must absorb solar radiation efficiently and therefore a detailed investigation of the absorption spectrum of the material is required [9]. Charge separation may be investigated using various techniques including photoluminescence quantum yield [10] and light-induced electron paramagnetic resonance [11], whilst current-voltage and electrically detected magnetic resonance measurements advance understanding of the device as a whole.

Two promising emerging technologies for PV electricity generation are organic–inorganic photovoltaics (OPV) and dye-sensitized solar cells (DSCs), devices which can potentially be produced at low–cost. They have already entered the market in niche applications [12]. Compared to traditional silicon-based or other inorganic solar cells, both OPV and DSCs have the advantages of material diversity, abundance, and open up the possibility of printing and large-scale fabrication even on flexible substrates. Moreover, their low weight and low material consumption, as well as a less energy-intensive production, can lead to low production costs and short energy payback times of less than a year. Additional advantageous features of OPV or DSCs are a broad scope for design, with the ability to modify aspects such as transparency and color [13]. Furthermore, DSCs are promising for indoor or diffuse light applications, as the devices exhibit higher efficiencies under diffuse and weak illumination than silicon-based solar cells.

The use of abundant and non-toxic materials is advantageous, especially compared to inorganic thin film CdTe or copper indium gallium (di)selenide (CIGS) solar cells. However, the efficiencies and stability of OPV and DSCs are still major drawbacks compared to conventional inorganic PV technologies, and at present, they do not compete commercially. Liquid electrolyte DSCs have the problem that, apart from the stagnation of the already rather high efficiencies (10 %) since they were first introduced, due to the use of corrosive and volatile iodide based electrolytes, the devices need to be sealed leading to

increased costs for substrates and encapsulation. This leaves little financial scope to achieve competitive prices per Watt-peak. However, we have recently witnessed a breakthrough in highly efficient solar cells, where the solution-processable semiconducting organolead halide perovskite, $CH_3NH_3PbI_3$, was used as an absorber of sunlight. The perovskite was used to sensitize mesoporous TiO_2 films in a solid state mesoscopic solar cell to deliver a power conversion efficiency (PCE) of up to 12.3% [14]. More importantly, they have been shown to exhibit ambipolar transport, allowing them to replace the hole or electron transporter in hybrid cells, making this family of materials suitable for solution-processable thin-film solar cells [15]. Particularly, the perovskite $[CH_3NH_3PbI_3]_xCl_x$ has been demonstrated to function in a thin-film architecture, with a layer of bulk crystalline perovskite formed over a mesoporous alumina scaffold [16]. A short period later, mesoporous Al_2O_3 was employed as a scaffold to support the formation of continuous thin films of a mixed halide perovskite, $[CH_3NH_3PbI_3]_xCl_x$, to form nonsensitized solar cells. This so-called meso-superstructure perovskite solar cell had a PCE as high as 10.9% [17].

In this thesis, we concentrate on the fabrication of perovskite-based solar cell using cheaper materials and environmentally friendly methods. The investigation covers the operation of these solar cells starting from the basic theory up to the estimation of the power efficiency that this solar cells can produce. By utilizing the proposed method, we can possibly also find alternative ways of improving power efficiency of the existing solar cells as well and thus provide cheap, high performing cells that can meet the tremendous population growth.

1.1.1 Aims and objectives

This project was conducted to evaluate the fabrication of perovskite-based solar cells that use recycled lead and lead compounds from depleted sealed-lead acid (SLA) batteries. The objectives of this study are:

1. To synthesize and characterize high-quality PbI_2 nanopowders from depleted SLA accumulator anode and cathode.
2. To evaluate phase transformations of high-purity PbI_2 nanoparticles before they can be used in solar cell.
3. To examine thermal stability CH_3NH_3I and PbI_2 as perovskite solar cell precursors.
4. To synthesize and characterize nanocrystalline TiO_2.
5. To investigate the effect of annealing temperature of nanocrystalline TiO_2 for solar cell application.
6. To investigate the effect of 6R and 12R lead iodide polytypes on $MAPbX_3$ in perovskite device performance.
7. To fabricate and characterize perovskite solar cells.
8. To study the effect of annealing temperature on $MAPbX_3$ perovskite solar cell performance fabricated in ambient atmosphere

1.2 Outline of the thesis

1. *Chapter 2*: This chapter provides the literature review of Organic–inorganic solar cells. Detailed information about generation of solar cells, device architecture, structure of perovskite and physics behind characterization of photovoltaic solar cells.

2. *Chapter 3*: This chapter gives and overview of standard characterization methods and device fabrication.

3. *Chapter 4*: In this chapter, a detailed method on how to synthesize and characterize high-quality PbI_2 nanopowders from depleted SLA accumulator anode and cathode is provided.

4. *Chapter 5*: This chapter present phase transformations of high-purity PbI_2 nanoparticles synthesized from lead-acid accumulator anodes

5. *Chapter 6* This chapter provides the effect of annealing temperature on nanocrystalline TiO_2 for solar cell application

6. *Chapter 7*: This chapter provides thermal stability study of perovskite solar cell precursors (CH_3NH_3I and PbI_2)

7. *Chapter 8*: This chapter highlights the effect of 6R and 12R lead iodide polytypes on $MAPbX_3$ perovskite device performance.

8. *Chapter 9*: In this chapter, effect of annealing temperature on $MAPbX_3$ perovskite solar cell performance fabricated in ambient atmosphere has been evaluated

9. *Chapter 10*: This chapter gives the summary of the study, provides conclusion and suggest possible future work for perovskite solar cells.

References

[1] Cohen, J.E., 2010. Beyond Population: Everyone Counts in Development, CGD Working Paper 220. Washington, D.C.: [Accessed on 10 Oct 2015]*http://www.cgdev.org/content/publications/detail/1424318*

[2] Parry, I., Heine, D., Lis, E., Li, S., 2014. Getting Energy prices right: From principle to practice *International Monetary Fund*, book: isbn=1498309038

[3] Harris, J.M., Roach, B., 2016. Environmental and natural resource economics: A contemporary approach,[Accessed on 10 Oct 2015] *www.ase.tufts.edu/gdae/Pubs/te/ENRE/4/Ch11.Energy.4E.pdf*

[4] McCartney, H.A., Unsworth, M.H., 1978. Spectral distribution of solar radiation. I : direct radiation, *Quarterly Journal of the Royal Meteorological Society*, 104, 699–718

[5] Stair, R., Johnston, R.G., Bagg, T.C., 1954. Spectral Distribution of Energy From the Sun, *Journal of Research of the National Bureau of Standards*, 53(2):113–119

[6] Roadmap,T., 2014. Technology Roadmap: Solar Photovoltaic Energy, *International Energy Agency*, online: https://www.iea.org/publications/freepublications/publication/technology-roadmap-solar-photovoltaic-energy—2014-edition.html.

[7] Saga, T., 2010. Advances in crystalline silicon solar cell technology for industrial mass production, *Npg Asia Materials*, 2(3): 96–102

[8] Feron, K., Belcher, W.J., Fell, C.J., Dastoor, P.C., 2012. Organic Solar Cells: Understanding the Role of Forster Resonance Energy Transfer, *International Journal of Molecular Sciences*, 13:17019–17047

[9] Heremans, P., Cheyns, D., Rand, B.P., 2009. Strategies for Increasing the Efficiency of Heterojunction Organic Solar Cells: Material Selection and Device Architecture, *Accounts of chemical research*, 42(11):1740–1747

[10] Liu, R., 2014. Hybrid Organic/Inorganic Nanocomposites for Photovoltaic Cells, *Materials*, 7:2747–2771

[11] Krinichnyi, V.I., Yudanova, E.I., Spitsina, N.G., 2010. Light-Induced Electron Paramagnetic Resonance Study of Poly(3-alkylthiophene)/Fullerene Composites, *The Journal of Physical Chemistry C*, 114:16756–16766

[12] Peter, L.M., 2011. Towards sustainable photovoltaics: the search for new materials, *Philosophical Transactions of the Royal Society A*, 369:1840–1856.

[13] Meister, M. Charge Generation and Recombination in Hybrid Organic/Inorganic Solar Cells. PhD thesis, *Johannes-Gutenberg-Universitat Mainz*, (2013).

[14] Hardin, B.E., Snaith, H.J., McGehee, M.D.,2012. The renaissance of dye-sensitized solar cells, *Nature Photonics* 6:162–69

[15] Jung, H.S., Park, N.G., 2014. Perovskite Solar Cells: From Materials to Devices, *Materials views*, 11(1):10–25

[16] Eperon, G.E., burlakov, V. M., Docampo, P., goriely, A., Snaith, H.J., 2013. Morphological Control for High Performance, SolutionProcessed Planar Heterojunction Perovskite Solar Cells, *Materials views* 24(1):151–157

[17] Yang, Z., Zhang, W.H., 2014. Organolead halide perovskite: A rising player in high-efficiency solar cells, *Chinese Journal of Catalysis* 35:983–988

Chapter 2

Theoretical Background

Two promising emerging technologies for PV electricity generation are organic photovoltaics (OPV) and organic-inorganic perovskite solar cells, devices which can potentially be produced at low cost. Compared to traditional silicon-based or other inorganic solar cells, both OPV and perovskite-based SCs have the advantages of material diversity, abundance, and open up the possibility of printing on a large-scale and even on flexible substrates. In this chapter we highlight the background of these solar cells.

2.1 Photovoltaics

Photovoltaic power generation has been receiving considerable attention as one of the most promising energy generation alternatives. The photovoltaic (PV) industry has been continuously growing at a rapid pace over the recent years [1]. Silicon crystalline PV modules are widely used in the world. New PV technologies with cheaper manufacturing cost compared to traditional silicon crystalline based modules are available in the international market these days such as; amorphous silicon (a-Si), Cadmium Telluride (CdTe) and Copper Indium Selenium (CIS) [2]. In addition, new standards and testing schemes have been developed to be comparable with the new or improved technologies [3].

The photovoltaic effect was discovered in 1839 by Becquerel [4]. However, it was not until 1883 that Charles Fritts developed the first solar cell, based on selenium [5]. In 1954 Chaplin et al [6] from Bell Laboratories found that silicon doped with certain impurities i.e gallium and lithium was very sensitive to light. This led to the first practical solar cells, with power conversion efficiency of around 6%.

The efficiency of the panel is determined by the semiconductor material that the cells are made from as well as the process used to construct the cells. Solar panels come in three types: amorphous, monocrystalline, and polycrystalline. These types are unfolded within three PV solar cell generations that are discussed below. Figure 2.1 summarizes the expected price-efficiency performance ratio of the three generations: First generation solar cells have an efficiency around 20%. They were very expensive in the past but have become much cheaper recently as illustrated in Figure 2.1. The second generation has lower efficiencies and is finally expected to be cheaper than the first generation. The third generation is expected to combine both high efficiency and low price. Figure 2.1 also illustrate two limits : The single bandgap limit lies in between approximately 31 and 41%, depending on the semiconductor material [7].

2.1.1 First Generation Solar cells

Solar Cells are one the oldest and commonly used technology because of their high PV power efficiency. The First Generation solar cells are single-junction solar cells produced on single crystal or polycrystalline on silicon wafers which can supply 2-3 watt power. To increase power, solar modules, which consist of many cells, are used. Generally, there are two types of First Generation solar cells. They differ by their crystallization levels. If the whole wafer is only one crystal, it is called the single crystal solar cell. If wafer consists of crystal grains, it is called polycrystalline solar cell. The boundaries between grains are clearly visible on the solar cell. Although the efficiency of monocrystalline solar

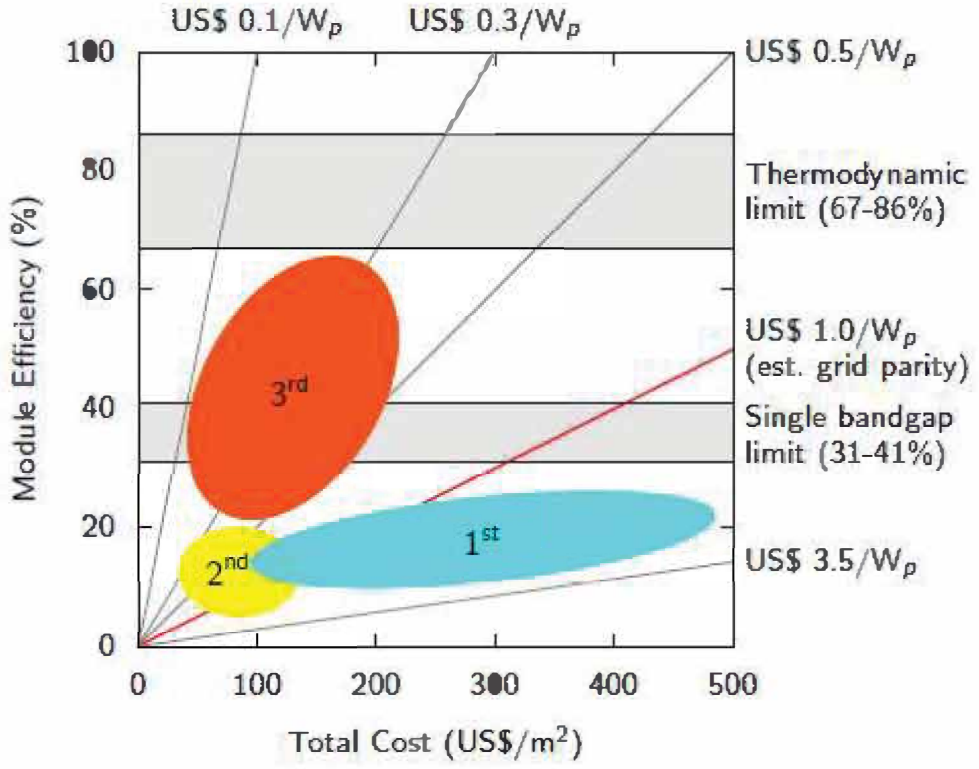

Figure 2.1: Illustration of the (expected) total costs and module efficiencies of the three generations of photovoltaics [7]

cells is higher than polycrystalline solar cells, production of polycrystalline wafers is easier and cheaper. The efficiency of commercial single crystalline cells lies in the range of 18-20 %, and for polycrystalline cells, which account for more than 60 % of the world market ranges at 13-14 % [8].

Even though first generation solar cells are commercially available, there is still a room to improve the fabrication cost and power efficiency. Understanding the nature of defects resulting from crystal growth and processing and treatments to minimize carrier losses can be considered as future work to improve first generation solar cells.

2.1.2 Second Generation Solar Cells

The Second Generation photovoltaic materials are based on thin film technologies not requiring the use of silicon wafers. They currently have low efficiencies and less cost compared to First Generation [9]. In addition, they have an advantage in visual aesthetic. Since there are no fingers in front of the thin film solar cells for metallization, they are much more applicable on windows, cars, building integrations etc. These thin films can also be grown on flexible substrates as shown in Figure 2.2. So Second Generation solar cells are applicable on textile products or on foldable devices. As an advantage of thin film solar cells, they can be grown on large areas up to 6 m^2. However, wafer-based solar cell can be only produced on wafer dimensions. The Second Generation solar cells include amorphous Si (a-Si) based thin films solar cells, Cadmium Telluride/Cadmium Sulfide (CdTe/CdS) solar cells and Copper Indium Gallium Selenide (CIGS) solar cells [10].

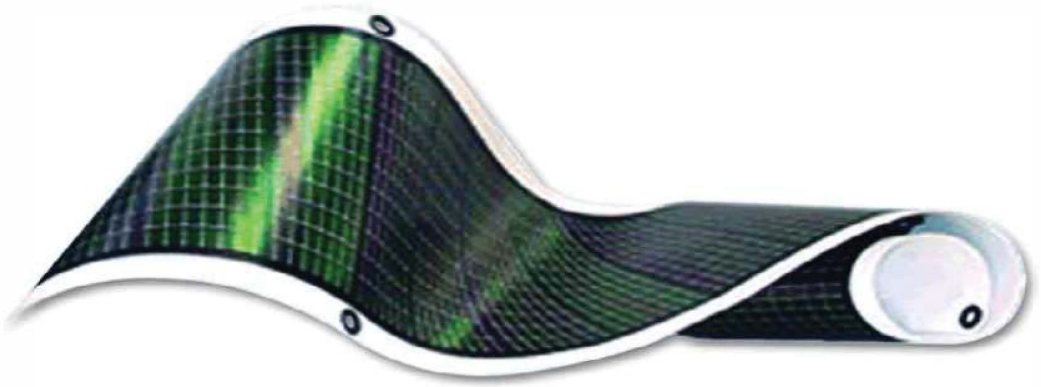

Figure 2.2: Flexible substrates [9]

2.1.3 Third Generation Solar Cells

For solar cells to achieve truly competitive cost to efficiency ratios, significant breakthroughs in technology is needed. This gave birth to Third Generation

solar cells known as photovoltaics. These are broadly defined as semiconductor devices which do not rely on traditional p-n junctions to separate photogenerated charges. This class is a novel technology which is promising but not commercially proven yet. Most developed Third Generation solar cell types are dye sensitized and concentrated solar cell [10]. Dye-sensitized solar cells are based on dye molecules between electrodes. Electron-hole pairs occur in dye molecules and transported through titanium dioxide TiO_2 nanoparticles. Although their efficiency is very low, their cost is also very low. Their production is easy with respect to other technologies. Dye-sensitized solar cells can have variable colors.

On the other hand, the concentrated PV (CPV) solar cell is another promising technology. The main principle of concentrated cells is to concentrate a large amount of solar radiation onto a small region where the PV cell is located. The amount of semiconductor material, which might be very expensive, is reduced in this way. Concentration levels start from 10 suns to thousands of suns. So, the total cost can be lower than conventional systems. Concentrator photovoltaics (CPVs) are promising technologies for near future.
Devices can be fabricated using high throughput, low-temperature processes such as printing [12], and because these processes require less energy than that required for the manufacture of silicon-based devices the production costs are lower. To improve the efficiency both material properties and device fabrication need to be optimized. The required improvement in the materials requires a greater understanding of the underlying physics involved, and it is in this area that this thesis concentrates. Before a detailed description of the materials is given it is necessary to have an appreciation of the application: organic photovoltaic devices.

In the next sections, the parameters measured to calculate a power conversion efficiency are outlined, along with the various device structures used in organic

solar cells.

2.1.4 Working principle of Photovoltaics

Concerning photovoltaics, there is a fundamental difference between organic and inorganic semiconducting materials with respect to the photogeneration of charge carriers. Whereas light absorption in inorganic semiconductors readily generates free charge carriers throughout the bulk, the relatively low dielectric constant of organic semiconductors results in the formation of a tightly bound electron-hole pair, known as an exciton.

The general concept of a solar cell is mainly outlined as follows; An electron is excited by solar radiation and then it is collected at the anode before it loses the gained energy completely. Then the electron will be re-injected with energy below Fermi level E_F into the cell from the cathode. The energy difference of the electron (between its energy at anode where it is collected and the energy at the cathode where it is re-injected) is used to do work (electrically, voltage times current). However, this process is called *photovoltaic effect* [13]. The photovoltaic effect is closely related to the photoelectric effect, where electrons are emitted from a material that has absorbed light with a frequency above a material-dependent threshold frequency. Absorption of a photon in a material means that its energy is used to excite an electron from an initial energy level E_i to a higher energy level E_f. Photons can only be absorbed if electron energy levels E_i and E_f are present so that their difference equals to the photon energy, hv = E_f - E_i. The absorption of a photon in an ideal semiconductor is illustrated in Figure 2.3.

Currently, we are in the midst of the third generation solar cell era. The main focus at this stage is to make the electricity production cost of solar cell commercially competitive by reducing the cell fabrication costs and push the efficiencies above Shockley and Queisser limit (SQ) [17]. The developments have taken many directions, which can be categorized in different forms.

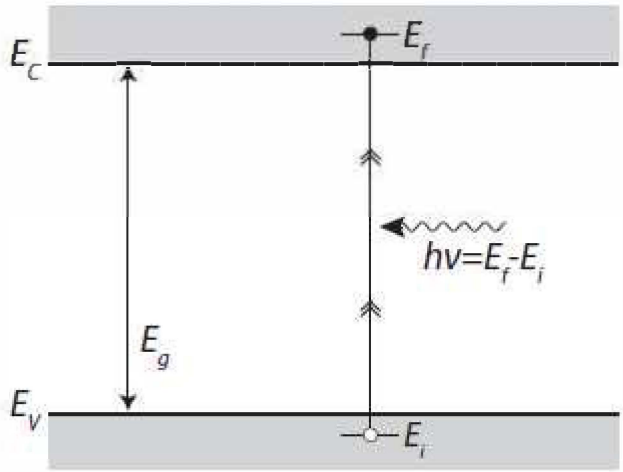

Figure 2.3: Illustrating the absorption of a photon in a semiconductor with bandgap E_g. The photon with energy hv excites an electron from E_i to E_f. At E_i a hole is created. [14]

Currently, there are some strategies of how to exceed the SQ limit:

1. More than one semiconductor material (excluding doping materials) per solar cell: Use more than one semiconductor material in a cell. Each incorporated semiconductor material will produce electric current in response to different wavelengths of light. The use of multiple semiconducting materials allows the absorbance of a broader range of wavelengths, improving the photons to electrical energy conversion efficiency. This allows the junctions to be stacked, with the layers capturing the shortest wavelengths on top, and the longer wavelength photons passing through them to the lower layers as shown in Figure 2.4

2. The sunlight is not concentrated - a "one sun" source. Sunlight can be concentrated about 500 times using inexpensive lenses: By employing what is known as Concentrated Photo Voltaic (CPV). Contrary to conventional photovoltaic systems, it uses lenses and curved mirrors to focus sunlight onto small, but highly efficient, multi-junction (MJ) solar cells. With

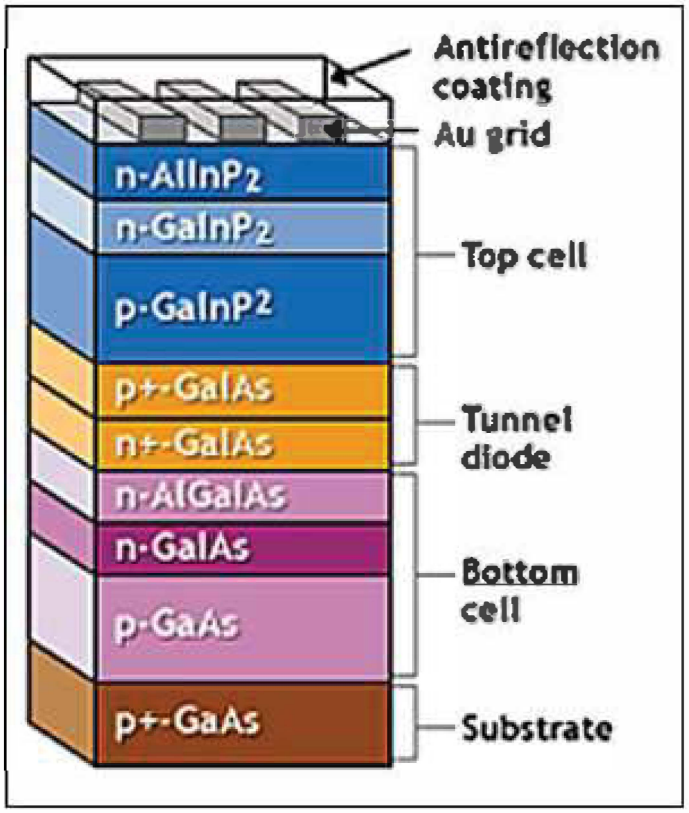

Figure 2.4: The typical of a multi-junction cell that has a top cell of gallium indium phosphide, [24]

this method where one can focus the sun beams to generate more power per unit of surface area, was an early favorite to increase solar efficiency (Figure 2.5).

3. Combining a PV semiconductor with a heat based technology to harvest both forms of energy, "quantum dots" to harvest some of the excess photon energy for electricity: an regular solar cell, each photon collision generates a particle pair consisting of one free hole and one free electron. Quantum Dots are extremely small "nanocrystals" (the names are used somewhat interchangeably) interspersed in a larger semiconducting material [18]. Quantum Dots (QDs) range between 1 and 20 nanometers in size. Semiconductors at this size have different physical properties compared to bulk materials. When photons with energy greater than the band gap energy collide with a Quantum Dot several "hot" hole/electron pairs

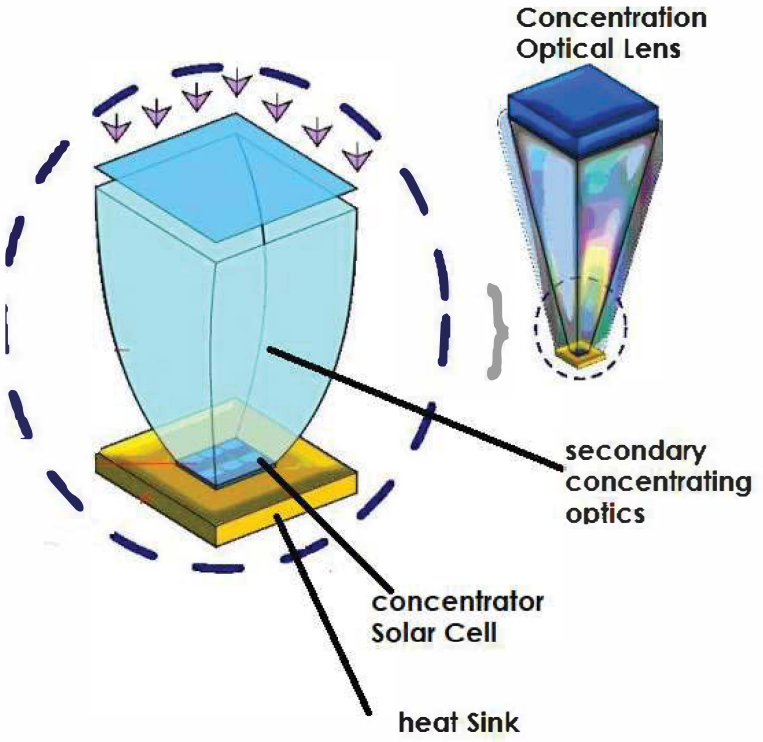

Figure 2.5: Illustration of Concentrated PhotoVoltaics (CPV) [15]

can be created as opposed to one pair and heat. Although silicon can be used as a nanocrystal, lead selenide (PbSE) also a semiconductor, is being used more frequently as the material of choice.

4. Employment of the Hybrid perovskites: Perovskites are a special family of hybrid organic-inorganic crystalline materials with AMX_3 perovskite structure, where A is the organic site, M is a metal, and X is the halogen [19]. The structure, which seems complex chemically, is extremely rich and can be grown and controlled relatively easily with high quality. However, the real thrust of making solar cells out of them is very recent [20, 21]. At the end of 2013, an efficiency of 16.2% was reported [22] and it is expected that 20%+ efficiency can be achieved within few years [23]. This also highlights the area of focus in this study.

2.2 Photovoltaic solar cell architecture

The organic-inorganic photovoltaic cell has two flat electrodes with different work function separated by an active layer. It is known that the structure and the working function plays a huge role in an output power efficiency of the cell. In this section, some basics of organic-inorganic solar cells are outlined. First, device construction is outlined and the difference between a bilayer heterojunction and a bulk heterojunction is emphasized. It is important to know that, in organic-inorganic solar cells or any organic devices, a photovoltaic current can be even in asymmetrical devices. A setup is with only one photoactive material and electrodes constructed with the same material from the top and bottom part. In this type of a device, the excitons must remain intact (not relaxed) long enough to reach an electrode and dissociate. Since the electrons and holes are so tightly bound, only those excitons that reach an electrode can dissociate and lead to charge flow. This highlights the advantage of having a donor–acceptor heterojunction in the active layer of an organic-inorganic device. Figure 2.6 (a) depicts the band structure of a device that contains only one material in the active layer, while Figure 2.6 (b) depicts the band structure of a device with a donor–acceptor blend. These figures highlight how exciton dissociation produces free charge carriers either at the electrode (Figure 2.6 (a)) or at the heterojunction (Figure 2.6 (b)).

Furthermore, the structure of the heterojunction-bilayer or bulk plays an important role in characteristics and performance of the organic-inorganic device. Figure 2.7 shows a planar bilayer device indicated by the junction between donor and acceptor material. In a bulk heterojunction device, attempts have been made to maximize/optimize the interface between phases [16]. In organic solar cells made from blends of conjugated polymers (donor) and fullerenes (acceptor), it is the conjugated polymer that absorbs the incident light. The absorption process generates an exciton that can either relax back to the ground state or dissociate into an electron and a hole. Since, inorganic

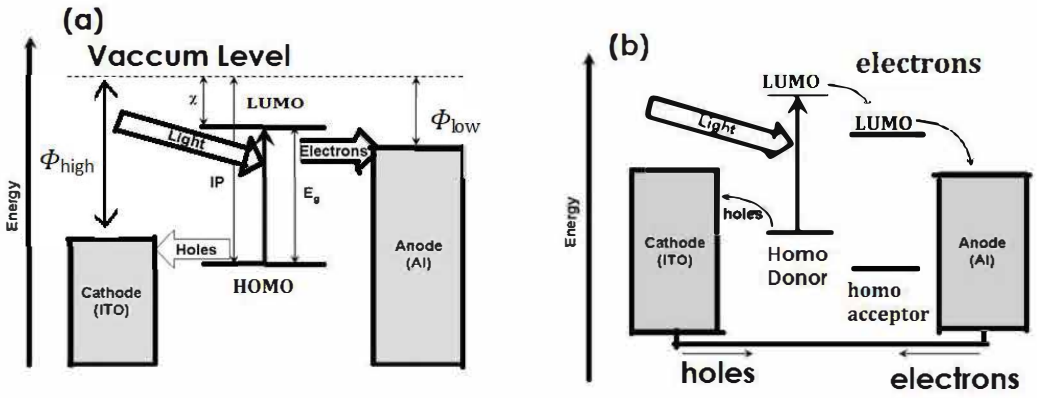

Figure 2.6: Schematic diagram of the band structure of (a) an organic solar cell having only one material in the active layer and different types of electrodes. (b) a heterojunction organic solar cell. The active layer in this type of device contains a donor and an acceptor. Also, here the electrodes are short-circuited to equalize their work functions.

cells, exciton diffusion lengths are small and the dissociation process only occurs at the donor/acceptor interface, controlling the structure of the active layer is very important to constructing efficient devices. Figure 2.8 shows device designs used for cells comprising two components, an electron donor (D) and an electron acceptor material (A). Charge separation occurs at the interface between those two. Ideally, the D- material should only be in contact with the electrode material with the higher workfunction (typically ITO) and the A-material with the lower workfunction electrode (typically Al). The low and high work function are necessary for the effective injection of electrons and holes, respectively.

2.2.1 Electrodes

Transparent electrodes are essential components in many optoelectronic technologies such as touch screens, LCDs, OLED and solar cells [25]. In organic devices, the workfunction (W_f) of the electrode materials is very important since it determines together with the LUMO/HOMO and Fermi level of the semiconductor whether the electrode forms an ohmic or a blocking contact for the respective

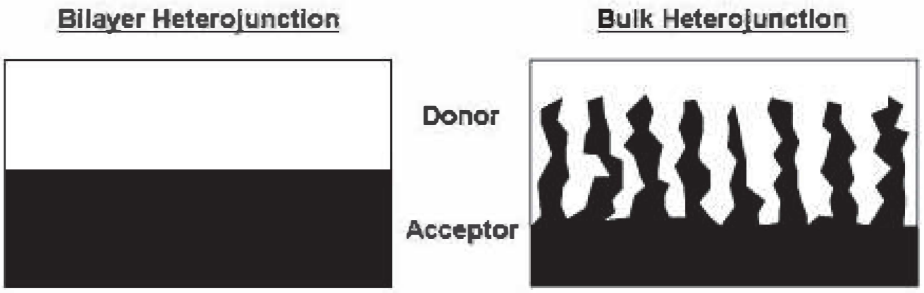

Figure 2.7: Illustration of bilayer and bulk heterojunction active layers. [25]

charge carrier (holes in VB, electrons in CB). Moreover a large difference in W_f of the electrode materials can increase the open circuit voltage V_{oc} considerably [26]. Depending on the type of solar cell considered, the active layer can have different configurations. Common electrode materials for the electron collecting contact (low W_f required) of organic solar cells are Al, Ca, In, Ag whereas for the hole collecting contact high workfunction materials like Au are preferred.

For the solar cell, one contact has to be at least partly transparent. Semi-transparency can be obtained if the sublimed metal e.g. Au is not much thicker roughly between 15-20 nm thick compared to 50-100 nm which are typical values for non-transparent contact. For these reasons so-called conducting glasses are often used [27]. Particularly, Indium Tin Oxide (ITO) which is a degenerated semiconductor comprising a mixture of In_2O_3 (90%) and SnO_2 (10%) with a bandgap of 3.7 eV and a Fermi-level between 4.5 and 4.9 eV is widely used. The large bandgap allows no absorption for wavelengths longer than 350 nm. The material can be highly conducting if there is an excess of Indium (In) due to a lack of oxygen - so that In acts as n-type dopant leading to very low sheet resistances. The ITO covered quartz substrates

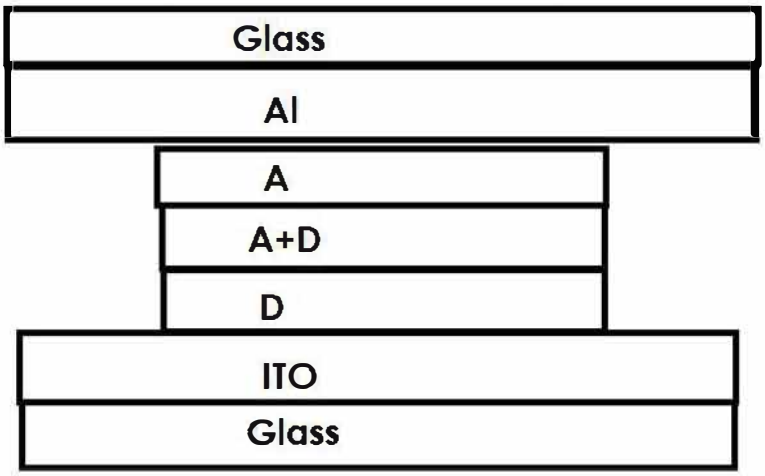

Figure 2.8: The organic photovoltaic cell. [35]

are commercially available since they are widely used as conducting glasses in the liquid crystal screen industry. Other conducting glasses are Tin oxide and Indium oxide. Alternatively, conjugated polymers with absorption in the whole visible range can be used if they are doped so that the allowed energy levels move deep into the bandgap and create an absorption minimum in the visible region [28].

The search for novel electrode materials with good stability, high transparency and excellent conductivity is, therefore, a crucial goal for optoelectronics. Several new versatile nanostructured electrode materials have been reported for the development of solar cell applications, such as carbon electrodes (Single-walled carbon nanotube (SWCNT), multi-walled carbon nanotube (MWCNT), graphene oxide (GO) and fullerene), metal oxides (TiO_2), fluorinated tin oxide (FTO), (SnO_2), boron-doped ZnO and Cu_2O) and conducting polymers (Poly(3,4-ethylenedioxythiophene) (PEDOT) poly(styrenesulfonate) (PSS), and a combination of PEDOT PSS, poly-3-hexylthiophene and polyaniline) electrodes etc.

To elaborate more, Graphene, which is a two-dimensional material is rising star in material science,and that it exhibits remarkable electronic properties that qualify it for applications for future optoelectronic devices. Recently, transparent and conductive graphene-based composites have been prepared by incorporation of graphene sheets into polystyrene or silica. However, the conductivity of such transparent composites is low, typically ranging from 0.001 to 1 s/cm depending on the graphene sheet loading level, which makes the composites incapable of serving as window electrodes in optoelectronic devices [29].

2.2.2 Active Layer Morphology

In general, the active layer is sandwiched between two electrodes. It consists of two materials, one electron donor, and one electron acceptor material. Poly-(phenylene vinylene) derivatives and poly-(alkylthiophenes) are common donors; fullerene and its derivatives are common acceptors. For Perovskite solar cells lead methylammonium tri-iodide ($CH_3NH_3PbI_3$) is used as a light harvester. This layer is responsible for light absorption, exciton generation/dissociation, and charge carrier diffusion. For example, when a photon strikes the perovskite ($CH_3NH_3PbI_3$) it knocks an electron loose. The empty spot vacated by the electron is called a hole, and acts as a positively charged particle. The subsequent motion of the electrons and holes is what generates electrical current. Because the perovskite itself doesn't conduct the movement of holes very well, solar cells require an additional layer of a hole-transport material to facilitate current flow. One common hole-transport material is a compound called N^2,N^2,$N^{2'}$,$N^{2'}$,N^2,N^2,$N^{2'}$,$N^{2'}$-octakis(4-methoxyphenyl)-9,9'-spirobi[9H-fluorene]-2,2',7,7'-tetramine (spiro-OMeTAD). To boost the current even more, researchers add a lithium salt called LiTFSI to spiro-OMeTAD. This process is called "doping."

Spiro-OMeTAD is an amorphous material, which gives it some unique properties. Most solid materials have well-defined electronic energy bands in which electrons and holes can move through the material. Crystals, for example, often have band structures that allow a symmetric flow of both electrons and holes, unlike the amorphous materials. Due to this asymmetric band structure, holes can have some difficulty in traveling through an amorphous material because they can get trapped in a particular energy level. In principle, doping spiro-OMeTAD with LiTFSI prevents the holes from getting trapped. Pairs of electrons occupy each energy level in spiro-OMeTAD. But when LiTFSI is introduced, one of those electrons is removed, leaving behind a hole in its place. The presence of that hole prevents other holes from getting stuck at that energy level, allowing them to move freely and generate electrical current. Furthermore, some of the key requirements for the active materials are as follows;

1. They should be broadband absorbers and have low fluorescence. Photo-excitations in the active material produce bound excitons (bound electron-hole pairs), and these excitons must dissociate in order for charge transport to occur.

2. The active materials should ideally have long diffusion lengths so that once an exciton is created it can reach an interface and be separated into charge carriers.

3. The materials need to have good charge transport properties for these charges to reach the electrodes.

4. Finally, to be able to utilize these properties and to lower fabrication costs the material should be soluble (although this is not essential). On top of the active layer there is a deposited anode, typically made of aluminum or gold. Besides, a very thin layer of lithium fluoride (5–10 Å) is usually placed between the active layer and the aluminum anode.

The lithium fluoride serves as a protective layer between the metal and organic material [30].

2.2.3 Factors determining the performance of organic–Inorganic solar cells

At first, at least one, but preferably both components of the photoactive layer should have a large absorption coefficient and a broad absorption spectrum in order to create a good overlap with the solar emission spectrum. Most conjugated materials are strong absorbers in the visible region with the exception of some, such as Phenyl–C61–butyric acid methyl ester (PCBM). However a considerable amount of solar energy is located at near infrared region, which causes a non-negligible spectrum mismatch between the photo-response of active layer and solar solar emission spectrum. In order to make a breakthrough in achieving highly efficient cells, it is important to find donor materials whose photo absorption range better overlaps solar emission.

Secondly, the donor material should have a high hole mobility, whereas the acceptor should have high electron mobility. Most donor materials are reasonably good hole transporter with hole mobilities in the range of 10^{-6} to 10^{-3} $cm^{-2}V^{-1}s^{-1}$ [30]

Thirdly, one of both components in an active layer should be easily oxidized (the donor), whereas the other one should be easily reduced (the acceptor). This means that for efficient photoinduced electron transfer from donor to acceptor, the lowest unoccupied molecular orbit (LUMO) of the donor should be located at higher potential energy than the LUMO of acceptor. In this way, photoinduced charge transfer can become the main decay mechanism of the excited state that was created by the absorption of light [31].

Fourth, material design of both donor and acceptor should allow for a large open-circuit voltage (V_{oc}). The open circuit voltage is related to the distance between the highest unoccupied molecular orbit (HOMO) level of

the donor and LUMO level of the acceptor. Additionally, the position of the LUMO level of the acceptor with respect to the work function of the electron collecting electrode should provide easy electron contact at the contact point. The same holds for HOMO of the donor with the hole collecting electrode. Therefore, a proper choice of the electrode materials should ensure the effective efficient charge collection on the contacts point.

2.3 Perovskite Based Solar Cell

In the past two decades, the organic-inorganic hybrid perovskites have arisen as new active materials and drawn great attention for research. The name "Perovskite" originates from the mineral called Calcium titanate which was discovered in the Ural mountains by a German mineralogist Gustav Rose in 1839 [31]. He named it in honor of Count Lev Aleksevich von Perovski, a Russian statesman, and mineralogist. Up to date, perovskites are a broad class of materials with structures based on the ABX_3 crystalline arrangement of the original mineral. The inexorable rise of perovskites has been driven by their enormous chemical and structural flexibility, and by their outstanding physical and chemical properties, which are often the best in their field [1].

Perovskite is increasingly and economically important. It is sought after for its rare earth metal content. For example perovskite is enriched in cerium, niobium, thorium, lanthanum, neodymium and other rare earth metals. Furthermore, these rare earth metals are becoming rather attractive for prospectors due to their growing value to photovoltaic industry. The titanium derived from perovskite is recovered as well. The most commonly used perovskite material in photovoltaics is lead methylammonium tri-iodide ($CH_3NH_3PbI_3$), which possesses high charge carrier mobilities in combination with long charge carrier lifetimes, resulting in efficient charge extraction. The function of methylammonium lead iodide ($CH_3NH_3PbI_3$) perovskite is akin to that of the "electron donor"

material in donor-acceptor polymer/organic planar- and bulk-heterojunction solar cells (i.e., PHJs and BHJs, two typical configurations of these types of cells).

Accordingly, we propose depositing or growing a thin layer of acceptor material on $CH_3NH_3PbI_3$ perovskite film to create a donor-acceptor contact interface for charge separation, in which the hybrid $CH_3NH_3PbI_3$ perovskite/acceptor PHJ yields the photovoltaic effect under irradiation. Figure 2.9 shows the comparison of the power conversion efficiencies of third generation solar cells with the existing technologies based on inorganic materials. It shows the record of power conversion efficiencies from different research institutions, industries, and university with respect to the year in which the efficiencies were obtained. It is clear that perovskite efficiency has increased rapidly from 4 % to 20 % which still needs to be improved. In this thesis work, attention has been addressed to hybrid perovskite-based solar cells for the improvement of power efficiency.

2.3.1 Structure of Perovskite

The basic building component of organic-inorganic perovskite hybrids is the ABX_3, where X is typically an anion: O^{2-}, CI^{-} , Br^{-} or $S^{2}-$, and the M atom is generally a divalent metal that can adopt an octahedral anion coordination, such as Ge^{2+}, Sn^{2+}, Pb^{2+}, Co^{2+}, Fe^{2+}, Cu^{2+}, Ni^{2+}, Mn^{2+}, Cr^{2+}, Pd^{2+}, Cd^{2+}, Eu^{2+} and or Yb^{2+}. They form the MX_6 octahedra where M located at the center of the octahedra and X lies in the corner around M (Figure 2.10). The MX_6 octahedra form an extended three-dimensional (3D) network by all-corner connected type. The perovskite lattice arrangement is shown in Figure 2.10, but it must be considered that, as with many structures in crystallography, it can be represented in multiple ways. The simplest way to think about a perovskite is as a large atomic or molecular cation (positively

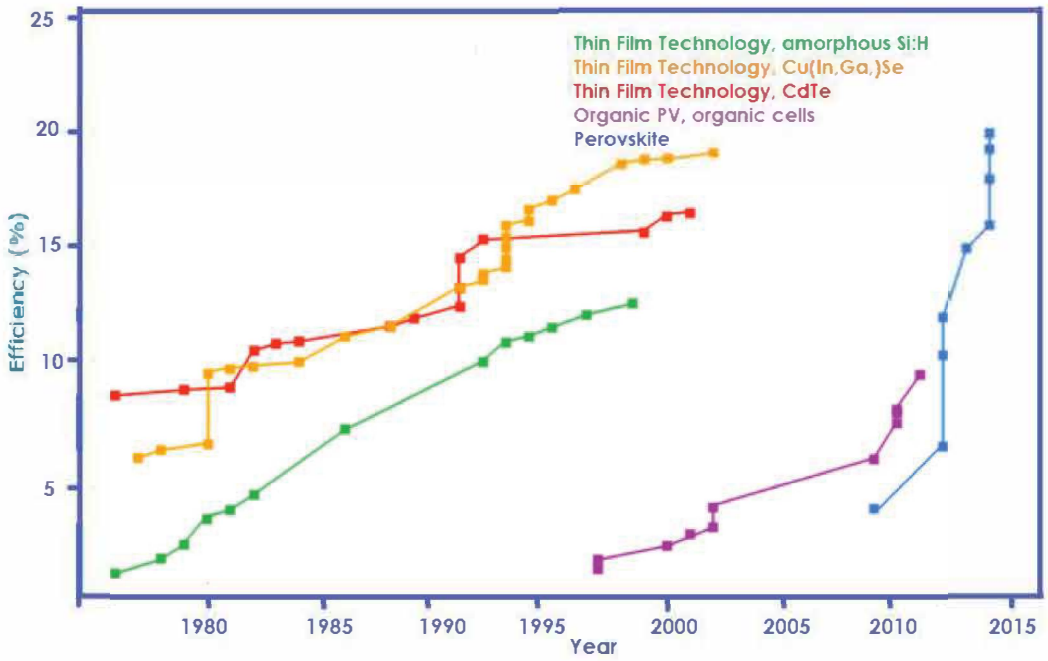

Figure 2.9: Perovskite solar cells with an increase in power conversion efficiency at a phenomenal rate compared to other types of photovoltaics. [30]

charged) of type A in the center of a cube. The corners of the cube are then occupied by atoms B (also positively charged cations) and the faces of the cube are occupied by a smaller atom X with the negative charge (anion). Depending on which atoms/molecules are used in the structure, perovskites can have an impressive array of interesting properties including superconductivity, giant magnetoresistance, spin-dependent transport (spintronics) and catalytic properties. Perovskites, therefore, represent an exciting playground for physicists, chemists, and material scientists [33].

the oxides can tolerate different ions in A- and B-sites as discussed before. The coordination numbers of A- and B-sites are 12 and 6, respectively. In the idealized perovskite-type oxide, the structurally related parameters have the following relation:

$$r_A + r_X = \sqrt{2}(r_B + r_X) \tag{2.3.1}$$

where r_A, r_X and r_B are the effective ionic radii for A, X and B ions,

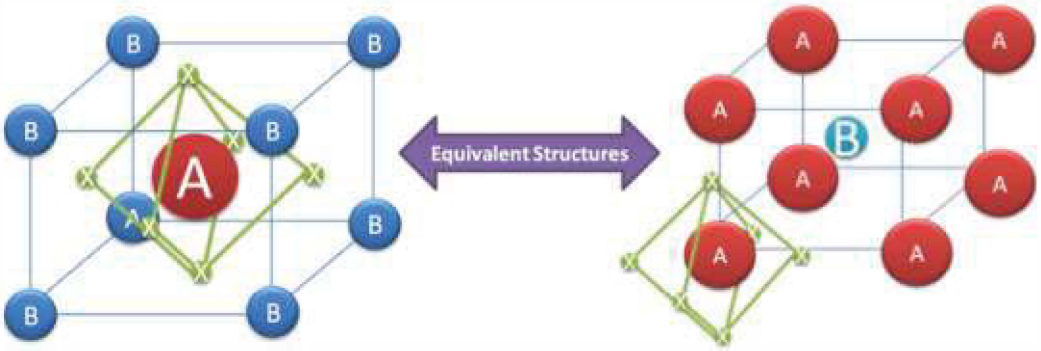

Figure 2.10: A generic perovskite crystal structure of the form ABX_3. Note however that the two structures are equivalent the left hand structure is drawn so that atom B is at the $< 0, 0, 0 >$ position while the right hand structure is drawn so that atom (or molecule) A is at the $< 0, 0, 0 >$ position. Also note that the lines are a guide to represent crystal orientation rather than bonding patterns [33]

respectively. Based on the geometric constraints imposed by a rigid sphere model, the size of A cation influences a lot the perovskites structures resulting in either rhombohedral (R3m), orthorhombic (Amm2), tetragonal (P4mm) and cubic (Pm-3m). Here we define the formability of perovskite as estimated based on its geometric tolerance factor *(t)*:

$$\mathrm{t} = \frac{r_A + r_X}{[\sqrt{2}(r_B + r_X)]} \tag{2.3.2}$$

For transition metal cations containing oxide perovskite, an ideal 3D cubic perovskite is expected when $t = 1$ while octahedral distortion is expected when $t < 1$. Symmetry also decreases for $t < 1$, which may affect electronic properties. For alkali metal halide perovskite, formability is expected for $0.813 < t < 1.107$ [33]. Besides the 3D network mentioned above, a 2-dimensional network is also a quite common structure for organic-inorganic hybrid perovskites. It happens when the group A is too large to fit into the space provided by the nearest-neighbors X within the inorganic sheet, the organic group A then causes distortion of cubic structure and in this situation, the tolerance factor t is much larger than 1. In such cases, the organic group needs to be held away from the inorganic sheets by a spacer, such as an alkyl

chain, in order to grow 2D perovskites layered structures.

This 2D perovskite can be expressed through $(R\text{-}NH_3)2MX_4$ where $R\text{-}NH_3^+$ is an aliphatic or aromatic ammonium cation, X is a halogen and M is a divalent metal ions such as Cu^{2+}, Ni^{2+}, Co^{2+}, Fe^{2+}, Mn^{2+}, Pd^{2+}, Cd^{2+}, Ge^{2+},Sn^{2+}, Pb^{2+}, Eu^{2+}, etc. The basic structures of 2D organic - inorganic perovskite are illustrated in Figure 2.11(a and b). The perovskite consist of single layers of oriented inorganic sheets separated by bilayers of organic ammonium cations, where the organic groups R self-assemble via (pi-pi)"Π - Π" interaction (when the organic group contains aromatic groups) or through Van der Waals force (when the organic group contains alkyl chains). In $(NH_3\text{-}R\text{-}NH_3)MX_4$ systems, shown in Figure 2.11(b), the organic cations make hydrogen bonds with the inorganic sheets at both ends rather than only at one end, thereby weakening the Van der Waals interaction between the layers. According to Yang [34] perovskites could function as both a light absorber and an electron transporter within the solar cell.

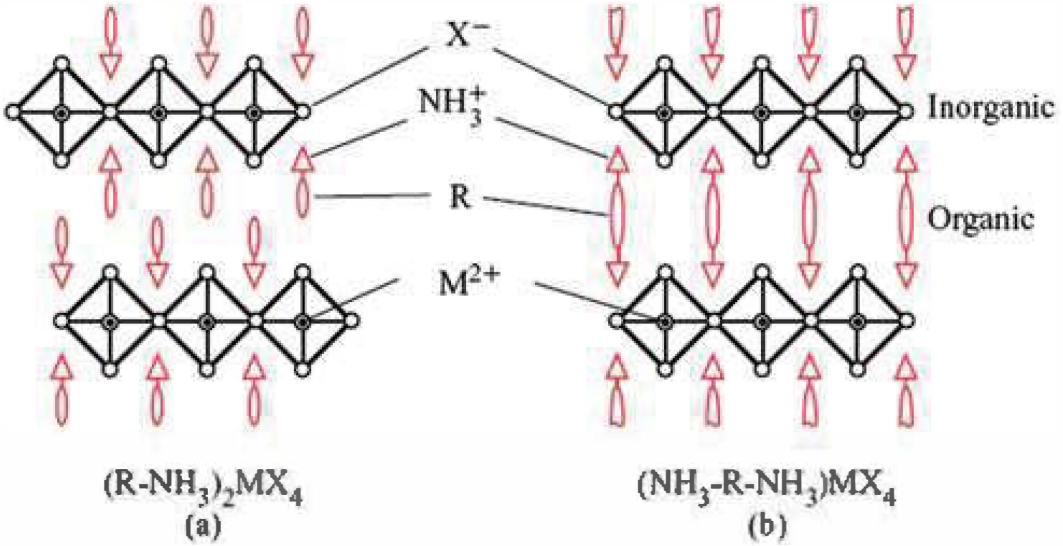

Figure 2.11: The basic structures of 2D organic–inorganic perovskite with bilayer (a) and (b)single layer intercalated organic molecules [33]

2.4 Characterization of photovoltaic solar cells

In this section, the most common techniques used to characterize and evaluate the photovoltaic performance of solar cells are presented. The most general methods include current-voltage and quantum efficiency measurements, classified as steady-state techniques. These are time-independent measurements where the charge density within the metal oxide semiconductor does not vary as a function of time. Hence, the processes of photogeneration and charge-transport through the semiconductor are in equilibrium with the loss processes of charge recombination.

On the other hand, the photoexcited electron can decrease its potential energy by losing energy to phonons until it reaches the lowest lying level in the conduction band (CB) which is the lowest unoccupied molecular orbit (LUMO). Since the phonon energy dissipates into heat this process is known as thermalisation. As a consequence of thermalisation the semiconductor bandgap is often regarded as a measure for the achievable voltage. The larger the bandgap the higher the voltage. On the other hand, a smaller bandgap material can absorb more photons and thus increase the number of photogenerated charge carriers i.e. the photocurrent. Hence, there must be an optimal bandgap for a given illumination spectrum. Shockley and Queisser were the first who calculated the maximum power conversion efficiency for a semiconductor with a given bandgap assuming only radiative recombination and the solar radiation. They obtained a value of 30 % from a semiconductor with a bandgap of 1.12 eV [17]. Figure 2.12 shows how the maximum conversion efficiency varies with the bandgap.

Despite the importance of band gap on the PVCs, it is also important to understand the behaviour of a photovoltaic device under illumination in darkness. For example, when illuminating the solar cell, some variables can be extracted

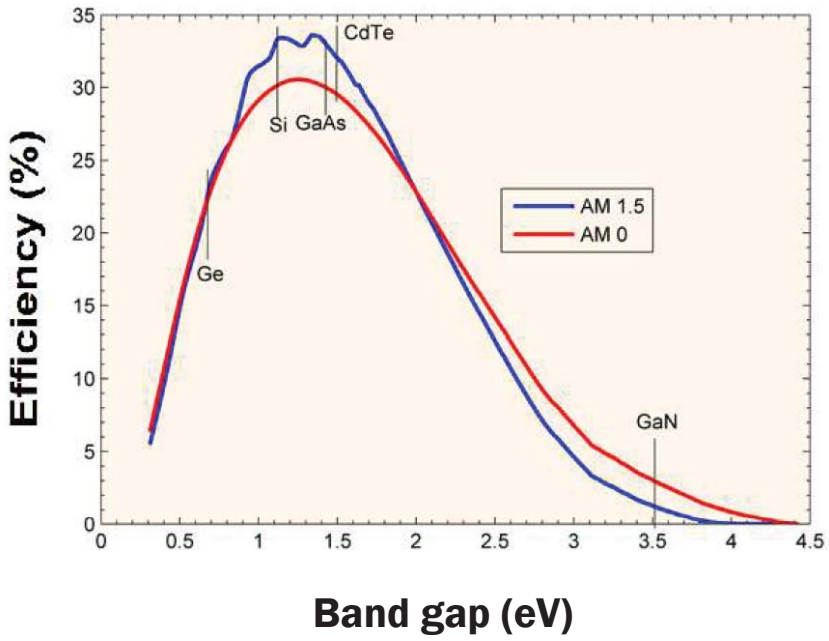

Figure 2.12: Terrestrial AM1.5 and extraterrestrial AM0 solar spectra with the band gap ranges of the different material systems. [17]

such as *J-V* characteristics which define the performance of the solar cell, where J is the current density and V is the voltage. However, the performance of the solar cell does not only depends on the illumination but also on the load such as a load resistor with a known resistance. A typical example of an illuminated *J-V* curve is shown in Figure 2.13.

Several parameters which can be derived from the J–V curve are short-circuit current density Jsc, the open-circuit voltage Voc, the current density at the maximum power point P_{MPP} and the voltage V_{MPP} at the maximum power point. The maximal power density P_{max} is indicated by the shaded rectangle. In the dark state, the *J-V* curve passes through the origin with no voltage, no current flows. When the device is exposed to light, the J-V curve shifts downward. Practically, J-V characteristics are done by applying an external potential bias to the cell while measuring the current response. The applied potential is referred to as forward bias when electrons are injected into the device from the photo-anode side and reverse bias when electrons are injected

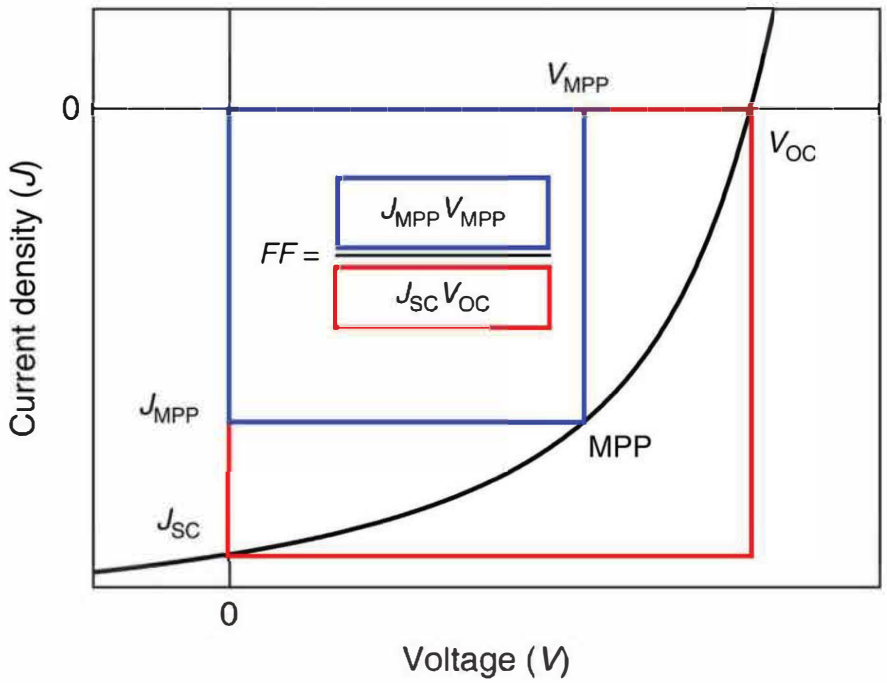

Figure 2.13: Typical J-V characteristics of a solar cell in dark and under illumination. Indicated are the short circuit current density Jsc, the open circuit voltage Voc, the maximal power point MPP and the current density JMPP and voltage VMPP at the maximum power point. [36]

from the counter-electrode (back contact) side. Another important characteristic is the fill factor (FF), which is the ratio of the maximum power (PMP) generated by the solar cell to the product of the voltage open circuit V_{oc} and the short circuit current J_{SC}. The fill factor provides information about the leakage current and the efficiency of charge collection in the device (Equatiion(2.4.1)).

$$FF = \frac{P_{MPP}}{J_{SC} \times V_{OC}} = \frac{J_{MPP} \times V_{MPP}}{J_{SC} \times V_{OC}} \tag{2.4.1}$$

From (Equatiion(2.4.1)) we can determine and define the solar cell conversion efficiency η as the ratio of the maximum generated power ($P_{MPP} = V_{MPP}.J_{SC}$) to the input or incident power P_{in} as given by equation (2.4.2)

$$\eta = \frac{J_{MPP} \times V_{MPP}}{P_{in}} = \frac{V_{OC} \times J_{SC} \times FF}{P_{in}} \tag{2.4.2}$$

where, P_{in} is the total power of sunlight illumination on the cell. To

summarize, (Voc, Isc, and FF) are three important parameters that should be optimized in order to determine solar cell power conversion efficiency. This is the most general way to define an efficiency. The others commonly used term is the Quantum Efficiency (QE). This efficiency of a device is defined as a function of the energy or wavelength of the incident radiation. For a particular wavelength, it relates the number of charge carriers collected to the number of photons striking on the device. QE can be reported in two ways by considering both internal and external factors. External Quantum Efficiency includes losses by reflection and transmission and can also be called IPCE (Incident Photon to Current Efficiency). It is a spectral quantity defined as the ratio between the number of extracted electrons (N_{el}^{out}) and the number of incident photons(N_{ph}^{in}), as shown in Equation (2.4.3):

$$\text{EQE (E)} = \frac{(N_{el}^{out})}{(N_{ph}^{in})} \tag{2.4.3}$$

On the other hand, internal Quantum Efficiency factors out losses due to reflection and transmission of photons such that it considers processes only involving absorbed photons. In relation to transmission and reflection processes, external QE can be transformed into internal QE. IQE is also a spectral quantity and it is defined as the ratio between the number of extracted electrons (N_{el}^{out}) and the number of absorbed photons in the photoactive layer (N_{ph}^{abs}), as shown in Equation (2.4.4):

$$\text{IQE (E)} = \frac{(N_{el}^{out})}{(N_{ph}^{abs})} \tag{2.4.4}$$

Since (N_{ph}^{abs}) can then be associated with (N_{ph}^{in}) through the absorption of the active layer (A), the IQE can be calculated by Equation (2.4.5):

$$\text{IQE (E)} = \frac{EQE(E)}{A(E)} \tag{2.4.5}$$

where:

$$\mathrm{A(E)} = 1 - R(E) - A_{para}(E) \tag{2.4.6}$$

2.5 Impedance Spectroscopy

2.5.1 Ohms Law: Resistance and Impedance

Electrical circuit consists of individual components through which there can be a continuous flow of electrical current, (I). The potential energy of the circuit to move electrons from one point to another corresponds to the voltage, V of the system. The opposition to the motion of electric current is a measure of its electrical resistance, R and is determined from the ratio between the voltage and the current. This is known as Ohms Law:

$$R = \frac{V}{I} \tag{2.5.1}$$

This law assumes an ideal resistor case, where the resistance is constant, frequency independent, independent of the current (resulting in V/I) whereby the alternate current and voltage are in phase with each other. In order to extend this concept to alternating current (AC) circuits the voltage and current need to be treated as complex time-dependent functions to take their phases, ϕV and ϕI respectively,into account

$$V(\omega) = |V|exp[i(\omega t + \phi V)] \tag{2.5.2}$$

$$V(\omega) = |I|exp[i(\omega t + \phi I)] \tag{2.5.3}$$

$$\omega = 2\pi f \tag{2.5.4}$$

where ω is the angular frequency.

Electrical impedance Z is a measure of the opposition to current when a voltage is applied in an AC circuit and corresponds to the generalized resistance in AC circuits. Hence, it is the complex ratio of the voltage and the current (Equation 2.5.5) and takes into account both magnitude and phase, where

φ is the phase difference between the voltage and the current. For a direct current (DC) circuit, the resistance of the system can be taken as impedance with the same magnitude and zero phase angle.

$$Z(\omega) = |Z|exp(-i\psi) \tag{2.5.5}$$

References

[1] AlRashidi, M.R., El-Naggar, K. M., AlHajri, M. F., 2013. Parameters Estimation of Double Diode Solar Cell Model, *International Journal of Electrical, Computer, Electronics and Communication Engineering* 7(2): 93–96.

[2] Dobrzanski, L.A., Drygala, A., Giedroc, M., Macek, M., 2012. Monocrystalline silicon solar cells applied in photovoltaic system, *Journal of Achievements in Materials and Manufacturing Engineering* 53(1):7–13.

[3] Sad Basha, L., 2012. Analysis and evaluation tools development of Phothovoltaic modules and system performance under Jordanian and german climatic conditions, Cairo University. online Thesis and Dissertations

[4] Bostan, C.G., Dina, N., Bulgariu, M., Cracium, S., Dafinei, M., Chitu, C., Staicu, I., Antohe, S., 2011. Teaching/ learning photovoltaic in high school, *Romanian Reports in Physics* 63(2): 543–556.

[5] Toy, J., 2007. Are Photovoltaic Cells a Feasible Way to Alleviate the Worlds Dependence on Fossil Fuels?, *Fundamental Science and Technological Applications*

[6] Chaplin, D.M., Fuller, C.S., Pearson, G.L., 1954. A New Silicon p-n

Junction Photocell for Converting Solar Radiation into Electrical Power *Journal of Applied physics* 25 : 676.

[7] Jger, K., 2012. On the Scalar Scattering Theory for Thin-Film Solar Cells, *ISBN 978-94-6203-177-7 A digital copy is available at http: repository.tudelft.nl*

[8] Calnan, S., 2014. Applications of Oxide Coatings in Photovoltaic Devices, *Coatings* 4: 162–202 Sonya Calnan

[9] Sahay, A., Sethi, V.K., Tiwaric, A.C., Pandey, M., 2015. A review of solar photovoltaic panel cooling systems with special reference to Ground coupled central panel cooling system (GC-CPCS), *Renewable and Sustainable Energy Reviews* 42: 306–312

[10] Guman. 2015.Center for Solar Energy Reseach and Applications, Center of Excellence of Turkey on Solar Energy, [Accessed on 15 Feb 2016] *http://gunam.metu.edu.tr/index.php/solar-technology/pv-cell-types.*

[11] Europen Photovoltaic Industry Assosiation, 2011. Solar photovoltaic electricity empowering the world, [Accessed on 15 Feb 2016] *http://www.greenpeace.org/international/Global/international/publications/climate/201*

[12] Mayer, A.C., Scully, S.R., Hardin, B.E., Rowell, M.W., McGehee, M.D., 2007. Polymer-based solar cells, *Materials today* 10(11):30–33

[13] Chander, S., Purohit, A., Sharma, A., Nehrad, S.P., Dhaka, M.S., 2015. A study on photovoltaic parameters of mono-crystalline silicon solar cell with cell temperature, *Energy Reports* 1:104–109

[14] Copeland, A.W., Black, O.D., Garrett, A.B., 1942. The Photovoltaic Effect, *Chemical rewiews* 31(1): 177–226

[15] Alharbi, F.H., Kais, S., 2014. Theoretical Limits of Photovoltaics Efficiency and Possible Improvements by Intuitive Approaches Learned

from Photosynthesis and Quantum Coherence, *Renewable and Sustainable Energy Reviews* 43:1073–1089

[16] Shah, A., Moulin, E., Ballif, C., 2013. Technological status of plasma-deposited thin-film silicon photovoltaics, *Solar Energy Materials and Solar Cells* 119: 311–316

[17] Shockley, W., Queisser, H.J., 1961. Detailed Balance Limit of Efficiency of p-n Junction Solar Cells, *Journal of Applied Physics* 32:510–519

[18] Luque, A., Marti, A., Nozik, A.J, 2007. Solar cells based on quantum dots: multiple exciton generation and intermediate bands, *Mrs Bulletin* 32(03):236–241.

[19] Burschka, J., Pellet, N., Moon, S.J., Humphry-Baker, R., Gao, P., Nazeeruddin, M.K., Gratzel, M., 2013. Sequential deposition as a route to highperformance perovskite-sensitized solar cells, *Nature* 499: 316-319

[20] Snaith, H.J., 2013. Perovskites: the emergence of a new era for low-cost, high efficiency solar cells, *Journal of Physical Chemistry Letters* 4(21):3623–3630

[21] Carnie, M. J., Charbonneau, C., Davies, M. L., Troughton, J., Watson, T. M., Wojciechowski, K., Snaith, H., Worsley,D. A., 2013. A one-step low temperature processing route for organo–lead halide perovskite solar cells,*Chemical Communications* 49 (72): 7893–7895.

[22] (NREL),N. R. E. L., 2013.Best research-cell efficiencies, [Accessed on 15 Feb 2016] *https://commons.wikimedia.org/wiki/File:Best Research-Cell Efficiencies.png*online

[23] McGehee, M. D., 2013. Materials science: Fast-track solar cells, *Nature* 501(7467): 323–325.

[24] [Accessed on 16 Feb 2016]http:https:http://www.daviddarling.info/encyclopedia/M/AE multijunction device.html.

[25] Jo, G., Choe, M., Lee, S., Park, W., Kahng, Y.H., Lee, T., 2012. The application of graphene as electrodes in electrical and optical devices, *Nanotechnology* 23(11): 112001 (19pp)

[26] Credgington, D., Hamilton, R., Atienzar, P., Nelson, J., Durrant, J.R., 2011. Non-Geminate Recombination as the Primary Determinant of Open-Circuit Voltage in Polythiophene:Fullerene Blend Solar Cells: an Analysis of the Infl uence of Device Processing Conditions, *Advanced Functional Materials* 21(14):2744–2753

[27] Meyer, J., Hamwi, S., Krger, M., Kowalsky, W., Riedl, T., Kahn, A., 2012. Transition Metal Oxides for Organic Electronics: Energetics, Device Physics and Applications, *Advanced Materials* 24(40):5408–5427

[28] Alias, A.N., Zabidi, Z.M., Ali, A.M.M., Harun, M.K., 2013. Optical Characterization and Properties of Polymeric Materials for Optoelectronic and Photonic Applications, *International Journal of Applied Science and Technology* 3(5):11–38

[29] Das, T.K., Prusty, S., 2013. Graphene-Based Polymer Composites and Their Applications, *Polymer-Plastics Technology and Engineering* 52: 319–331

[30] Ossila, 2015. Perovskites and Perovskite Solar Cells, [Accessed on 16 Feb 2016] http://www.ossila.com/pages/perovskites-and-perovskite-solar-cells-an-introduction.

[31] Rose G, 1839. Beschreibung einiger neuen Mineralien des Urals, *annalen der physik*124 (12):551–573

[32] Attfield, J.P., Lightfoot, P., Morris, R.E., 2015. Perovskite, *Royal society of chemistry*, 44; 10541.

[33] Park, N.G., 2014. Perovskite solar cells: an emerging photovoltaic technology, *Materials* 18(2):65–72

[34] Yang, H.M., Park, C.W., Ahm, T., Jung, B., Seo, B., Park, H., Kim, J.D., 2013. A direct surface modification of iron oxide nanoparticles with various poly(amino acid)s for use as magnetic resonance probes, *Journal of Colloid and Interface Science*, 1;391: 158–167.

[35] Birol, H., Rambo, C.R, Guiotoku,M and Dachamir Hotza, D., 2013. Preparation of ceramic nanoparticles via celluloseassisted glycine nitrate process: a review, *Journal of Royal Society of Chemistry* 3:2873–2884

[36] Du, Y, Cai, H., Wu, Y., Xing, Z., Li, Z., Xu, J., Huang, L., Ni, J., Li, J., Zhang, J., 2017. Enhanced planar perovskite solar cells with effciency exceeding 16 percent via reducing the oxygen vacancy defect state in titanium oxide electrode, *Physical Chemistry Chemical Physics* 19 :13679–3686.

Chapter 3

Research techniques and device fabrication

In this chapter we discus research techniques used in this study. The experimental set-up, theory and layout of the methods used for characterization is also discussed.

3.1 An overview of standard characterization methods

Different characterization techniques were employed in this work to study different properties of synthesized perovskites materials. The crystal structure and crystallite size was determined using a Bruker-AXS D8 Advance X-ray diffractometer (Bruker Corporation of Germany) operating at 40 kV and 4 mA using Cu Kα = 0.15406 nm. The morphologies were obtained by using a field Scanning Emission Electron Microscope (FE-SEM), ZEISS SEM-Microscopes Crossbeam—540. The selected-area electron diffraction (SEAD) pattern were done by High resolution transmission electron microscopy (HRTEM) JOEL JEM 2100. The powders were uniformly dispersed in ethanol and sonicated for 30 min followed by drop casting the solution on carbon coated copper grid. Photoluminescence (PL) measurements were done using a Carry Eclipse Fluorescence spectrophotometer equipped with a 150W xenon (Xe) lamp. Raman studies of the prepared samples were performed using Raman Spectrometer,

Horiba Jobin Yvon T64000 with an excitation wavelength of 514 nm and a low power of 12 mW so as to minimize any heating effect. The optical properties were studied using a Perkin-Elmer Lambda 950 UV-Vis spectrometer. The thermal effect were studied using differential scanning calorimetry (DSC) and thermogravimetric analysis (TGA). To investigate the electrical properties of different perovskite solar cell fabricated, current-voltage measurements were done using solar simulator unit (Oriel Cornerstone, Newport) with Keithley 2400 series meter. The light intensity was calibrated using a standard silicon cell. All the I-V measurements were conducted at the light intensity of 1000 mW/m^2.

3.1.1 X-ray diffraction (XRD)

Operation

XRD is one of the commonly employed non-destructive technique in determining certain parameters such as the crystal structure, composition, quality, lattice parameters, orientation, defects, stress and strain in either powder or thin film form [1]. The XRD uses X-Ray (or neutrons) beam with a specific wavelength to probe the sample in order to determine the above-mentioned features [2]. During the measurement, X-Rays are directed towards the sample and proceed to elastically scatter off the electron clouds of atoms in the sample. The detector is then used to measure the X-Ray intensity as a function of the angle of a beam diffraction. A periodic structure within the sample leads to interference fringes determined by the periodic arrangement of the atoms. Thus, Bragg's Law plays a crucial role in the interpretation of these peaks.

$$\lambda = 2d\sin(\theta) \tag{3.1.1}$$

where d is the distance between the atomic planes, θ being the scattering angle, and λ being the wavelength of the incident X-Ray radiation.
However, by knowing the widths on the diffraction lines, crystal size, size distribution and strain of the crystals can be easily determined. The lattice

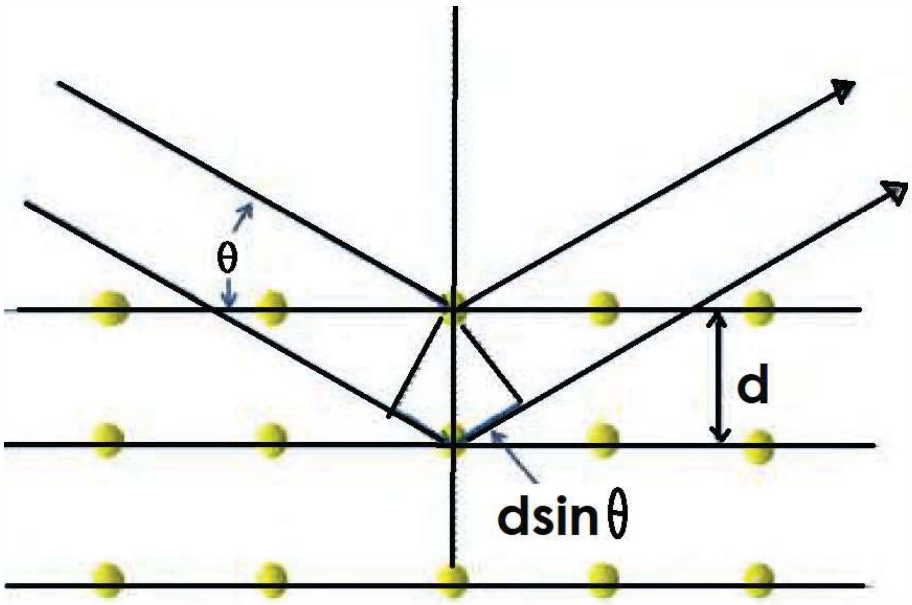

Figure 3.1: Schematic representative of Bragg's law

spacing and the crystal size of the sample is determined by using peak position and full width half maximum (FWHM). Another alternative way of determining the crystallite size of a sample is through using Debye-Scherrer equation which is given by

$$D = \frac{k\lambda}{\beta cos(\theta)} \tag{3.1.2}$$

Where D is the size of the crystallites, β is the full width at half maximum of a diffraction line located at angle θ while λ is the X-Ray diffraction wavelength of Cu K_α radiation (0.1514 Å and k is a Scherrer constant (0.94), which depends on the peak breadth, the crystallite shape, and the crystallite size distribution.

Types of X-ray spectra found on XRD

When the sample is bombarded with the stream of electrons accelerated with high energy from the filament it results in two types of X-Ray spectra being generated. The first type being continuous and the second type being characteristic spectra. The continuous spectra are produced when the electrons hit the targeted sample, and are characterized by the wide range of wavelengths

X-Rays depending on the targeted material and voltage across the X-Ray tube. However, when the applied voltage is raised above a critical value, characteristic of the target metal display a sharp intensity maxima in the spectrum. Since they are so narrow and since their wavelengths are characteristic of the target metal used, they are called characteristic lines. These 'characteristic lines' and they are produced by exciting an electron out of its shell (only K lines are used in x-ray diffraction due to absorption). The K_α lines are produced as an electron from one of the outer shells falling into the vacancy created in the K shell, thereby emitting energy in the process as x-rays. The characteristic spectra are produced when the electronic transition occurs amongst individual atoms of the targeted specimen as a result of high voltage. Figure 3.2 shows the comparison between the two spectra, the characteristic X-rays have a much higher intensity compare to continuous spectra. This type of spectra is defined more by Bohr model of atoms [3].

Experimental Setup

The final crystal structure and crystallite size of the synthesized materials and fabricated devices were determined using a Bruker-AXS D8 Advance X-ray diffractometer (Bruker Corporation of Germany) operating at 40 kV and 4 mA using Cu $K\alpha = 0.15406$ nm.

3.1.2 Scanning electron microscopy (SEM)

Operation

Scanning electron microscopy (SEM) is among the most powerful surface technique that provide information on the specimen or substrate such as composition, topology, and crystallography [5]. It is a very good technique for investigating the surface morphology of nanoparticles. SEM uses electron beam generated by tungsten or lanthanum hexaboride to probe a sample [6]. An electron beam is accelerated and directed using positively charged wire grids, and focused using electrostatic and magnetic field lenses. As

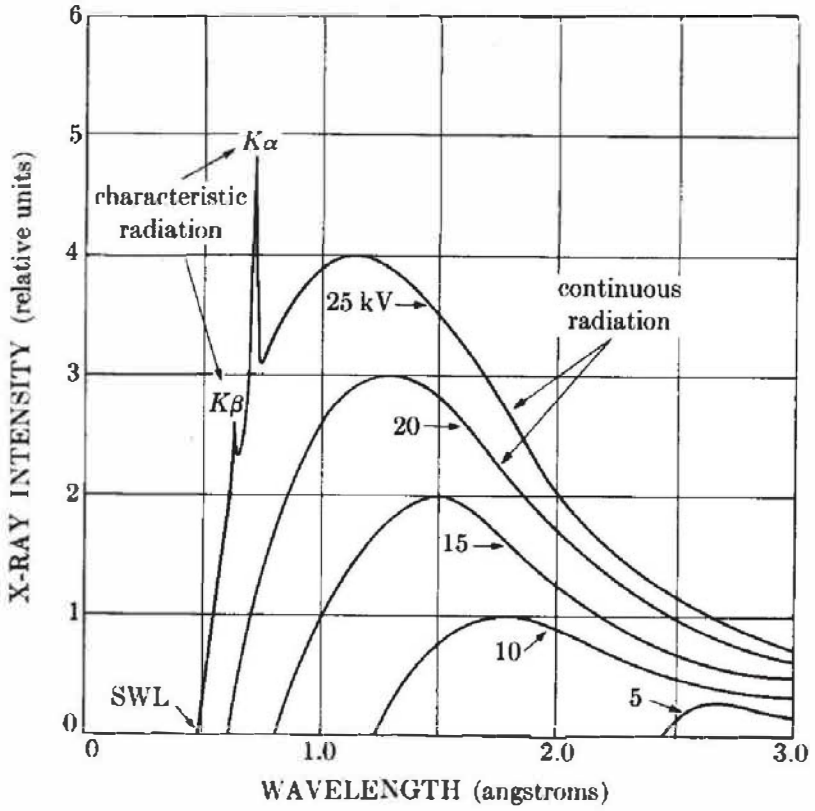

Figure 3.2: X-ray spectrum of Mo at different voltage [3]

the electron beam is systematically scanned over the sample, it results in dissipation of the electron beam energy in the near surface region of the sample thus low energy secondary electrons, backscattered electrons (BSE), auger electrons, characteristic x-ray and continuum x-ray can be detected by an electron detector.

The signal from low energy secondary electrons is then used to create the image of the analyzed sample. Secondary electrons give the most valuable information about the morphology and topography of the analyzed material while backscattered electrons provide valuable information in terms of illustrating contrasts in composition of multiphase samples. X-Ray generation is produced by inelastic collisions of the incident electrons with electrons in shells of atoms in the sample. As the excited electrons return to lower energy states, they yield X-Rays of a fixed wavelength. Thus, characteristic X-Rays are produced for

each element in a sample that is "excited" by the electron beam. Depending on the instrumental aperture and resolution, the maximum magnification for an SEM can be as large as one million times, thus allowing the clear observation of atomic clusters and nanostructures. It should be pointed out that the image resolution that is given by SEM largely depends on the interaction of electron probe with the specimen. Figure 3.3 shows both components and working principle from scanning of the sample up to data acquiring.

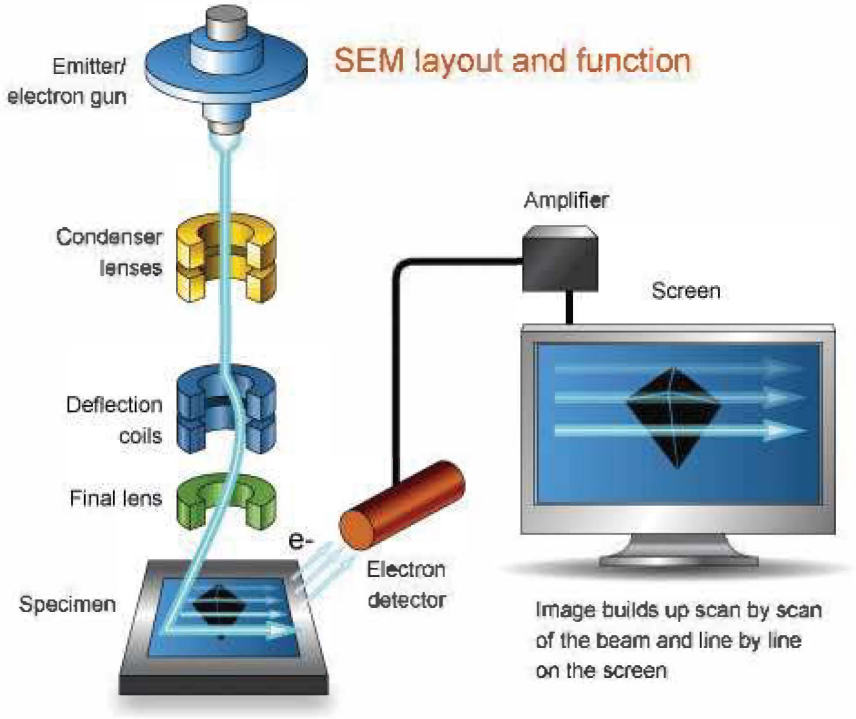

Figure 3.3: Schematic diagram showing components and working principle of SEM [4]

Experimental Setup

The morphologies of organic, inorganic materials and perovskite devices were obtained using a field SEM (FE-SEM), Zeiss SEM-Microscopes Crossbeam 540.

3.1.3 Energy Dispersive X-ray Spectrometry (EDS)

Operation

EDS spectrometer is the most commonly employed analytical technique in the elemental analysis of the solid samples [7]. It uses a high-energy focused beam of electrons produced by thermionic sources such as a tungsten hairpin exaboride (LaB6) crystal to irradiate the solid surface in order to obtain the localized chemical analysis. Its characterization capabilities are due in large part to the fundamental principle that each element has a unique atomic structure allowing a unique set of peaks on its X-ray spectrum. Based on the principle, EDS is capable of detecting all the elements present in the analyzed sample with the atomic number 4 (Be) to 92 (U) [8].

There are two analysis methods that are associated with EDS spectrometer namely, qualitative and quantitative analysis. Qualitative analysis is regarded as a first step of analyzing an unknown sample by identifying the elements present on the obtained X-Ray spectra using tables of energies or wavelengths. Quantitative involves the determination of the concentration of the elements present in the sample by measuring the intensities of each element line that appears on the X-Ray spectra and compare it with a calibrated standards of known composition. In the analysis, only peaks which are statistically significant should be considered for identification because the higher the peak in the spectrum the more concentrated the element is in the specimen.

Experimental Setup

Elemental analysis or chemical characterization of the synthesized samples were obtained using EDS coupled in Joel JSM-9800F Field emission scanning electron microscope (FE-SEM).

3.1.4 Transmission electron microscopy (TEM)

Operation

Transmission electron microscopy is an imaging technique in which a beam of electrons is transmitted through a specimen, and then an image is formed. The image is then magnified and directed to appear either on a fluorescent screen or to be detected by a sensor such as a charge-coupled device (CCD) camera. The system can study small details down to near atomic level. It can investigate the size, shape and arrangement of the particles which make up the specimen as well as their relationship to each other on the scale of atomic diameter. Materials to be analyzed with this technique needs to be have dimensions small enough to be electron transparent and that can be produced by the deposition of dilute suspension containing the specimen onto support grids. The suspension is normally a volatile solvent such as ethanol that can evaporate to allow the specimen to settle on the grids. Figure 3.4 shows the schematic diagram of TEM, showing the position of electron gun, electromagnetic lenses, specimen stage and imaging system.

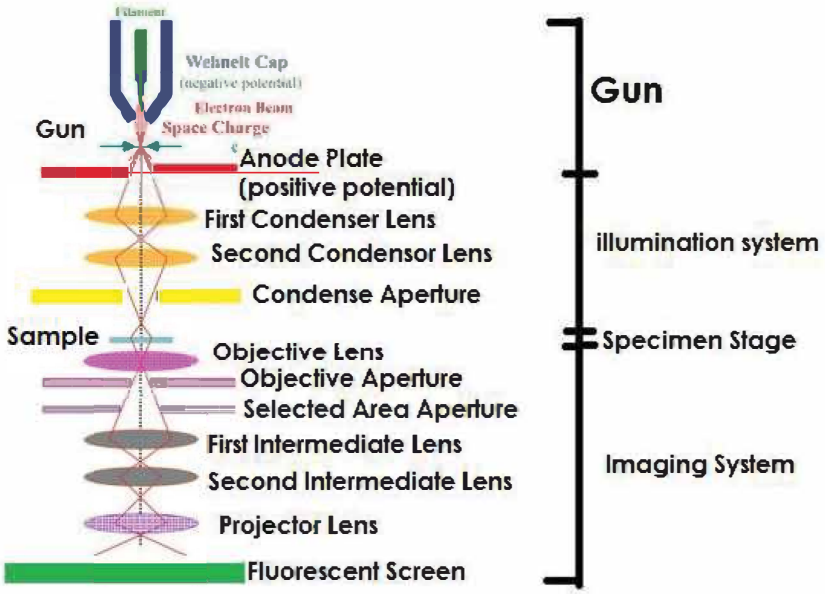

Figure 3.4: Schematic diagram showing components of TEM [9]

Experimental Setup

The SEAD patterns were done using HRTEM (JOEL JEM 2100). The powders were uniformly dispersed in ethanol and then sonicated for 30 min before being drop cast onto a carbon-coated copper grid.

3.1.5 Differential scanning calorimetry (DSC)

Operation

Differential scanning calorimetry is the most popular thermal analysis technique of thermal analysis. DSC measures the heat required to maintain the same temperature in the sample and an appropriate reference material during controlled heating. DSC can be used to study thermal transitions of perovskite precursors such as PbI_2. These transitions include the melting, crystallization, and degradation or decomposition.

Experimental Setup

DSC analysis was performed using a Perkin Elmer Pyris differential scanning calorimeter under the nitrogen atmosphere (flowing rate of 20 ml min $^{-1}$). The instrument was calibrated using the onset temperatures of zinc and indium standard and the enthalpy of indium. During the heating of a sample, for example, from room temperature to its decomposition temperature, peaks with positive and negative heating and cooling may be recorded; each peak corresponds to a heat effect associated with a specific process, such as crystallization or melting.

3.1.6 Thermogravimetric analysis (TGA)

Operation

Thermogravimetric analysis (TGA) is one of the members of the family of thermal analysis techniques used to characterize a wide variety of materials. TGA provides complimentary and supplementary characterization information to the most commonly used thermal technique, DSC. TGA analysis is a

technique where the mass of a sample is measured as a function of temperature or time while the sample is subjected to a controlled temperature program in a controlled atmosphere. The heart of the TGA analyzer is the thermobalance, which is capable of measuring the sample mass as a function of temperature or time.

A purge gas, such as nitrogen, flowing through the balance creates an inert atmosphere. TGA can directly record the changes in mass due to dehydration, decomposition, or oxidation of a sample as a function of time and temperature. TGA is mostly used to study the decomposition, thermal stability and ash content of various nanomaterials and nanocomposites. TGA measurements provide valuable information that can be used to select materials for certain end-use applications, predict product performance and improve product quality.

Experimental Setup

In this study, TGA examinations were performed utilizing a Perkin Elmer TGA7 thermogravimetric analyzer, under the nitrogen air at a stream rate of 20 ml/min

3.1.7 Fourier-transform infrared (FTIR)spectroscopy

Operation

Fourier-transform infrared spectroscopy is a technique that is used to identify types of chemical bonds or functional groups in a molecule. During the analysis, Infrared radiation (IR) radiation passes through a sample and produces an infrared absorption spectrum like a molecular "fingerprint". FTIR can be used to identify bonds in unknown material including solids, liquids, gasses, semi-solids, powders, polymers, organics, inorganics. Advantages of an FTIR analysis include its high speed, sensitivity, mechanical simplicity and inexpensiveness [10].

Experimental Setup

FTIR spectroscopy was performed using a Perkin Elmer Spectrum 100 Fourier-transform infrared spectrophotometer. The samples were analysed in an attenuated total reflectance (ATR) detector in a 400 – 4000 cm^{-1} wavenumber range at a resolution of 4 cm^{-1}.

3.1.8 UV-Vis spectrometer

Operation

UV-Vis spectrometry is a non destructive technique which measures the light intensity when passes through the sample and compare it to the light intensity before it passes the sample. The operation of UV-Vis spectrometry is shown in Figure 3.5. The principle of UV-Vis spectroscopy is based on the ability of

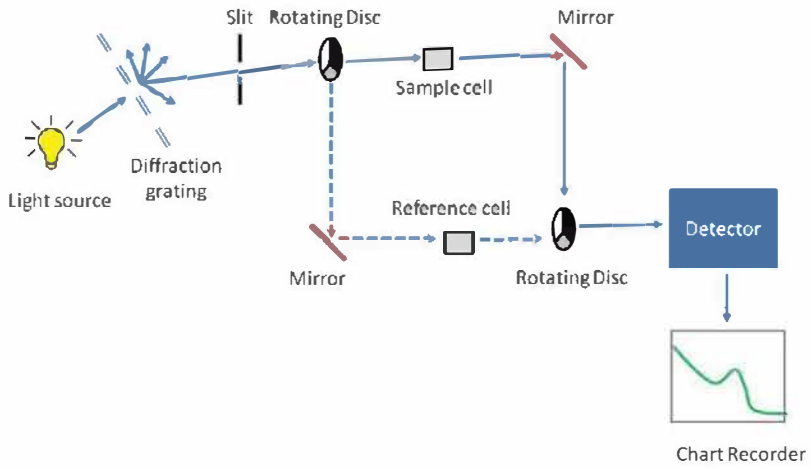

Figure 3.5: Schematic representation of UV-Vis operation,[11]

the material to absorb ultraviolet and visible light. The relationship between the input and output intensity is described by Beer-Lambert Law (Equation 3.1.3)

$$e^{-A} = (I/I_o) \tag{3.1.3}$$

The absorbance, A, can be divided by the path length, l, to yield the absorption co-efficient α which quantifies the absorbance per metre thus taking

film thickness into account. The spectroscopy consist of light source, a sample holder, a diffraction grating which separates the different wavelengths of light, and a detector. The radiation source normally a Tungsten filament(300-2500 nm) and a deuterium arc lamp which is continuous over the ultraviolet region (190-400 nm). The detector is typically a photodiode or a charge couple device (CCD). Photodiodes are used with monochromators, which filter the light so that only a single wavelength reaches the detector. Diffraction gratings are used with CCDs, which collects light from the different wavelengths on different pixes.

Experimental Setup

The optical properties were studied using the Perkin-Elmer Lambda 950 UV-Vis spectrometer. Before the measurement, the absolute reflectance of the samples was calibrated using a standard sample. Experimental data were collected within the 250800 nm range with 1 nm step and 0.5 s integration time.

3.1.9 Raman Spectroscopy

Operation

Raman spectroscopy is a non-destructive, optical method of material analysis. Characteristics of a sample are obtained by analyzing monochromatic light that has undergone inelastic scattering upon interaction with the sample. In general, there are three possible outcomes that may occur when light is incident on matter: the light may be absorbed, scattered, or have no interaction at all. If light interacts with a material and is not absorbed, it is considered scattered.

There are additionally, two main classifications of scattering. (i) If a monochromatic radiation of given frequency ω is incident on a surface and is elastically scattered without any change of frequency, it is classified as Rayleigh scattering, whereas (ii) if the scattering is inelastic and the collected light contains a different

frequency, it is referred to as having been Raman scattered [12]. In order to adequately describe the scattering mechanisms using the energy transfer model, some quantum mechanical definitions are required. The first is the definition of a photon. A photon is the basic unit of electromagnetic radiation. It can be thought of as a quantum or particle of light that has energy (Equation 3.1.4)

$$E = hv \tag{3.1.4}$$

where h is Plancks constant and v is the frequency of the light.

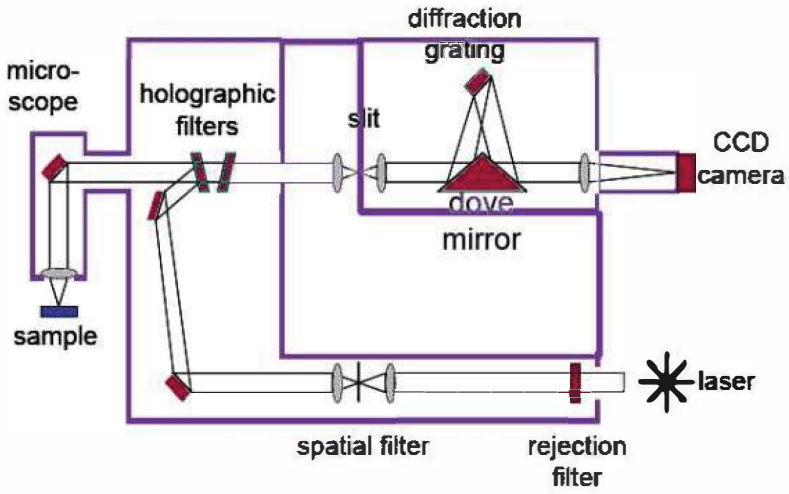

Figure 3.6: Schematic diagram of a Raman spectrometer, [12]

In modern Raman spectrometers (Figure 3.6), lasers are used as a photon source due to their highly monochromatic nature, and high beam fluxes. This is necessary as the Raman effect is weak, typically the Stokes lines are ≈105 times weaker than the Rayleigh scattered component. In the visible spectral range, Raman spectrometers use notch filters to cut out the signal from a very narrow range centred on the frequency corresponding to the laser radiation. Most Raman spectrometers for material characterization use a microscope to focus the laser beam to a small spot (<1–100 mm diameter). Light from the sample passes back through the microscope optics into the

spectrometer. Raman shifted radiation is detected with a charge-coupled device (CCD) detector, and a computer is used for data acquisition and curve fitting. These factors makes Raman spectroscopy a very sensitive and accurate technique.

Experimental Setup

The Raman investigations of all samples reported in the present work was performed utilizing Raman Spectrometer Jobin Yvon, Horiba TX64000. An excitation wavelength of 514 nm was utilized at an intensity of 0.012 watts, and LWX50 and LWX100 magnifying instrument objective were utilized for centering. A couple of milligrams of the sample were put into a little aluminum test cup, the laser light with an intensity of 100 mW was introduced and centered around the sample, and the scattered radiation was gathered at 180^o.

3.1.10 Solar Simulator

Operation

The organic solar cells in this study were characterized using a solar simulator equipped with a keysight keithley source meter. It is a source measurement unit (SMU) instrument designed specifically for test application that demand tightly coupled sourcing and measurements. The source meter is used with Oriel xenon lamp (150 W) coupled with AM1.5 filter to simulate sunlight. The light intensity is calibrated with indiumtin oxide (ITO)/ fluorine-doped tin oxide (FTO) cell with KG2 filter following the standard solar cell testing procedures.

Proper integration between software, solar simulator and reference cell is necessary to achieve accurate repeatable data to calculate the PV-cell efficiency. Once the solar simulator and other instruments are turned on and the solar cell is placed beneath the simulator, the software will open the solar simulator shutter, sweep the voltage across the prescribed range, measure the current and display the I-V curve on the computer as shown in Figure 3.7. The software

also calculates the PV parameters including the power conversion efficiency (PCE).

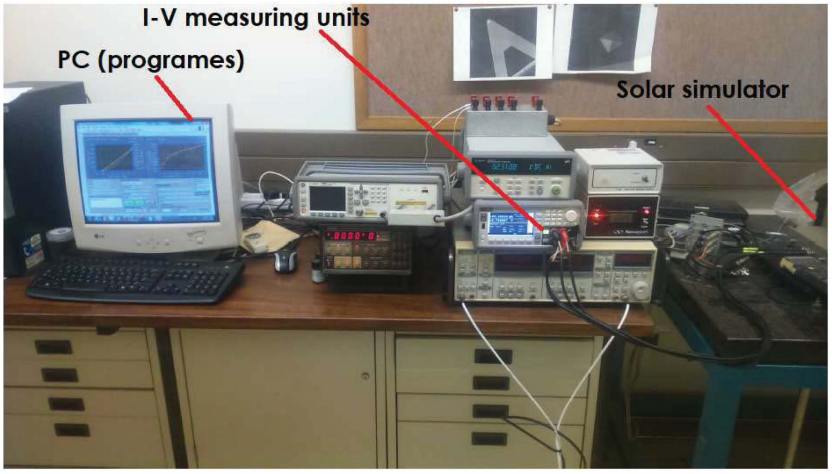

Figure 3.7: Solar Simulator equipped with Keithley 2400 source meter

Experimental Setup

To investigate the electrical properties of different perovskite solar cell fabricated, current-voltage measurements were done using SMU (Oriel Cornerstone, Newport) with Keithley 2400 series meter. The light intensity was calibrated using a standard silicon cell. All the I-V measurements were conducted at the light intensity of 1000 mW/m^2. A Meter/DC (HP 4140B pA) Voltage Source with a current sensitivity as low as 10–14 A was used for measurement with the voltage scan size from -2 V to +2 V. In this system, the sample stage was enclosed in a black light-tight metal box allowing only dark current to be measured and minimizing electrical noise.

3.2 General processing techniques

3.2.1 Cleaning the ITO/FTO glass substrate

Pre-patterned ITO/FTO glass substrates were sonicated for 10 minutes in soap solution and rinsed with deionized water. The as-prepared substrates

were then sonicated for 5 minutes in acetone and ethanol in each, followed by drying using a nitrogen gas.

3.2.2 Spin coating

Spin coating is by far proven to be the simple and precise method that uses centrifugal force to produce a uniform thin film ranging from 20 to 300 nm in thickness. The layer thickness can be varied based on the number of spin coatings done. However the are also other variables that can be varied to control the thickness of the film such as solvent concentration, spin speed and spin time. During spin coating, the volatile solvent is evaporated and typical spin time is 30 second to 2 minutes. Figure 3.8 shows the Laurell WS Series spin coater that was used in this thesis.

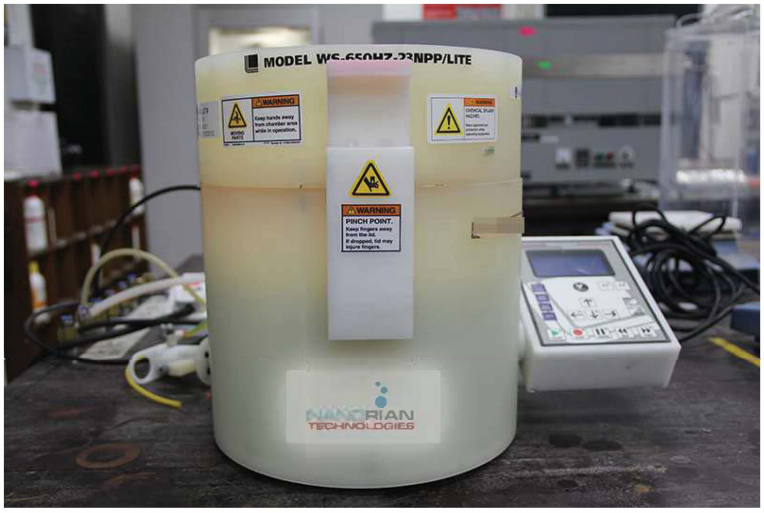

Figure 3.8: Spin coater

3.2.3 Thermal vacuum Evaporator

Thermal evaporation is a method of depositing a thin film of metal or small molecule organic semiconductors. The photograph of vacuum evaporator is shown in Figure 3.9. The variables to control the metal evaporation are vacuum chamber pressure, source material purity and evaporation power which is correlated with the evaporation rate. The pressure of the vacuum chamber

Figure 3.9: Vacuum evaporator

should be maintained between 4×10^{-4} to 5×10^{-7} torr to ensure good quality deposition. The deposition rate varies from 0.4 to 3 $\mathring{A}$ in most investigations and source materilas should be evaporated slowly to protect the sub-layer which can be damaged by hot vapors.

3.3 Material Synthesis and Device Fabrication

This sections highlight different methods of synthesis undertaken in this study to synthesize different organic and inorganic materials. It also covers the fabrication of perovskite devise. Compared with the methodology of traditional semiconductors, the fabrication of perovskites samples is relatively easy. Because they need neither series of cumbersome equipment nor strict environment condition but can be synthesized and deposited simply by soft chemical methods at room temperature, it is possible to design the perovskites as we want by working on the organic part.

3.4 Synthesis of PbI_2 using anode and cathode

Metallic lead (Pb) anode and lead dioxide (PbO_2) cathode material were extracted from one cell of a depleted sealed-lead acid gel (SLAG) battery.

The un-purified yield Pb and PbO_2 were 66.8 g and 89.0 g respectively. Two routes were taken to synthesize PbI_2. The first used the anode and the second the cathode.

3.4.1 Synthesis of PbI_2 using anode

The anode material was soaked in hot water for 1 hr three times to remove the combining gel from the surface. Immediately after washing, the metallic lead was oven dried for 1 hr at 80 ^oC and allowed to cool at room temperature. The metallic lead was then broken up into small pieces and placed in a 500 mL glass beaker. The glass beaker was placed on a pre-heated hot plate and 40 mL of concentrated nitric acid (55%) was poured drop wise into the beaker and allowed to boil under gentle magnetic stirring. When no further reaction of lead and acid was visible, 20 mL of deionized water was added to create a dilute solution and the precipitate was decanted and collected. The un-reacted metallic was subjected to the same procedure until no further lead remained. The process was repeated three times resulting in four white $Pb(NO_2)_2$ samples in four different beakers. A solution of potassium iodide (KI) was prepared by dissolving 10 g of potassium iodide powder in a 50 mL of deionized water. The KI was added into $Pb(NO_2)_2$, giving yellow PbI_2 solution. The reaction Eq. 3.4.1 and Eq. 3.4.2 respectively, describe the two synthetic routes. The solution was then washed with deionized water and dried at 300 ^oC for 1 hr resulting in a yellow, dry PbI_2 powder. The samples were then allowed to cool naturally at room temperature prior to characterization.

$$3\ Pb + 8\ HNO_3 \rightarrow 3\ Pb(NO_3)_2 + 2\ NO + 4\ H_2O \tag{3.4.1}$$

$$Pb(NO_3)_2 + 2KI \rightarrow 2KNO_3 + PbI_2 \tag{3.4.2}$$

3.4.2 Synthesis of PbI_2 using cathode

PbI_2 may also be synthesized using the cathode precursor and acetic acid according to:

$$PbO + 2\ CH_3COOH \rightarrow Pb(CH_3COO)_2 + H_2O \tag{3.4.3}$$

$$Pb(CH_3COO)_2 + 2\ KI \rightarrow PbI_2 + 2\ CH_3COOK \tag{3.4.4}$$

The collected lead dioxide (PbO_2) was washed with deionized and oven dried for 1 hr at 80 ^{o}C. After drying, 34.66 g of (PbO_2) was annealed at 600 ^{o}C for 5 hrs resulting in lead oxide (PbO). The obtained PbO was mixed in 50 mL of acetic acid in a glass beaker. The solution was allowed to boil on a hot plate while magnetically stirring. The precipitated of $Pb(Ch_3COO)_2$ was collected and dried at 80 ^{o}C for 1 hr and then mixed in a glass beaker with a solution of KI prepared by dissolving 10 g of potassium iodide powder in a 50 mL of deionized water. The solution was heated until the liquid solution is completely boiled. The precipitate was then collected and oven dried for 50 mins. The sample was allowed to cool naturally at room temperature resulting in a homogeneous powder for characterization. Four samples were then subjected to post-melting temperature at 500 ^{0}C at varying annealing times to produce rare 6R polytype PbI_2.

3.4.3 Synthesis of ZnO Nanomaterials

Nanocrystals of anatase TiO_2 were synthesized using the hydrothermal method. The gel was prepared by mixing 45 mL of deionized water with 15 mL of HCl (Sigma-Aldirich) under constant starring for 5 min in a fume hood. 2 mL of titanium (IV) isopropoxide (Sigma-Aldirich) was added to the solution under a constant stirring for 10 min. The mixture was transferred into a preheated autoclave oven at 100 ^{o}C for 2 hrs and then allowed to cool to room temperature before centrifugation. The collected white particles were washed several times using deionized water. The as-prepared TiO_2 nano-powders were

separated into three samples and annealed at 200 ^{o}C, 400 ^{o}C and 600 ^{o}C. While ZnO nanorods were synthesized on indium tin oxide (ITO) substrate seed-layer assisted Chemical Bath deposition (CBD). The ITO substrates were thoroughly cleaned using a warm soap solution, rinsed in deionized (DI) water, followed by acetone, ethanol and DI water by sonication for 10 minutes each. The sol-gel for seed layer was prepared by dissolving zinc acetate dihydrate ($Zn(CH_3COO)_2.2H_2O$, Merck) in ethanol giving a 30 mM solution. The solution was then aged for 24 h. Cleaned ITO substrates partly covered using a non-sticking, heat resistant tape and then spin-coated at 3000 rpm for 1 min to form ZnO seed layer. The layer was then dried at 200 ^{o}C for 5 min. The above procedure was done four times in order to increase the thickness of ZnO seed layer. Finally, the spin coated ZnO seed layer was annealed in air at 400 ^{o}C for 60 min. The growth solution of the nanorods was prepared by dissolving equimolar amounts (35 mM) of zinc nitrate hexahydrate ($Zn(NO_3)_2.6H_2O$; 98%, Sigma Aldrich) and hexamethylenetetramine (HMT; 99.5 %, Sigma Aldrich) in DI water. The growth of nanorods was done by suspending substrates (using nylon cable ties) with the seeded surface facing downwards in the beaker containing the growth solution. The beaker was then placed in a water bath at 90 ^{o}C with an error of 1 for 60 min. After the growth, the substrates were immediately removed from the growth beaker, washed with DI water and annealed at 400 ^{o}C for 30 min.

3.4.4 Synthesis of Methylammonium iodide (CH_3NH_3I) Nanomaterials

CH_3NH_3I was synthesized by reacting 27.86 ml methylamine (40% in methanol, Aldrich) and 30 ml hydroiodic acid drop wise (57 wt% in water, Aldrich) in a 250 ml round-bottomed flask at 0 ^{o}C for 2 h with stirring. The precipitate was recovered by evaporation at 50 ^{o}C for 1 h. The product, methyl ammonium iodide (CH_3NH_3I), was dissolved in ethanol, recrystallized from diethyl ether,the process was repeated three times to signify purity and dried at 60 ^{o}C in a

vacuum oven for 24 h.

3.4.5 Device Fabrication

Compared with the methodology of traditional semiconductors, the fabrication of perovskites samples is relatively easy. Because they need neither series of cumbersome equipment nor strict environment condition but can be synthesized and deposited simply by soft chemical methods at room temperature, it is possible to design the perovskites as we want by working on the organic part. Two pervoskites having the same chemical formula, but using two different lead iodide polytypes were synthesized for the purpose of comparison. The experimental description is therefore in two parts. Experimental 1 describes the synthesis route for the perovskite based on the rare PbI_2 form of lead iodide. This polytype has lattice parameter C(6R) 20.937 Å. Experimental 2 employs commercially sourced PbI_2 with a lattice parameter C (12R) 41.874 Å.

Experimental 1

Three drops of $MAPbI_3$ solution were dropped on the ZnO nanorods coated substrate (ITO). The substrate was spun at 3000 rpm for 60 s and dried in a pre-heated oven at 100 ^oC for 10 min. A hole transporting layer was formed by spin coating poly (3, 4-ethylenedioxythiophene) polystyrene sulfonate (PEDOT: PSS) solution at 3000 rpm for 30 s. Finally, a thermal evaporator was used to deposit 100 nm of Au at a deposition rate of 0.2 nm/s using (i) a finger-like Shadow mask with an active area of 0.6 cm^2 to check response to illumination, and (ii) a circular Shadow mask having a diameter of 0.8 mm for Schottky diode of the form of ITO/ZnO/perovskites. Figure 3.10 is a photograph of the completed devices based on the Shadow masks (i) and (ii) respectively.

Figure 3.11 shows the steps in the perovskite device fabrication in this work.

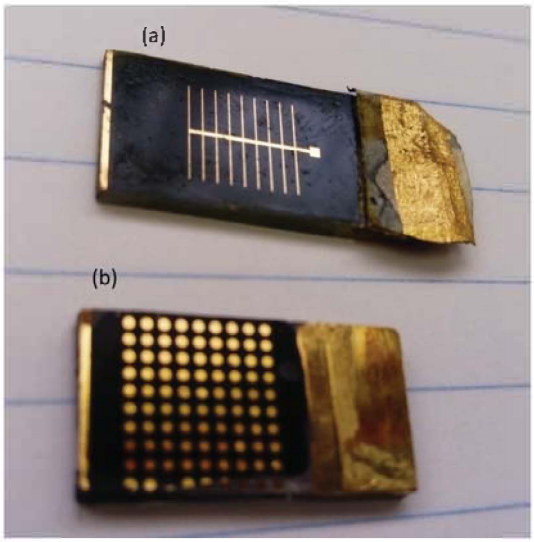

Figure 3.10: A low resolution photograph of Shadow masks used in the Au electrode deposition (a) finger-like, and (b) circular (see text).

Experimental 2

A two step method was used to deposit $MAPbI_3$ solution in the ITO substrate coated with ZnO nanorods. A 1M PbI_2 solution was prepared by dissolving 4.66 g of 12R polytype PbI_2 (Sigma Aldrich) in 10 ml of N,N-dimethylformamide (DMF). The solution was kept at 70 ^oC for 2 h under constant stirring. Three drops of PbI_2 solution was spin coated on ZnO nanorods substrate at 3000 rpm for 60 s and dried in 100 ^oC for 10 min. MAI solution (Sigma Aldrich) was dropped on the substrate, a wait of 20 s was observed and the substrate was spun at 3000 rpm for 60 s and dried for 10 min in 100 ^oC. A hole transporting layer was formed by spin-coating the poly(3,4-ethylenedioxythiophene) polystyrene sulfonate solution at 3000 rpm for 30 s. Finally, 100 nm of Au was deposited using thermal evaporator at a deposition rate of 0.2 nm/s. Figure 3.12 shows the steps taken in this work to fabricate the final perovskite device.

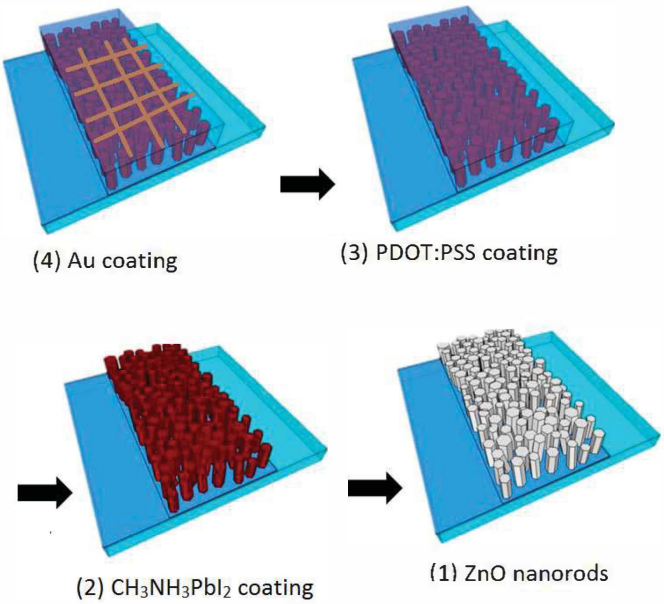

Figure 3.11: Typical fabrication procedure for lead halide perovskite devices

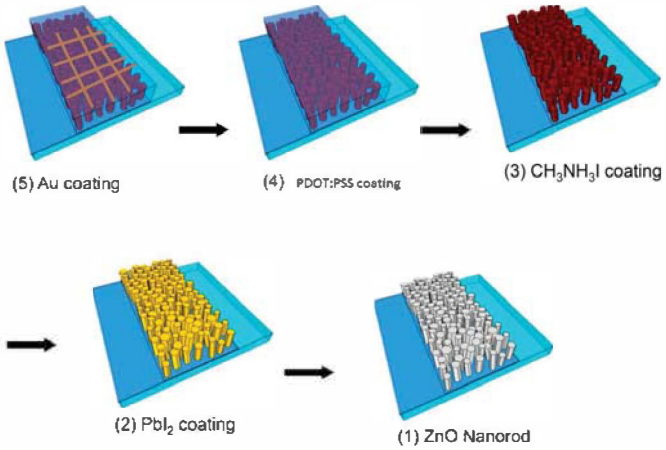

Figure 3.12: Fabrication of 6R polytype based lead iodide perovskite device.

References

[1] Wong, C.S., Bennett, N.S., Manessis, D., Danilewskyc, A., McNally, P.J., 2014. Non-destructive laboratory-based X-ray diffraction mapping of warpage in Si die embedded in IC packages, *Microelectronic Engineering* 117:48–56.

[2] Ben Raben, M., Chaglabou, N., kanzari, M., Bezig, B., 2009. Structural and optical studies on antimony and zinc doped CuInS2 thin films, *Journal of Physics Procedia* 2(3):745–750.

[3] Bohr, N., 1913. On the Constitution of Atoms and Moleculess, *Philosophical Magazine* 6(6):1–25

[4] Myscope., 2014. Training for advance research, [Accessed on 7 March 2014]*Australian microscopy and microanalysis research facility.* Online. http://www.ammrf.org.au/

[5] Chiang, C.-T., DeLeon, R.L., Garvey, J.F., Preparation of Zinc Oxide Thin Films by Reactive Pulsed Arc Molecular Beam Deposition, *Journal of Physical Chemistry* 111 (48): 17700–17704

[6] Chung, B.-H., Kim, S.J., Choi, M. S., Jang, D.Y., 2013. Design and fabrication of a scanning electron microscope (SEM) with an electrostatic column for process embedment, *Journal of the Korean Physical Society* 63(7): 1287–1290

[7] Song,Yongxiu., Zhu, Jiaxiang., Xu, Hui., 2014. Synthesis, characterization and visible-light photocatalytic performance of

Ag_2CO_3 modified by graphene-oxide, *Journal of Alloys and Compounds* 592: 258–265

[8] Sperandio, C., Arnoult, C., 2010. Characterization of the interphase in an aluminium/epoxy joint by using controlled pressure scanning electron microscopy coupled with an energy dispersive X-ray spectrometer, *Micron* 41(2): 105–111

[9] [Accessed on Sep 2014] http:https://sites.google.com/site/bsatpati/tem, online. January 2018.

[10] Lu, H., Hu, Y., Li, M., Chen, Z., Fan. W., 2006. Structure characterization and thermal properties of silane-grafted-polyethylene/clay nanocomposites prepared by reactive extrusion, *Composites Science and Technology*, 66:3035-3039.

[11] [Accessed on Sep 2014]http://cnx.org/contents/ba27839d-5042-4a40-afcf-c0e6e39fb454@19.1:100, online. September 2014

[12] Begum, N., Bhatti, AS., Jabeen, F., Rubini, S., Martelli, F., 2010. SPhonon Confinement Effect in III-V Nanowires, *InTech*

Chapter 4

Synthesis and characterization of PbI_2 samples

4.1 Overview

In this chapter we present the properties and synthesis of nanosized PbI_2 particles. High-quality lead iodide (PbI_2) nanoparticles were synthesized from both anode and cathode of a discarded sealed lead-acid accumulator as starting materials. Their crystal structure, morphology, chemical composition and optical properties are discussed. The XRD measurements indicated the presence of pure hexagonal PbI_2 nanoparticles. Application of the Scherrer equation indicates crystal sizes between 13.70 and 14.32 nm. SEM indicated the presence of spherical particle agglomerations between 1.5 and 3.5 μm in diameter. The measured band gap using two methods was consistent at 2.75 eV. EDS results suggest the absence of impurities in the synthesized nanoparticles. The overall results suggest that discarded sealed lead-acid accumulators can source pure hexagonal phase lead iodide nanoparticles with potential applications in perovskite solar cells.

4.2 Introduction

PbI_2 is a lamellar semiconducting solid comprising lead and iodide ion layers in covalent bonding. Weak van der Waals interactions hold these layers together

in a three-dimensional hexagonal close-packed (hcp) array of iodide anions with alternate layers of octahedral lattices with lead (II) cations interstitially sited. Figure 4.1 shows the layered crystal structure of PbI_2.

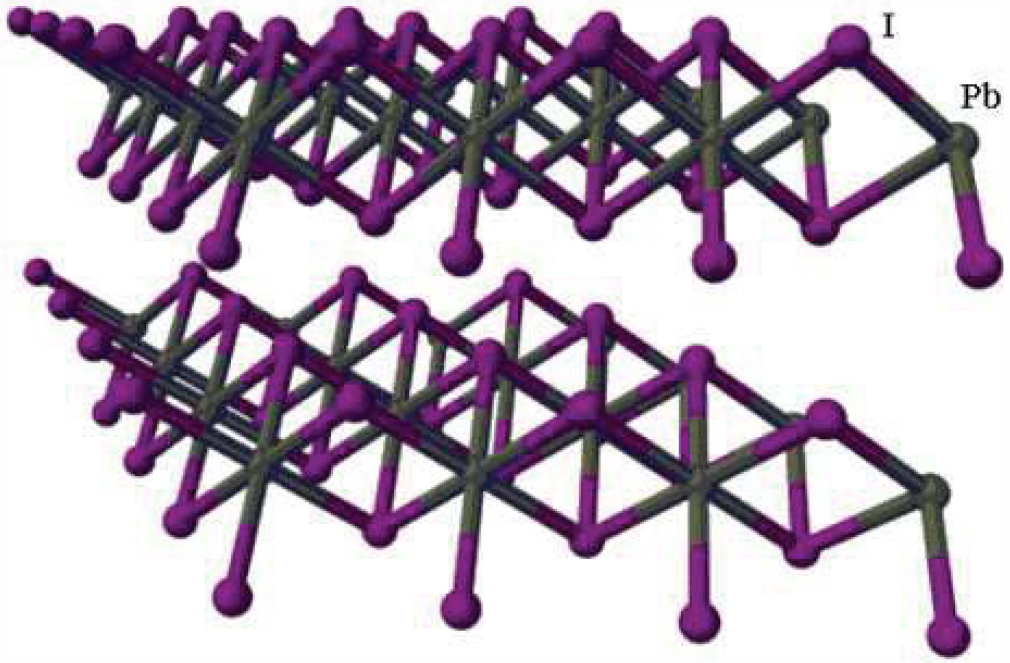

Figure 4.1: Layered structure of PbI_2 [1]

The lattice consists of a repeating I-Pb-I sequence [3] with high atomic number ($Z_{Pb} = 82$, $Z_I = 53$) and intrinsic band gap of about 2.4 eV. These properties make it a potential candidate for room-temperature, direct detectors of low energy ionizing x- and γ- rays [1]. There is a growing interest in the use of this material in lead-based perovoskite solar cells. The economical application to solar cells depends highly on the ease of fabrication and growth processes and on the purity and yield of PbI_2 [4]. It is generally believed that the properties of PbI_2 depend not only on their chemical purity, but also on precise chemical structure, phase, morphological distribution and dimensionality. A challenging issue presently faced in materials synthesis is the problem of controlling the mesoscopic anisotropy in inorganic materials.

Extensive studies of the influence of purity of precursor PbI_2 powders on single bulk crystal growth have reported varying degrees of success in the literature [5]. Examples of currently used methods that yield micro- or nano-PbI_2 structures are low temperature colloidal processes [12], reverse micelles methods [13], vapor-transporting methods [14], hydrothermal [15] and vapor deposition [3]. The hydrothermal method is considered the method of choice to prepare the bulk nanoparticle semiconductor with well-controlled morphologies at lower temperature using a one-step procedure [10].

In this work, PbI_2 nanoparticles bulk have been synthesized from both the anode and the cathode of a discarded sealed lead-acid accumulator cell (SLA). This route is potentially economically viable from the perspective of both source material and processing costs. Lead is a well-known environmental hazard and its safe disposal presents a perpetual challenge in the light of its abundance in high-density energy electrochemical storage devices. The lead in depleted accumulators is currently destined mostly for recycle and reuse in similar accumulators. In this study the suggested reuse of such lead sources in lead perovskite solar cells opens up interesting future possibilities for more experimentation and development. To the best of our knowledge we present for the first time an investigation on the synthesized PbI_2 via optical, structural, morphological characterizations and purity assessments of for solar cell applications.

4.3 Results and Discussion

4.3.1 Structural analysis

To understand the formation and evolution of PbI_2 phase and crystallization, XRD measurements of the PbI_2 powders were carried out. Figure 4.2 shows

the XRD patterns of PbI_2 for four different washing processes labeled (PbI_2-1 to PbI_2-4). The 2θ diffraction peaks were then observed at 22.45^o, 25.94^o,

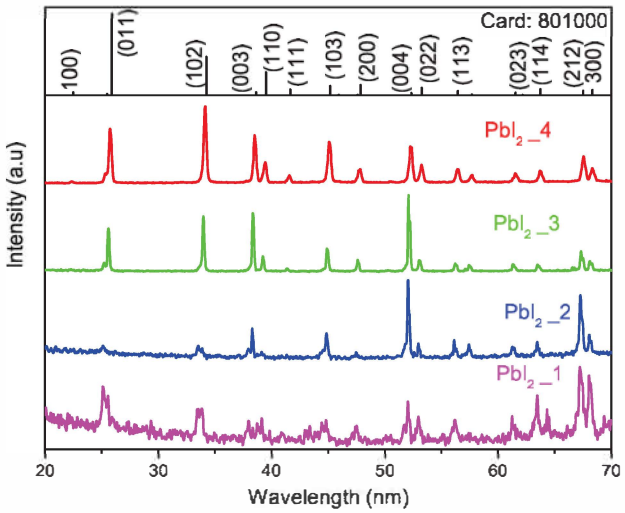

Figure 4.2: XRD patterns of PbI_2 from different washing and synthesis methods

34.18^o, 38.56^o, 39.73^o, 41.72^o, 45.31^o, 47.85^o, 52.41^o, 53.28^o, 56.53^o, 61.61^o, 63.71^o, 67.65^o, and 68.44^o. These peaks respectively correspond exactly to crystal plane reflections (100), (011), (102), (003), (110), (111), (103), (200), (022), (113), (023), (114), (212) and (300). These reflections correspond to the standard card (JCPDS:80-1000) of hexagonal PbI_2 structure. This suggests the absence of foreign impurities in the powder (PbI_2). Therefore, this implies that the method used is suitable for yielding high quality PbI_2 nanoparticles. The evolution of Figure 4.2 further suggests that with more sample washing and re-heating the diffraction peaks become narrower with higher intensity. Further evidence of this can be seen in Figure 4.3, which is a detailing of the XRD pattern at the (102) reflection. Figure 4.4 XRD shows the presence of PbI_2 nanoparticles synthesized using the cathode. The observations suggest pure and highly crystalline PbI_2 structure is attainable by washing. The mean crystallite particle size was estimated using the Debye-Scherrer equation [11,

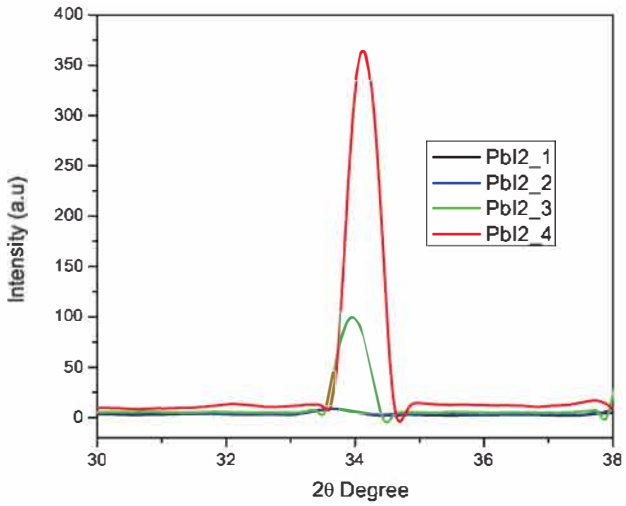

Figure 4.3: Detailed XRD pattern showing the effect of washing and synthesis method on PbI_2 intensity

12].

$$D = \frac{k\lambda}{\beta \cos\theta} \tag{4.3.1}$$

where D is the size of the crystallites, β is the full-width at half-maximum (FWHM) of a diffraction line located at angle θ, λ is the x-ray wavelength and k=0.9 is the Scherrer constant, which depends on the peak breadth, crystallite shape, and crystallite size distribution. Five prominent peaks for all samples were chosen to estimate the average crystallite size of PbI_2 nanostructures by the least squares method. The estimated crystallite sizes are 13.70, 11.59, 12.49, and 14.32 nm for samples heated in ascending order. For more accurate results, instrumental effect (broadening) and internal strain within the samples were taken into account by correcting the peaks. It is evident that the crystallite sizes increase with washing intensity, thus confirming the literature observation that the growth and synthesis method is significant in the fabrication of PbI_2 nanostructures [13]. To further investigate all electrodes as possible sources of lead iodide the acetic acid method was used. Figure 4.5 is the XRD pattern of the cathode sourced PbO_2 nanoparticles. The figure matches the standard card: (JCPDS:73-0851) with few impurity peaks, which are

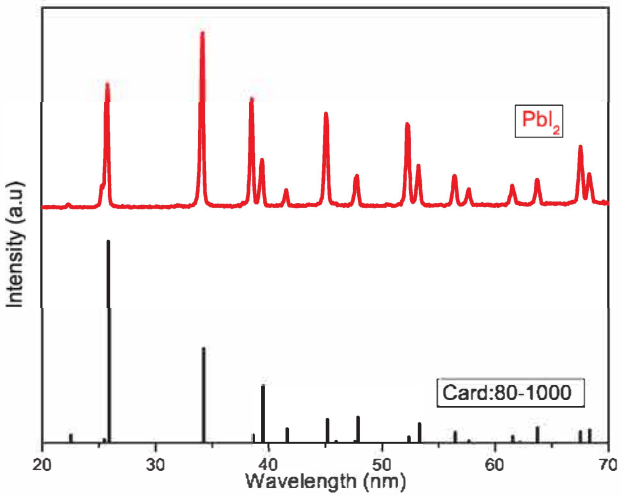

Figure 4.4: XRD patterns of PbI_2 from cathode

attributable to unwashed remnant gel sulphuric acid. Figure 4.6 is the XRD pattern indicates the presence of PbO nanoparticles after annealing PbO_2 particles for 5 hrs.

4.3.2 Morphology and chemical composition

The morphology, chemical composition and elemental distribution of the samples were investigated by scanning electron microscopy. Figures 4.7(a)-(e) indicate that for both anode and cathode precursors the PbI_2 particle morphology is approximately spherical with the varying diameters. However, for the anode precursor the resultant particles increase in size with increased washing, as shown in Figures 4.7(a)-(d). From 4.7(a) it is clear that the powder consisted of various particles sizes and morphologies making exact size determination more difficult, although average particle size was estimated at 691.60 nm. It is evident from the improved contrast that SEM images in Figures 4.7(b)-(d) illustrated that some nanoparticles agglomeration occurred to form larger clusters with diameters averaging 1.87, 3.16 and 3.40 μm respectively. Figure 4.7(e) shows nanoparticles synthesized from the cathode precursor material,

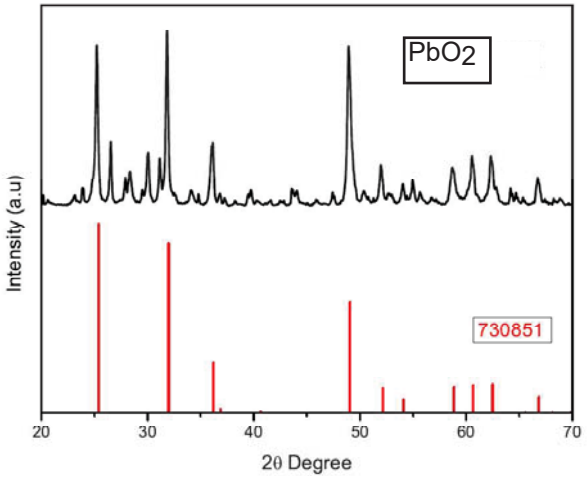

Figure 4.5: XRD patterns of PbO_2 extracted from cathode

with average particle size at approximately 1.53 μm. Both methods gave similar particle arrangement and morphology.

Figure 4.8 shows the SEM elemental mapping measurements of the PbI_2 particles from both anode and cathode starting materials. The figure data suggest the absence of impurities except carbon attributable to post heating, and potassium, which can be attributed to un-reacted precursors. Figure 4.9 shows the traditional EDS measurements on the PbI_2 products for both anode and cathode starting materials. The results are in agreement with those from the SEM elemental mapping measurements. However, in spite of the prominent Pb, I, K and C peaks in the EDS spectrum, the weight percentage of Pb, and I elements obtained from EDS is nearly stoichiometric. This is a good indication that both source materials are good starting materials for PbI_2 nanoparticles and may be suitable for further exploration of lead iodide perovskite solar cells.

4.3.3 Optical properties

PL measurements on anode-sourced PbI_2 nanostructures were carried out using 200 nm wavelength excitation. Figure 4.10 shows the spectra obtained

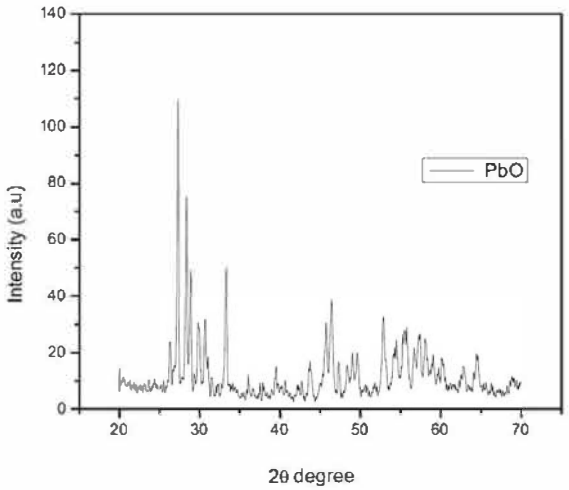

Figure 4.6: XRD patterns of PbO after annealing at 600 ^{o}C

by monitoring PbI_2 emissions on the blue emission band, between 440 to 500 nm. One broad peak was observed centered at 457 nm which scales linearly without any sign of saturation. This broadness is attributed to the known free excitons [14, 8].

The maximum emission intensity for PbI_2 nano-structure was obtained with increased washing. This result implies that the intensity of the near-band-edge emission depends on the extent of PbI_2 powder crystallinity, with increased crystallinity leading to enhanced optical properties. The observable bands are directly related to higher-order crystallinity, which is consistent with the XRD measurements. Emission band red-shift is observed in Figure 4.10. This could be due to increase in the particle size of PbI_2 during particle growth process. This observation is further supported by the XRD results. The broadening of PL emission spectra is thought to be related to the increase in material crystallinity by the removal of impurities, as suggested by the SEM micrographs. Figure 4.11 shows the PL spectrum of cathode sourced PbI_2 nanoparticles under 200 nm wavelength excitation, with a similar broad emission peak at around 457 nm.

The optical absorption of direct band gap (E_{em}) of PbI_2 nanoparticles

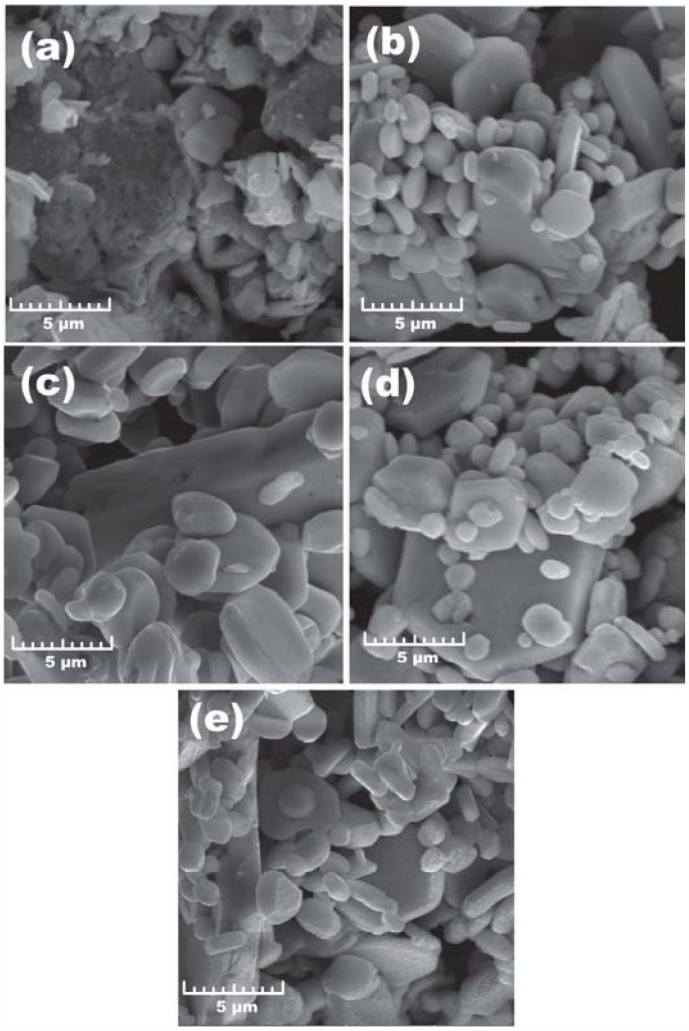

Figure 4.7: SEM micrographs of anode (a)-(d) and cathode (e) PbI_2 ($\times$10k magnification).

was estimated using the emission energy equation

$$E_{(em)} = \frac{hc}{\lambda} \tag{4.3.2}$$

where h is Planck's constant, c is the speed of light and λ is a cut-off wavelength in nanometers. The optical band gap was determined by extrapolating a straight line from the peak height shown in Figure 4.10. The average estimated band gaps of both anode and cathode sourced PbI_2 nanoparticles were 2.73 eV and 2.69 eV respectively ($\pm$ 0.6 eV). The obtained band gap is consistent with the one reported in the literature [7, 24]. The estimated band gap shifts towards higher energy compared to the 2.5 eV direct band gap of bulk PbI_2.

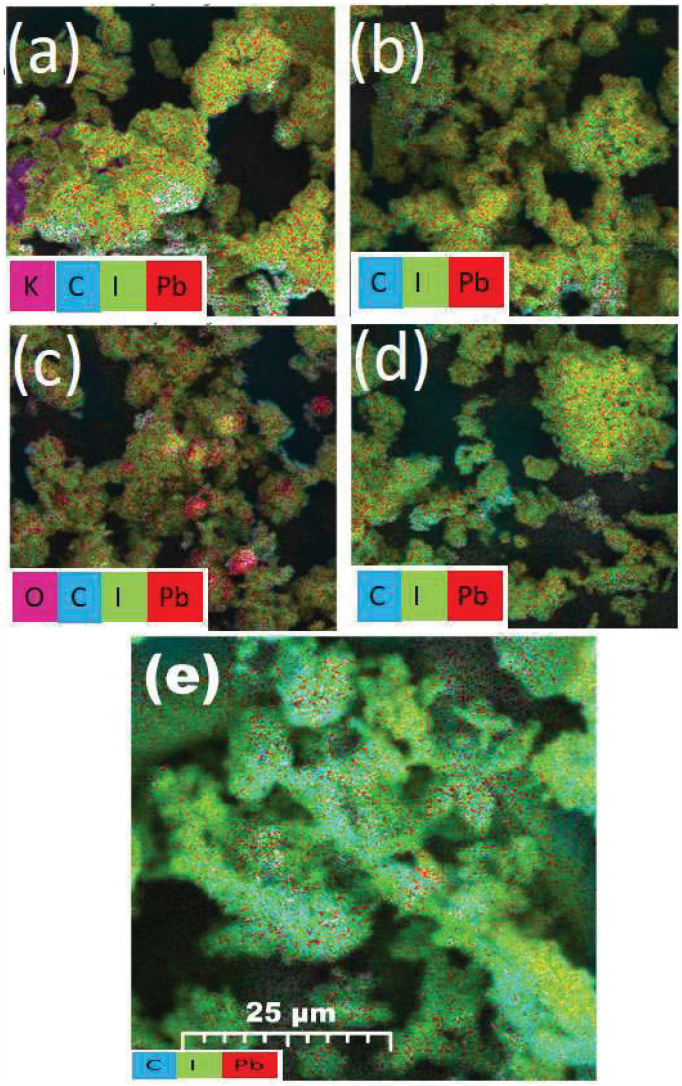

Figure 4.8: SEM images of PbI_2 elemental mapping from anode (a)-(d) and cathode (e).

The crystallite particles sizes were estimated from XRD using Debye-Scherrer equation found to be in the range of 11.5 to 14.3 nm, consistent with the PL measurements. The obtained PL maximum at E_g=2.713 eV is blue shifted relative to PbI_2 bulk energy gap. This indicates that the obtained structure consists of PbI_2 nanoparticles, with average crystallite size of 13 nm. However, by confining PbI_2 sizes within extensive Linde Type A zeolite matrices Tang et al [18] showed that the dimensions of PbI_2 crystallites effectively places them in the low quantum confinement regime, where their sizes are larger than the

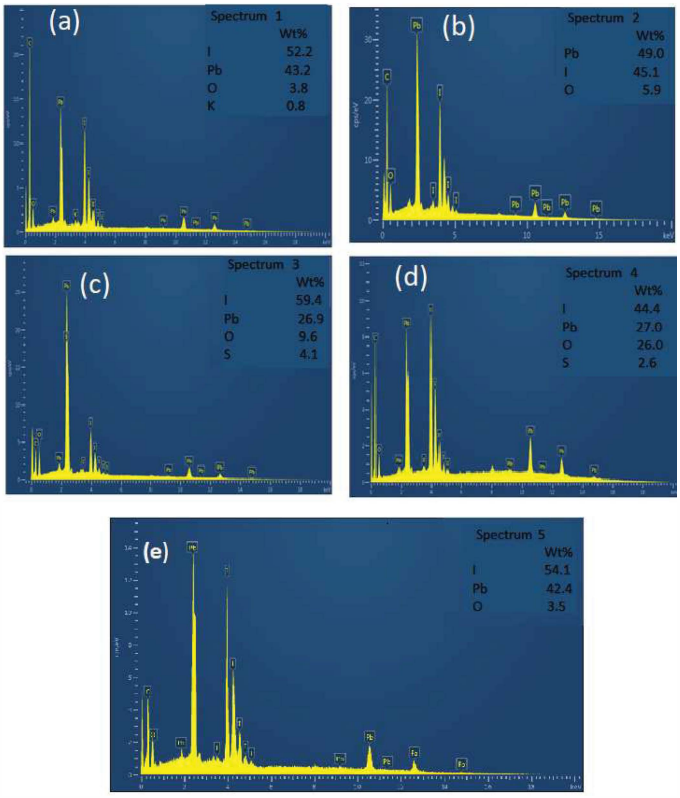

Figure 4.9: EDS of PbI_2 particles.

effective Bohr radius of the exciton (~1.9 nm) [19]. Therefore, the variations of the PL maximum could be attributed to the quantum size effect rather than to particle size variations or preparation method.

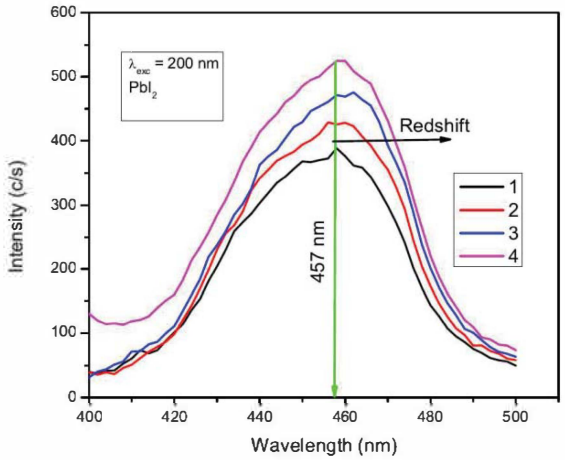

Figure 4.10: PL emission spectra of anode-sourced PbI_2 (λ_{exc}=200 nm).

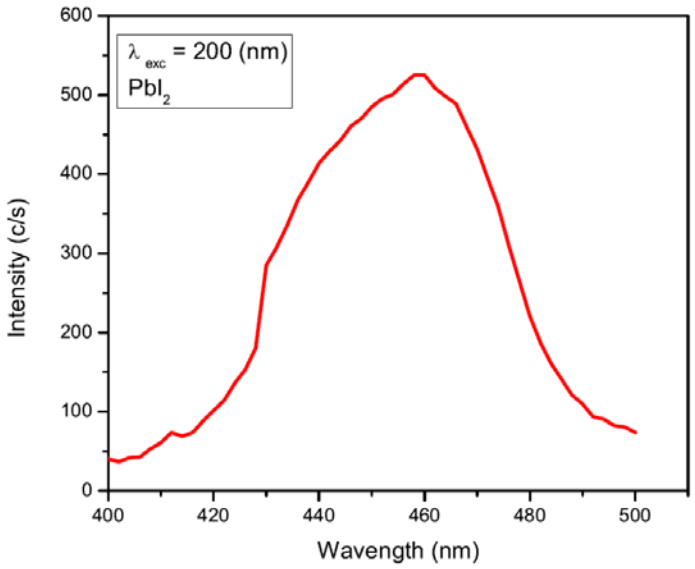

Figure 4.11: PL emission spectra of cathode-sourced PbI2 (λ_{exc}=200 nm).

4.4 Conclusions

For the first time, highly pure and crystalline lead (II) iodide nanopowders were successfully prepared using two separate approaches on the anode and the cathode materials obtained from a depleted SLAG accumulator. The powders exhibited good thermal stability, which is needed for the final solar cell to be stable in use over varied environmental temperatures. The average crystallite size was found to be 13.03-µm. SEM micrograph revealed grain-like surface morphologies with grain sizes ranging between 1.5 and 3.5 nm. Spectral PL emissions were observed in blue region from 400 to 500 nm, attributed to the well-known excitonic band. The band gap was found to be in the range of 2.69 and 2.75 eV for both methods. The present study therefore suggests effective routes and methods for the low-cost production of high-quality lead (II) iodide nanopowders that have potential applications in lead iodide perovskite solar cells. The cost implications are attractive considering the abundance of discarded lead-acid accumulators.

References

[1] Zheng, Z., Liu, A., Wang, S., Li, Z., Lau, W.M., Zhang, L. 2005. In situ growth of epitaxial lead iodide films composed of hexagonal single crystals, *Journal of Materials Chemistry*, 15: 4555–4559

[2] Dmitriev, Y., Bennett, P.R., Cirignano, L.J., Klugerman, M., Shah, K.S. 2008. Physical modeling of the electrical properties of PbI_2 films, *Nuclear Instruments and Methods in Physics Research Section A: Accelerators, Spectrometers, Detectors and Associated Equipment*, 592(3):334–345

[3] Condeles, J.F., Ando, R.A., Mulato, M. 2008. Optical and structural properties of PbI_2 thin films, *Journal of Material Science*, 43: 525–529

[4] Shkir, M., Abbas, H., Siddhartha, Khan, Z.R. 2012. Effect of thickness on the structural, optical and electrical properties of thermally evaporated PbI_2 thin films, *Journal of Physics and Chemistry of Solids*, 73: 1309–1313

[5] Dos Santos, E.M.S., Pereira, L.S., Dements, G.J.F. 2011. Quantum Confinement in PbI_2 Nanodisks Prepared with Cucurbit[7]uril, *Journal of the Chemical Society*, 22(8): 1595–1600

[6] Preda, V., Mihut, L., Baltog, I., Velula, T., Teodorescu, V. 2006. Optical properties of low-dimensional PbI_2 particles embedded in polyacrylamide matrix, *Journal of Optoelectronics and Advanced Materials*, 8(3):909–913

[7] Kasi, G.P., Dollahon, N.R., Ahmadi, T.S. 2007. Fabrication and characterization of solid PbI_2 nanocrystals, *Journal of Physics D: Applied Physics*, 40(6):1778

[8] Zhu, X.H., Zhao, B.J., Zhu, S.F., Jin, Y.R., He, Z.Y., Zhang, J.J., Huang, Y. 2006. Synthesis and characterization of PbI_2 polycrystals, *Crystal Research and Technology*, 41(3):239–242

[9] Ma, D., Zhang, W., Zhang, M., Xi, G., Qiam, Y. 2005. A facile hydrothermal synthesis route to singlecrystalline lead iodide nanobelts and nanobelt bundles, *Journal of Nanoscience and Nanotechnology*, 5(5):810–813

[10] Schiebera,M., Zamoshchik, N., Khakhana, O., Zucka, A. 2008. Structural changes during vapor-phase deposition of polycrystalline-PbI_2 films, *Journal of Crystal Growth*, 310(13):3168–3173

[11] Alexander, L., Klug, H.A. 1950. Determination of Crystallite Size with the x-ray Spectrometer, *Journal of Applied Physics* 21: 137–142

[12] Molefe, F.V., Koao, L.F., Dejene, B,F., Swart, H.C. 2015. Phase formation of hexagonal wurtzite ZnO through decomposition of $Zn(OH)_2$ at various growth temperatures using CBD method, *Optical Materials*, 46:292–298

[13] Zheng, Z., Wang, S., Li, D., Liu, A., Huang, B., Zhao, H., Zhang, L. 2007. Morphology-controlled synthesis of lead iodine compounds from lead foils and iodine, *Journal of Crystal Growth*, 308(2):398–405

[14] Derenzo, S.E., Weber, M.J., Klintenberg, M.K. 2002. Temperature dependence of the fast, near-band-edge scintillation from CuI, HgI_2, PbI_2, ZnO:Ga and CdS:In, *Nuclear Instruments and Methods in Physics Research A*, 486:214–219

[15] Zhang, J., Song, T., Zhang, Z., Ding, K., Huang, F., Sun, B. 2015. Layered ultrathin PbI_2 single crystals for high sensitivity flexible photodetectors, *Journal of Material Chemistry C*, 3:4402

[16] Zhu, G., Hojamberdiev, M., Liua, P., Peng, J., Zhou, J. 2011. The effects of synthesis parameters on the formation of PbI_2 particles under DTAB-assisted hydrothermal process, *Materials Chemistry and Physics*, 131:64–71

[17] Koutselas, I., Dimos, K., Bourlinos, A., Gournis, D., Avgeropoulos, A., Agathopoulos, S., Karakassides, M.A. 2008. Synthesis and characterization of PbI_2 semiconductor quantum wires within layered solids, *Journal of Optoectronics and Advanced Materials*, 10(1): 58–65

[18] Tang, Z.K., Nozue, Y., Goto, T., 1992. Quantum Size Effect on the Excited State of HgI_2, PbI_2 and BiI_3 Clusters and Molecules in Zeolite LTA, *Journal of the Physical Society of Japan*, 61(8):2943–2950

[19] Nagamune, Y., Tekeyama, S., Miura, N., 1989. Magnetoabsorption spectra of band-edge excitons in 2H-PbI_2 at high magnetic fields up to 40 T, *Physical review B*, 40:8099

Chapter 5

Phase transformations of PbI_2 nanoparticles synthesized from lead-acid accumulator anodes

5.1 Overview

In this chapter we investigate the effects of annealing time and post-melting temperature of a rare 6R polytype form of PbI_2 synthesized from lead-acid accumulator anode. The XRD characteristics show a phase transformation when annealing time increased from 0.5 - 5 hrs. The nanoparticle grain size and inter-planar distance appeared to be independent of annealing time. PL measurements show three broad peaks in a range of 400 nm to 700 nm that are attributed to excitonic, donor-acceptor pair and luminescence bands from the deep levels. In addition, the effect of annealing time on emission and high temperature phase transformation are discussed.

5.2 Introduction

PbI_2 consists of high atomic number elements (Z_{Pb}=82 and Z_I=53) and exhibits high photon stopping power. PbI_2 melts congruently at 408 ^{o}C, with no destructive phase transitions between room temperature and melting point [9, 10]. It also has a low vapor pressure and does not volatilize easily at room temperature [11]. However, obtaining high quality PbI_2 crystals remains

problematic due to factors related to crystal growth and temperature stability. At first, there are concerns about its degradation at sustained temperatures up to 130 ^{o}C. Secondly, decomposition of the PbI_2 melt during the crystal growth process can lead to deposition of segregated Pb and evaporation of I_2, which may change the stoichiometry. Thirdly, the intra-layer chemical bonding between the Pb layer and the adjacent I layers in an individual I-Pb-I package is strongly ionic and/or covalent, whereas the interlayer bonding between the individual packages is due to much weaker van der Waals iodine-iodine atom interactions. This leads to a difficult to handle, flaky PbI_2 crystal that readily cleaves normal to the *c*-axis. Good surfaces parallel to the *c*-axis are then difficult to obtain and structural faults and dislocations are common [16]. Various reported synthesis methods attempt to address these issues. For instance, the low-temperature colloidal synthesis method [12], reverse micelles method [13], vapor-transporting method [14], vapor deposition [3] and hydrothermal techniques [15]. Almost all literature sources surveyed conducted PbI_2 investigations at ambient temperatures. Therefore no destructive phase transformations below the melting temperature are reported.

The present chapter reports on an aspect of a wider project to fabricate low-cost lead-perovskite solar cells from recycled lead-acid batteries [7]. The aim of the present investigation is to subject PbI_2 to annealing temperatures higher than the melting point in order to observe the possible structural changes to the compound, particularly with regards to any changes in its stoichiometry. Vapor-phase synthesis of stoichiometrically diverse PbI_2 is possible because the compound can also be grown from both melt [6]. The various stoichiometries may give interesting future directions in attempts to enhance solar cell performance. The source of PbI_2 in the present work is by secondary synthesis using lead metal from the anode of discarded lead-acid accumulator as precursor. To the best of our knowledge we present for the first time the formation of 6R polytype phase transformation in lead iodide crystals.

5.3 Results and Discussion

5.3.1 Structural analyses

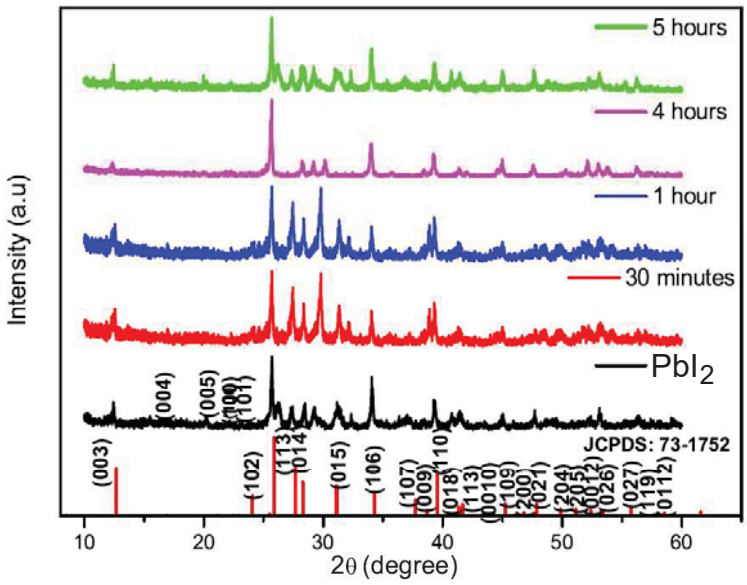

Figure 5.1: XRD patterns of (a) PbI_2 at different annealing times

The effects of temperature on the crystallinity and phase transformation of the annealed PbI_2 powders XRD were investigated using XRD. Figure 5.1 shows the reflections for annealing times of 0.5 hr to 5 hrs. All the reflections correspond to the JCPDS:873-1752 standard card for hexagonal PbI_2. After post-melting treatment, additional intense peaks are observed at 16.93^o, 21.20^o, 22.51^o and 22.91^o, corresponding to the (004), (005), (100) and (101) planes. The lattice parameters calculated from these additional peaks are a=0.4557 nm and c=0.6979 nm. This indicates the presence of pure, high-temperature stable, hexagonal phase 6R polytype PbI_2 [8]. This phase, which is rarely attained in the literature, is considered to be important in current attempts to improve perovskite solar cells because of its better carrier mobility [9]. In Figure 5.2, the (106) peak position shifted slightly towards smaller angle (2θ) with increasing annealing time. This implies phase transformations associated with an increasing parameter c due to weakening of the I-I bond

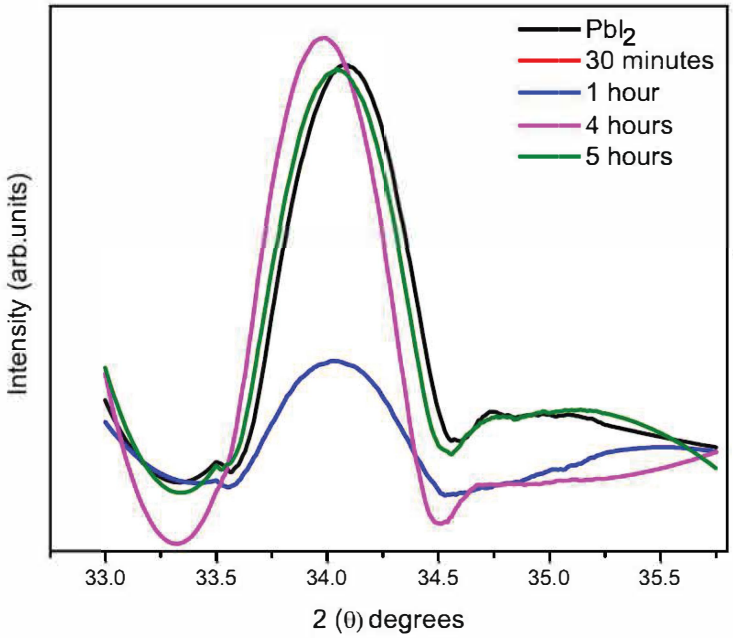

Figure 5.2: A shift detail of the (106) peak

in loosely coupled I-Pb-I packages [11, 17]. Post-melting annealing can lead to the formation of mechanical defects such as dislocation and slip planes. These effects are actively being studied because they limit room temperature stability and commercialization of PbI_2 nanoparticle-based perovskite solar cells [18, 19]. For these purposes, it is important to improve growth techniques for pure 6R polytype crystals in light of their high electron/hole mobilities. It is reported that the most room- and high temperature-stable polytypes are 2H and 12R [20, 21].

The lattice parameters presented in Table 5.1 for reflection (hkl) are calculated using [22]:

$$\frac{1}{d_{hkl}^2} = \frac{4}{3} + \frac{h^2 + h^2 + hk}{a^2} + \frac{l^2}{c^2} \tag{5.3.1}$$

where

$$c = \frac{\lambda}{\sqrt{3}\sin\theta} \quad \text{and} \quad a = \frac{\lambda}{\sin\theta}. \tag{5.3.2}$$

The planes (013), (014) and (106) give a= 4.558 Å and c=6.780 Å, which correspond to the standard card JCPDS: 873-1752. Nanoparticle grain sizes

Table 5.1: Lattice parameters as a function of annealing temperature at 500 ^{o}C

Time (hr)	2θ	d_{hkl} (Å)	Grain size (Å)	Plane	a, c (Å)
0.5	25.74	3.46	126.53	(013)	$a = 4.00$
	28.31	3.15	129.01	(014)	
	34.05	2.63	111.35	(106)	$c = 6.92$
Sample2 (PbI_2)	25.61	3.48	107.75	(013)	$a = 4.02$
	28.25	3.60	97.73	(014)	
	33.98	2.64	114.67	(106)	$c = 6.96$
5.0	25.63	3.48	97.12	(013)	$a = 4.01$
	28.34	3.15	195.73	(014)	
	34.04	2.63	104.01	(106)	$c = 6.95$
4.0	25.63	3.48	77.36	(013)	$a = 4.01$
	28.34	3.15	97.65	(014)	
	34.04	2.63	105.28	(106)	$c = 6.95$
1.0	25.74	3.55	125.35	(013)	$a = 3.99$
	28.38	3.24	133.45	(014)	
	34.08	2.75	104.00	(106)	$c = 6.95$

were estimated using the Debye-Scherrer equation

$$D = \frac{K\lambda}{\beta \cos\theta}, \tag{5.3.3}$$

where D is crystallite size, β is the full-width at half-maximum at θ reflection angle. The x-ray wavelength is λ. The Scherrer constant, which depends on peak breadth, crystallite shape and size distribution, is K=0.94. The lattice spacing (d_{hkl}) was calculated using Braggs law:

$$2d_{hkl} \sin\theta = n\lambda, \tag{5.3.4}$$

where θ is the Bragg angle. Annealing conditions, particularly the temperature and time, play a significant role in improving the crystallinity of the material by increasing the material grain size [23]. In this study, the annealing time did not significantly affect the observed grain size and inter-planar distance. The preferred crystalline orientation is known, however, to

depend on crystallite size in PbI_2 thin films [4].

5.3.2 Optical properties

Figure 5.3 shows both excitation and emission spectra of ununnealed PbI_2 nanoparticles. The excitation wavelength of 221 nm was then used to excite PbI_2 nanopowders annealed at different annealing times. Figure 5.4 shows the

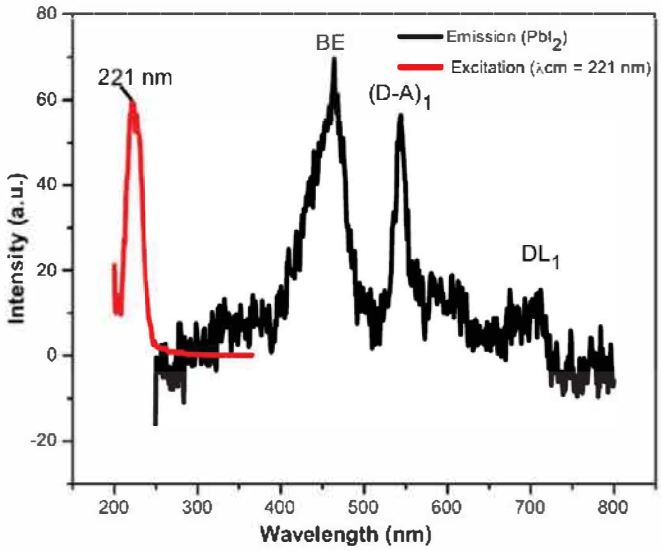

Figure 5.3: PL excitation and emission spectra of unheated PbI_2

emission spectra of PbI_2 nanoparticles, with three broad peaks between 400 nm and 700 nm. This PL spectrum consists of a series of excitonic lines around 2.5 eV (495 nm) and a broad band associated with a shallow donor level around 2.43 eV (510 nm). The latter is due to donor-acceptor pair recombination associated with lattice imperfections or impurities. Luminescence bands from deep levels are observed at 600 nm. They appear to depend strongly on annealing time. Phonon replicas of both bands could be resolved on good quality samples [9]. It is observed that around 2.4 eV the band becomes narrow with increasing annealing time. This indicates improved PbI_2 nanoparticle purity with annealing and higher crystallinity, in agreement with the XRD measurements in Figure 5.1. Red-shift in the emission bands is also observed in

both Figure 5.3 and Figure 5.4 which is further evidence of phase transformations.

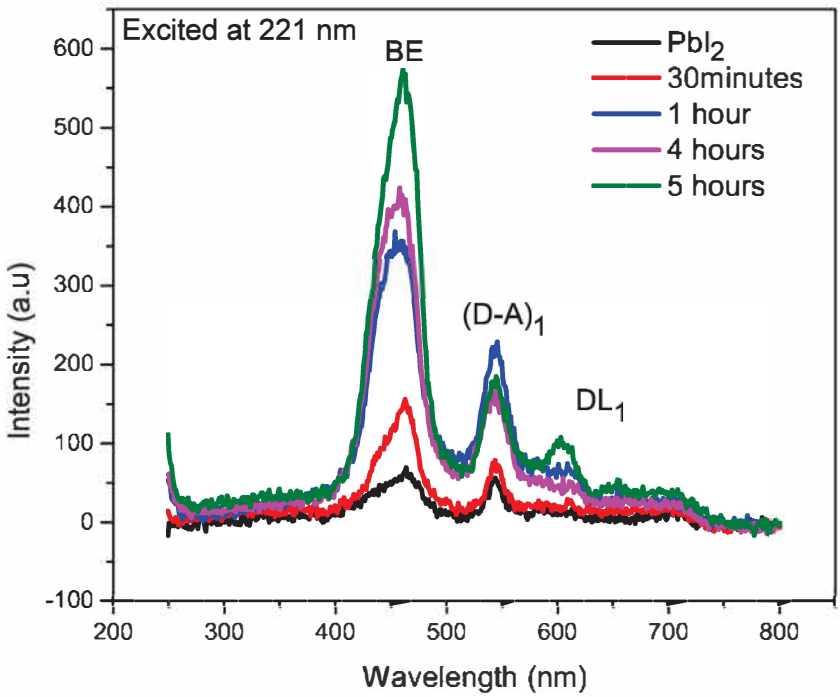

Figure 5.4: PL analysis of PbI_2 nanoparticles annealed at different annealing time

The estimated PbI_2 nanoparticle optical band gaps (E_g) respectively average 2.76 eV (excitonic band), 2.26 eV (donor-acceptor pair bands) and 2.07 eV (luminescence bands). These estimates are in agreement with values in the literature [7, 24].

5.3.3 Thermodynamic stability analysis

The quality of perovskite films depends strongly on conversion and formation of high-quality perovskite grains, which typically involve heat treatment. Thermal analysis provides valuable insights into the thermal stability of the final product. Direct TGA and DSC measurements were conducted under an inert, regulated flow-rate N_2 atmosphere. Figure 5.5 shows TGA measurements on the PbI_2

nanoparticles. Unheated and 0.5 hr heated TGA curves are similar with respect to weight loss as only one degradation curve is observed. Both curves

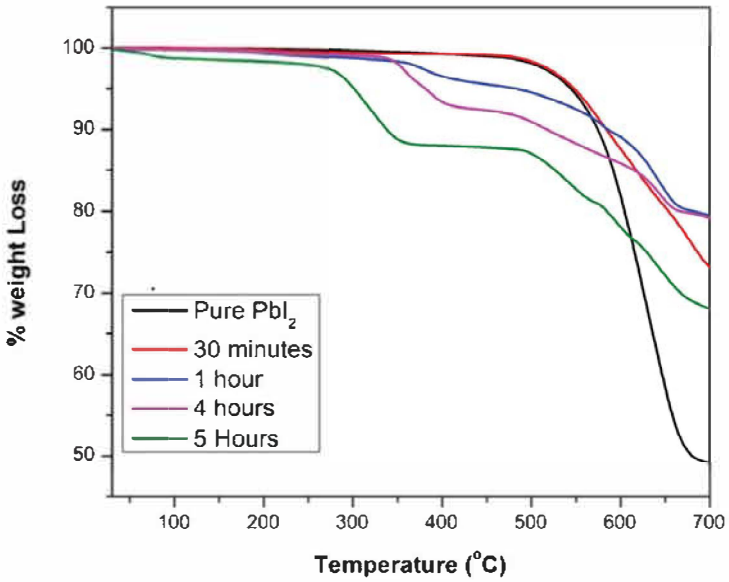

Figure 5.5: TGA curves of thermal decomposition of PbI_2 nanoparticles at different annealing time

show no weight loss up to 480 ^{0}C, suggesting that the material is thermally stable up to this temperature. No coordinated water molecules or any water of crystallization in the PbI_2 nanoparticles were observed. Slow decomposition is observed between 490 ^{0}C to 580 ^{0}C with a sudden loss in weight occurring at 600 ^{0}C. The total weight loss are 26.8% (unheated) and 50.3% (0.5 hr heated). The mass loss between 550 ^{0}C and 600 ^{0}C for both solutions agrees with the thermal decomposition of the inorganic PbI_2 part of perovskite reported in the literature [4, 25]. In contrast, the samples heated through 1.0, 4.0 and 5.0 hrs undergo two degrading steps with weight loss observed at around 300 ^{0}C and 500 ^{0}C respectively. The broad weight loss profile implies lower thermal stability at higher temperatures through distortion of Pb-I-Pb bonds. This is supported by the shift in onset decomposition temperature towards lower temperatures, in direct support of XRD results. The thermal stability of PbI_2 nanoparticle phases after annealing at different times was studied using DSC.

Figures 5.6 (a)-(c) show a single endothermic peak that could be due to the PbI_2 phase transformation reported in the literature [4]. Longer annealing times appear to shift the peak towards higher temperature. This could be due to surface crystallization or internal stress relaxation in the material which lead to endothermic rearrangement of the crystal lattice [25, 26]. Figures 5.6 (d) and (e) show no endothermic peaks, suggesting that latent heat is neither absorbed nor given off after heating, which would have indicated melting or crystallization. No change in the PbI_2 heat capacity was observed. Further studies are needed to better understand the temperature-time characteristics of PbI_2 crystals.

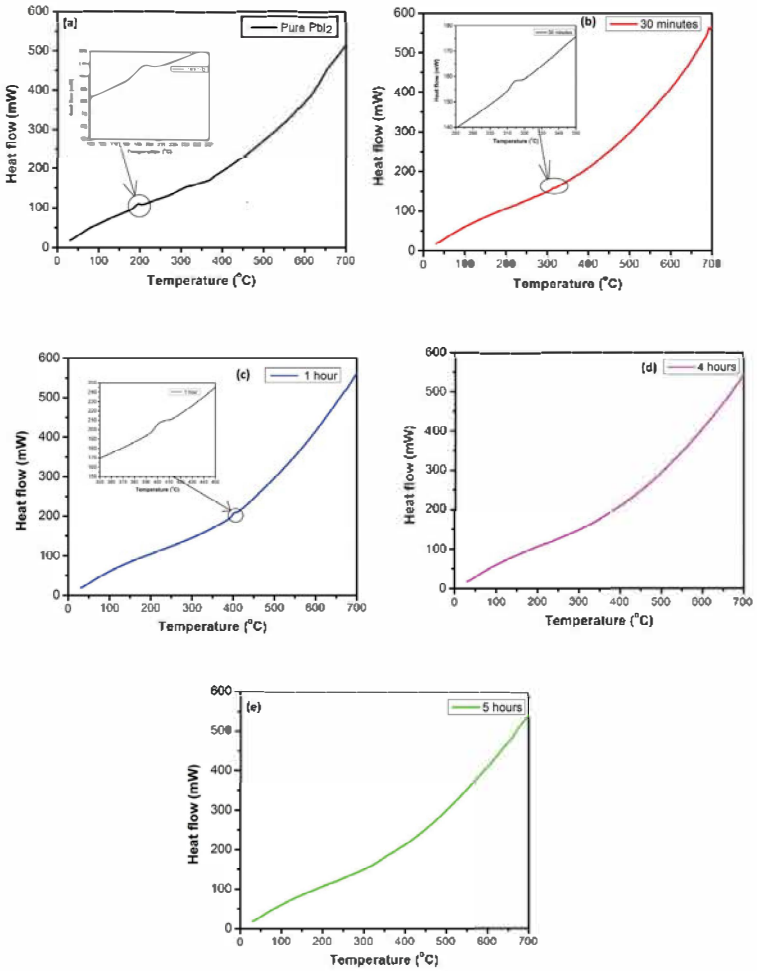

Figure 5.6: DSC scans of PbI_2 nanoparticles versus annealing time (a) unheated (b) 30 mins (c) 1 hr (d) 4 hrs and (d) 5 hrs

5.3.4 FTIR analysis

Figure 5.7 shows the FTIR spectrum of PbI_2 nanoparticles. The data suggests that no organic components are present in the synthesized PbI_2 nanoparticles. The spectrum bands are attributable only to vibrational modes of inorganic clusters. The bands around 1400 to 1650 /cm can be explained in terms of different vibrational modes of the O-H group in absorbed water molecules [27]. These modes disappear with increased annealing time due to the removal of the water molecules. The existence of strong interactions between Pb and

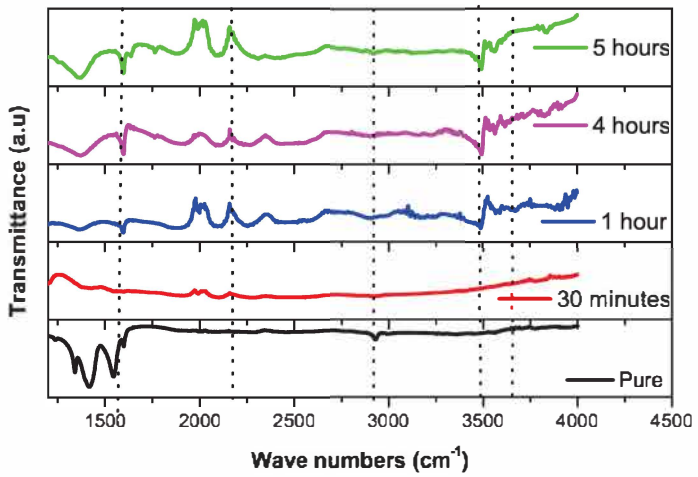

Figure 5.7: FTIR spectra of PbI_2 nanoparticles versus annealing time (a) un-heated (b) 30 mins (c) 1 hr (d) 4 hrs and (d) 5 hrs

I molecules is confirmed by the FTIR spectrum. The peaks around 3412 and 3383 /cm are due to asymmetric and symmetric stretching vibrations of the inorganic Pb-I clusters [28]. The stretching vibrations increase with the annealing time and shift slightly to lower stretching wave numbers, further supporting high temperature phase transformation.

5.4 Conclusions

In conclusion, we have reported on studies of post-melting point annealing temperature and time on the crystallinity, phase transformation and thermal stability of PbI_2 nanoparticles synthesized using anode lead from a discarded lead-acid accumulator as the starting point. The reported synthesis route is based on recrystallization during cooling. Measurements confirmed that the high-purity synthesized product consisted of the rare 6R polytype form of PbI_2. This polytype is thought to hold considerable promise in perovskite photovoltaic applications because of its higher electron/hole mobility. Measurements using XRD, PL, TGA, DSC and FTIR techniques confirm that the as-synthesized hexagonal PbI_2 exhibits increased emission intensity with increased annealing time. Higher temperature phase transformations were confirmed by the presence of a single endothermic peak in DSC and the slight shift to lower wave numbers in FTIR, attributable to stretching vibrations.

References

[1] Condeles, J.F., Ando, R.A., Mulato, M. 2008. Optical and structural properties of PbI_2 thin films, *Journal of Material Science*, 43: 525–529

[2] Mousa, A.M., Al-rubaie, N.J. 2009. The influence of depostion conditions on structural properties of PbI_2, *Texture, Stress, and Microstructure*, Volume 2009, Article ID 494537

[3] Dmitriev, Y., Bennett, P.R., Cirignano, L.J., Klugerman, M., Shah, K.S. 2008. Physical modeling of the electrical properties of PbI_2 films, *Nuclear Instruments and Methods in Physics Research Section A: Accelerators, Spectrometers, Detectors and Associated Equipment*, 592(3):334–345

[4] Bhavsar, D.S. 2011. Structural studies of vacuum evaporated lead iodide thin films, *Advances in Applied Science Research*, 2 (2): 407–413

[5] Malevu, T.D., Ocaya, R.O., Tshabalala, K.G., Fernandez, C. 2016. Synthesis and characterization of high quality PbI_2 nanopowders from depleted SLA accumulator anode and cathodes, *Applied Physics A: Materials Science and Processing*, 122(7): 630

[6] Hassan, M.A., Jafar, M.M., Matuchova, M., Bulos, B.N. 2010. An experimental evidence of some lead lodide polytypes compatible with the dielectric function model, *Journal of Applied Sciences*, 10(24): 3367–3373

[7] Zhu, G., Hojamberdiev, M., Liua, P., Peng, J., Zhou, J. 2011. The effects of synthesis parameters on the formation of PbI_2 particles under

DTAB-assisted hydrothermal process, *Materials Chemistry and Physics*, 131:64–71

[8] Zhang, J., Song, T., Zhang, Z., Ding, K., Huang, F., Sun, B. 2015. Layered ultrathin PbI_2 single crystals for high sensitivity flexible photodetectors, *Journal of Material Chemistry C*, 17(3):4402–4406

[9] Matuchova, M., Zdansky, K., Zavadil, J., Maixner, J., Alexiev, D., Prochazkova, D. 2006. Study of lead iodide semiconductor crystals doped with silver, *Materials Science in Semiconductor Processing*, 9:394–398

[10] Zhao, X., Jin, Y., Zhu, X. 2010. Polycrystal synthesis and single crystal growth of PbI_2, *Applied Mechanics and Materials*, 26(28):720–723

[11] Chaudhary, S.K., Kaur, H. 2011. Impurity induced structural phase transformations in melt grown single crystals of lead iodide, *Crystal Reasearch and Technology*, 46(12):1235–1240

[12] Preda, V., Mihut, L., Baltog, I., Velula, T., Teodorescu, V. 2006. Optical properties of low-dimensional PbI_2 particles embedded in polyacrylamide matrix, *Journal of Optoelectronics and Advanced Materials*, 8(3):909–913

[13] Kasi, G.P., Dollahon, N.R., Ahmadi, T.S. 2007. Fabrication and characterization of solid PbI_2 nanocrystals, *Journal of Physics D: Applied Physics*, 40(6):1778

[14] Zhu, X.H., Zhao, B.J., Zhu, S.F., Jin, Y.R., He, Z.Y., Zhang, J.J., Huang, Y. 2006. Synthesis and characterization of PbI_2 polycrystals, *Crystal Research and Technology*, 41(3):239–242

[15] Ma, D., Zhang, W., Zhang, M., Xi, G., Qiam, Y. 2005. A facile hydrothermal synthesis route to single-crystalline lead iodide nanobelts and nanobelt bundles, *Journal of Nanoscience and Nanotechnology*, 5(5):810–813

[16] Hassan, M.A., Abdul-Gader-Jafar, M.M. 2006. Frequency dependence of loss tangent of thermally annealed undoped lead iodide crystals in the dark, *Nuclear Instruments and Methods in Physics Research A*, 566: 526–535

[17] Salje, E., Palosz, B., Wruck, B. 1987. In situ observation of the polytypic phase transition 2H-12R in PbI_2: investigations of the thermodynamic, structural and dielectric properties, *Journal of Physics C: Solid State Physics*, 20: 4077–4096

[18] Sha, W.E.I., Ren, X., Chen, L., Choy, W.C.H. 2015. The efficiency limit of $CH_3NH_3PbI_3$ perovskite solar cells, *Applied Physics Letters*, 106(22): 221104

[19] Fan, J., Jia, B., Gu, M. 2014. Perovskite-based low-cost and high-efficiency hybrid halide solar cells, *Photonics Research*, 2(5):111–120

[20] Minagawa, T. 1975. Common polytypes of PbI_2 at low and high temperatures and the 2H-12R transformation, *Acta Crystallographica Section A*, A31:823–824

[21] Chaudhary, S.K. 2012. Lead iodide crystal as input material for radiation detectors, *Crystal Structure Theory and Applications*, 1:21–24

[22] Malevu, T.D., Ocaya, R.O. 2014. Effect of annealing temperature on structural, morphology and optical properties of ZnO nano-needles prepared by Zinc-Air Cell system method, *International Journal of Electrochemical Science*, 10:1752–1761

[23] Ibrahim, N.B., Aldbea, F.W., Andullah. 2012. Effects of annealing temperature on structure and magnetic properties of $Tb_xY_{3-x}Fe_5O_{12}$ (x=0.2) thin films, *Journal of Nanomaterials*, 2012:1–6

[24] Koutselas, I., Dimos, K., Bourlinos, A., Gournis, D., Avgeropoulos, A., Agathopoulos, S., Karakassides, M.A. 2008. Synthesis and

characterization of PbI_2 semiconductor quantum wires within layered solids, *Journal of Optoectronics and Advanced Materials*, 10(1):58–65

[25] Dualeh, A., Gao, P., Seol, S., Nazeeruddin, M.K., Gratzel, M. 2014. Thermal behavior of methylammonium lead-trihalide perovskite photovoltaic light harvesters, *Chemistry of Materials*, 26:6160–6164

[26] Baikie, T., Fang, Y., Kadro, J.M., Schreyer, M., Wei, F., Mhaisalkar, S.G., Graetzel, M., White, T.J. 2013. Synthesis and crystal chemistry of the hybrid perovskite $(CH_3NH_3)PbI_3$ for solid-state sensitised solar cell applications, *Journal of Materials Chemistry A*, 1:5628–5641

[27] Zhengwe, J. 1997. Preparation of $PbI_2 \pm PbBr_2 \pm KCl$ ternary heavy-metal halide glasses, *Journal of Material Science Letters*, 16:1656–1657

[28] Kaviyarasu, K., Sajan, D., Selvakumar, M.S., Augustine Thomas S., Prem Anand, D. 2012. A facile hydrothermal route to synthesize novel PbI_2 nanorods, *Journal of Physics and Chemistry of Solids*, 73(11):1396–1400

Chapter 6

Effect of annealing temperature on nanocrystalline TiO_2 for solar cell application

6.1 Overview

This chapter investigates the effect of annealing temperature (AT) on structure, morphology and optical properties of hydrothermally synthesized TiO_2 nanocrystals. Selected-Area Electron Diffraction (SAED) confirmed high quality monocrystals. XRD and Raman spectroscopy indicate only anatase and rutile phases. At high temperature, the (101) and (001) are preferred. PL emission peaks appear at 407, 416 and 493 nm, which can be attributed to photo-excited electron-hole pairs, band-edge excitons and oxygen vacancy defects, respectively. UV-Vis spectroscopy indicates that AT over the $200 - 600\ ^oC$ temperature range causes the band gap to decrease from 3.08 eV to 2.73 eV. Hydrothermal synthesis followed by annealing at $600\ ^oC$ is found to be a good route for high-purity, nanocrystalline anatase-phase TiO_2 with the preferred $\{001\}$ orientation that is thought to enhance solar cell performance.

6.2 Introduction

The current, high interest in the nanostructures of titanium dioxide (TiO_2) is being driven in part by the abundance of low cost processing methods, which

have been shown to impact the resultant morphology, and in part by the fact that a given technology device may perform better when built using a given morphology. The importance of morphology differentiated behavior is only now being understood. For these reasons, TiO_2 nanostructures are finding applications in photocatalytic processes, photovoltaic and photonic and other sensors [1, 2, 4]. Table 6.1 summarizes the basic properties of three basic nanostructural forms of TiO_2. Other forms are known to exist, but are not generally thought to be as important to solar cell device performance.

Table 6.1: Summary of the parameters of the rutile, anatase and brookite structures of TiO_2.

Phase	Space group	Lattice parameter (nm)		Thermal stability (high temp.)	Ref.
		a	c		
Rutile	D_{4h}^{14}–$P4_2/mnm$	0.4584	0.2953	high	[4]
Anatase	D_{4h}^{19}–$I4_1/amd$	0.3733	0.9370	high	[4]
Brookite	D_{2h}^{15}–$Pbca$	0.5456	0.5143	low	[5]

In contrast to the brookite phase, the anatase and rutile phases are more thermally stable and posses higher surface areas, which makes them more suitable for solar cell applications. Several literature studies suggest that the performance of a solar cell profoundly depends on the exposed crystal facet. In single crystals, the {001} anatase facets are the most exposed and are therefore thought to have a good potential for charge transfer. The {001} facets have an estimated surface energy of 0.90 J/m^2, in contrast to 0.44 J/m^2 for the (101). The latter facets have been employed in solar cell devices in various literature accounts. Several synthesis methods have also been reported for the anatase phase with exposed (001) facets. For instance, Bajestani *et al* have grown anatase TiO_2 with exposed (001) facets on n-doped reduced graphene oxide [6]. Dai *et al* evaluated the feasibility of hydrothermal treatment to produce exposed, chemically active (001) facets in the anatase phase [7]. Other workers have demonstrated morphological variants based on (001) facets that

hold promise to enhance solar cell performance, such as nano-tubes [8], nano-sheets [9] and meso-porous spheres [8].

In the present work, we have successfully synthesized TiO_2 nanocrystals that have exposed (001) and (101) facets using a hydrothermal method. The obtained nanocrystals were then annealed at three different temperatures to evaluate the effect of high temperatures on the product quality with respect to nanostructure crystallinity, crystallite size, selected-area electron diffraction pattern, band gap and structural properties.

6.3 Results and discussion

6.3.1 Structural analysis

Figure 6.1 shows the XRD patterns of the TiO_2 powders after annealing at 200 ^{o}C, 400 ^{o}C and 600 ^{o}C. The XRD patterns indicate the presence of nanocrystalline rutile phases, marked (A) and anatase phases, marked (R). Both are in the tetragonal I41/amd space group (No. 141), with a=3.7845 Å, c=9.5143 Å. The peak intensity ratio is approximately 3:1 for anatase relative to rutile phases. Similar results were obtained on a commercial sample of TiO_2 [9, 10]. The brookite phase, which often appears in most nanocrystalline TiO_2 powders prepared using other processes [11, 12], was not observed. Figure 6.2 shows that the crystallinity of both anatase and rutile phases distinctly increases with increasing AT, as indicated by the increase in the full-width-at-half-maximum (FWHM) of the most intense peak (101) peak of the anatase phase. This can be attributed to the change in crystal size [15]. The anatase peak position for (101) plane was used to estimate the crystallite sizes according to the Debye-Scherrer equation:

$$D = \frac{0.9\lambda}{\beta \cos\theta}, \tag{6.3.1}$$

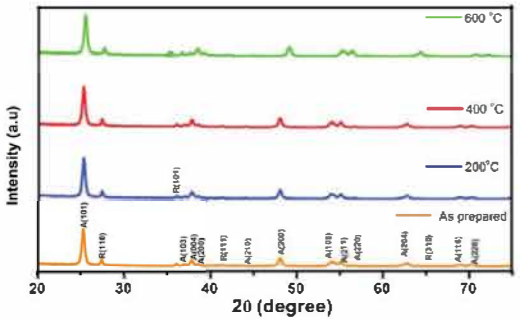

Figure 6.1: XRD patterns of the synthesized nanocrystalline TiO_2 powder at the different AT

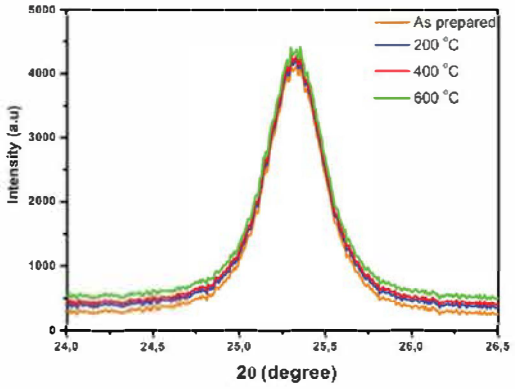

Figure 6.2: Analysis of the most intense peak (101) for anatase phase

where D is crystallite size, β is the full-width at half-maximum (FWHM) at diffraction angle theta, λ is the X-ray wavelength and a Scherrer constant (0.9) that depends on the peak breadth, crystallite shape, and crystallite size distribution. Table 9.1 summarizes the results of application of Equation 9.6.3 to the data. The results show that D averages at 23.05 nm but increases with increasing AT. This indicates that AT plays a vital role in tuning the crystal size. Similar results have been reported on TiO_2 powders by Jaafer *et al* [16]. They argue that annealing induces diffusion-driven phase segregation thereby resulting in a non-homogenous composition and increasing crystal size. It was also important to evaluate the effect of AT on lattice parameters

of the synthesized nanocrystalline TiO_2 powders. The lattice parameters of the annealed TiO_2 powders annealed were calculated using Miller indices [hkl] using Equation 6.3.2.

$$\frac{1}{d^2} = \frac{4}{3} + \left(\frac{h^2 + k^2 + hk}{a^2}\right) + \frac{l^2}{c^2}, \tag{6.3.2}$$

where a and c are the required lattice constants. Equation 6.3.2 becomes:

$$a = \frac{\lambda}{\sqrt{3}\sin\theta}, \quad \text{and} \quad c = \frac{\lambda}{\sin\theta} \tag{6.3.3}$$

under the first order reflection (n=1) on the (101) plane. Table 9.1 summarizes the lattice parameters a and c, which are seen to decrease with increasing AT. This indicates that the anatase lattice is being compressed during the phase transformation due to the gradual build up of stress on the anatase surface [17], causing particle size to increase and/or precipitation of the rutile phase.

Table 6.2: Solar cell parameters as a function of AT.

AT (^oC)	Peak position (2θ)	FWHM	Crystal size (nm)	a (Å)	c (Å)
as-prepared	25.3217	0.3819	22.28	3.798	9.560
200	25.2280	0.3641	22.37	3.791	9.528
400	25.3234	0.3746	22.72	3.785	9.522
600	25.3235	0.3574	22.82	3.777	9.422

Figure 6.3 shows the EDS spectrum of the nanocrystalline TiO_2 powders. The measurements show that there are no impurities from other materials. Although the EDS measurement does not precisely quantify the elementary composition, it suggests that titanium and oxygen atoms are nearly in the expected stoichiometric ratio.

6.3.2 Raman analysis

Raman spectroscopy was used for the structural identification of the annealed samples. It has been reported that anatase TiO_2 has six Raman active modes

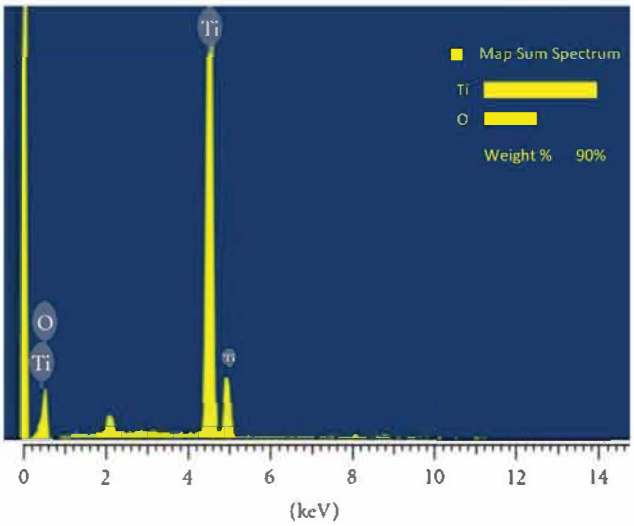

Figure 6.3: EDS spectrum of as-prepared TiO_2 powder.

(A1g + 2B1g + 3Eg) and rutile has four (A1g + B1g + B2g + Eg) [18]. Figure 6.5 shows the Raman spectrum of the annealed powders. All the observed Raman bands in the figure are attributable to anatase and rutile Raman active modes, which is consistent with the XRD patterns. The Raman bands at around 143.30, 197.23, 396.50, 517.49, and 638.49 /cm are respectively due to Eg, Eg, B1g, A1g and Eg for the active modes of both phases. Generally, it has been reported that the anatase transforms to rutile between 500 and 700 ^oC [19]. The appearance after annealing at 600 ^oC of bands that are characteristic of the rutile phase suggests the presence of this transformation. Figure 6.5 shows the intensity analysis of the strongest band at 143.30 /cm (Eg) for anatase TiO_2. This band become more prominent but appears not to evolve with AT. This suggests good quality/stability of the powders. Furthermore, it suggests that the presence of the anatase phase increases with AT, as also suggested by the XRD measurements.

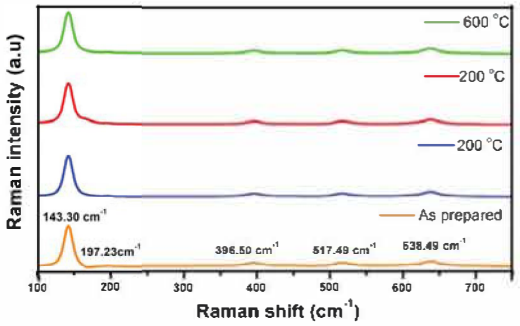

Figure 6.4: Raman spectra of the synthesized nanocrystalline TiO_2 powder at different AT

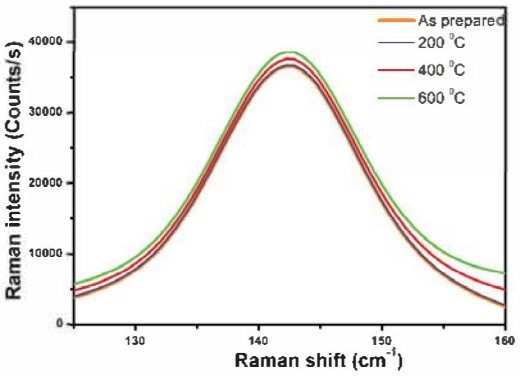

Figure 6.5: Raman intensity analysis of the strongest band at 144 /cm (Eg) for anatase TiO_2

6.4 Morphology analysis

Figure 6.6 shows SEM images of TiO_2 nanostructures of (a) as-prepared, and (b)-(d) annealed at 200, 400 and 600 ^oC, respectively. The particle size is seen to increase with AT. The micrographs suggest that the synthesized nanostructures are good candidates for solar cell applications because large crystalline islands and the associated large, spatial gaps are thought to improve film uniformity and quality over wider expanses of the surface. Wider surfaces allow better contact between TiO_2 nanostructures, photo-active layer and the top electrode. This enhances optical absorption in the photoactive layer.

Figure 6.6(a) also shows an interesting AT-driven evolution of the particle structure from various sized clusters to the more uniform tetragonal shape, shown in Figure 6.6(d), that has (001) and (101) facets. This observation agrees with the foregoing XRD and Raman analyses. It is reported in the literature [20] that an increased (001) to (101) facet ratio generally improves the transfer and separation of photo-generated electrons and holes. This is beneficial to the solar cell as a whole. Figure 6.7 shows SAED patterns of

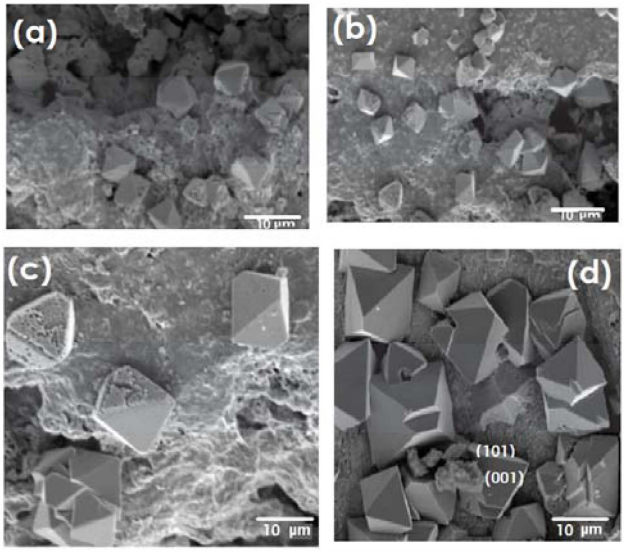

Figure 6.6: SEM micrographs of TiO_2 nanostructures (a) as-prepared, and (b)-(d) annealed at 200, 400 and 600 ^oC, respectively.

anatase TiO_2 nanostructures, (a) as-prepared, and (b)-(d) annealed at 200, 400 and 600 ^oC, respectively. It can be seen that the nanostructures are of highly monocrystalline quality and possess laterally smooth (110) facets and pyramidal ends constructed by (111) facets, as also indicated by SEM. The increased spot brightness in the SAED patterns with AT indicates increased crystallinity, further supporting the earlier XRD results.

6.4.1 Photoluminescent analysis

Figure 6.8 shows the room temperature PL spectra of the as-prepared, and annealed nanocrystalline TiO_2 powders when excited at 229 nm. Photoluminescence

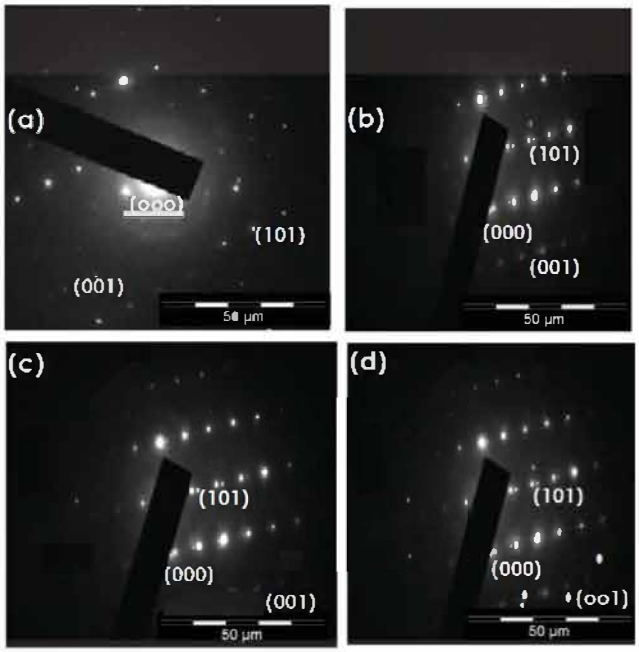

Figure 6.7: HR–TEM images of the TiO_2 nanostructures (a) as-prepared, and (b)-(d) annealed at 200, 400 and 600 ^oC, respectively.

(PL) spectroscopy can reveal useful information about the charge carrier trapping efficiency, migration and transfer in a semiconductor. These mechanisms are initiated during the radiative recombination of photo-generated electrons and holes. For the as-prepared sample, a PL signal around 470 nm only was observed. This is associated with shallow traps on surface oxygen vacancies or defects for both anatase and rutile phases. The anatase band at 470 nm becomes more prominent with increasing temperature. This suggests that shallow traps may contribute to carrier transport via the relatively slower and inefficient diffusion. As such, these traps generally benefit solar energy conversion. Increasing AT to 600 ^oC results in three emission peaks at 407, 416 and 493 nm, i.e. band gap energies of 3.26, 2.98 and 2.52 eV, respectively. The peak at 407 nm originates from the recombination of photo-generated electron-hole pairs [21]. The peak at 416 nm can be attributed to the band-edge free excitons and bound excitons. The peak at 493 nm is due to intrinsic defects resulting from non-stoichiometric factors in TiO_2 or from oxygen vacancies and defects [22]. Figure 6.9 shows the PL emission spectra of the TiO_2 nanocrystals

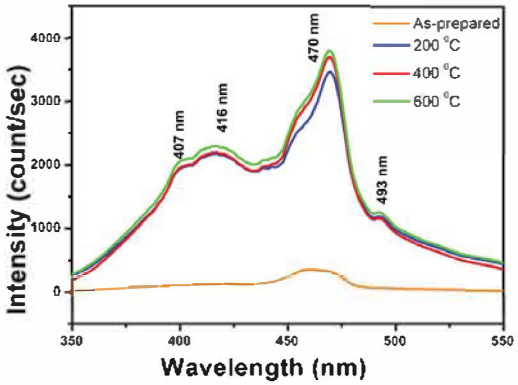

Figure 6.8: Room temperature PL spectra of the annealed nanocrystalline TiO_2 powders.

after deconvolution and Gaussian fitting. Annealing at 600 ^oC produced the

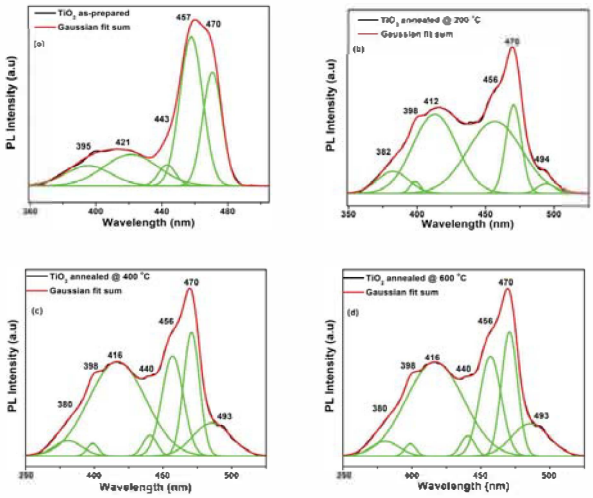

Figure 6.9: Deconvoluted PL spectra of the annealed nanocrystalline TiO_2 powders.

strongest emission, suggesting that with increased AT, crystallization of the anatase phase also increased, along with oxygen based surface vacancies and defects.

6.4.2 UV-Vis spectroscopy

Figure 6.10 shows the UV-Vis spectra of TiO_2 nanocrystals, as-prepared and annealed, used to calculate the band gap. The TiO_2 nanocrystals exhibit absorption peaks in the range of about 343 nm to 380 nm. This is attributed to the direct electronic transition from the bottom of valence band to the top of conduction band. It implies that the synthesized nanocrystals experience spatial excitonic confinement compared to the bulk of TiO_2. The absorption

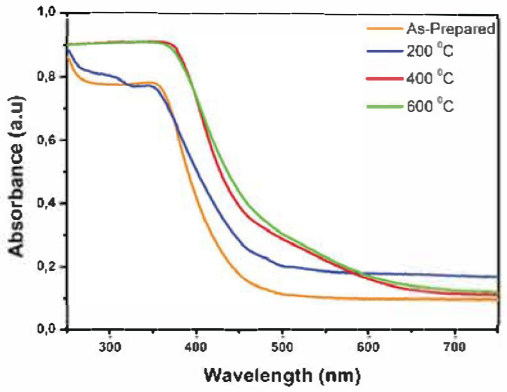

Figure 6.10: UV-Vis absorption spectra of the annealed nanocrystalline TiO_2 powders.

coefficients of the spectra were obtained by conversion from the reflectance spectra using the Kubelka-Munk function:

$$F(R) = \frac{(1-R)^2}{2R} = \frac{K}{S} = A\frac{c}{s}, \tag{6.4.1}$$

where R is the absolute reflectance, K is the molar absorption coefficient, s is the scattering coefficient, c is concentration of the absorbing species and A is the absorbance. Equation 6.4.1 can be modified by multiplying with the Tauc's relation:

$$\big(E\big)^{1/n} = F(R)E, \tag{6.4.2}$$

where $E{=}h\nu$ is photon energy in terms of Planck's constant h, and photon frequency ν. The constant n equals 0.5 for a direct-allowed transition, 2

for non-metallic materials or indirect-allowed transitions, 3/2 for a direct-forbidden transition, and 3 for an indirect-forbidden transition. Figure 6.11 shows how the optical band gap was determined using Tauc's plot i.e. $[F(R)E]^n$ vs E. The estimated band gaps were found to be 3.08, 2.95, 2.79 and 2.73

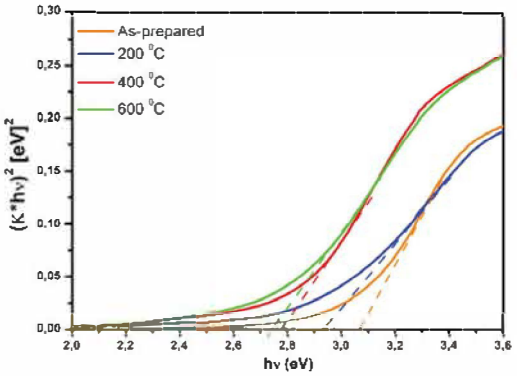

Figure 6.11: Band gap determination using Tauc's plots for the as-prepared, and annealed TiO_2 powder samples.

eV for TiO_2 powders for as-prepared, and annealed at 200, 400, and 600 ^oC, respectively. These values show that band gap decreases as an AT increases. This is thought to be due to widening of interatomic distances as the amplitude of the atomic vibrations increase by virtue of increased thermal energy [23, 24]. These results provide further evidence of increased crystallinity that directly supports the XRD and PL results.

6.5 Conclusions

The effect of AT on phase transformation, crystal structure, crystallinity, particle size, band gap on hydrothermally synthesized TiO_2 nanocrystals was investigated using XRD, Raman, SEM, PL and UV-Vis techniques. XRD suggested the presence anatase and rutile phases with no traces of other TiO_2 phases such as brookite. Raman spectrocopy confirmed the purity of the synthesized powders. SEM and TEM measurements have shown that the

preferred facets of TiO_2 nanocrystals at high temperature are (101) and (001). SAED patterns confirmed high monocrystalline quality of the synthesized TiO_2 powders. PL showed the presence of three main emission peaks that can be attributed to a direct electronic transition from the bottom of the conduction band to the top of the valence band (407 nm), band-edge free excitons (416 nm) and bound excitons and oxygen vacancy defects (493 nm). UV-Vis measurements showed that the band-gap a decreases as the annealing temperature increases, which can be explained in terms of quantum confinement processes. Therefore, hydrothermal synthesis followed by autoclaving at 600 ^oC is a viable, low cost method to synthesize high-quality monocrystalline, tetragonal TiO_2 nanocrystals with predominantly $\{001\}$ faces, that are known to be enhance solar cell device applications.

References

[1] Yan, J., Wu, G., Guan, N., Li, L., Li, Z., Cao, X., 2013. Understanding the effect of surface/bulk defects on the photocatalytic activity of tio$_2$: anatase versus rutile, *Chemical Physics Letters* 15(26):10978–10988.

[2] Peng, JD., Shih, PC., Lin, HH., Tseng, CM., Vittal, R., Suryanarayanan, R., Ho, KC., 2014. TiO_2 nanosheets with highly exposed (001)-facets for enhanced photovoltaic performance of dye-sensitized solar cells, *Nano Energy* 10(26): 212–221.

[3] Wang, Y., Liu, J., Wang, M., Pei, C., Liu, B., Yuan, Y., Liu, S., Yang, H., 2017. Enhancing the sensing properties of TiO_2 nanosheets with exposed (001) facets by a hydrogenation and sensing mechanism, *Inorganic Chemistry*, 56(3):1504–1510.

[4] Dorian, AH., Sorrell, CC., 2011. Review of the anatase to rutile phase transformation, *Journal of Materials Science* 46(4):855–874.

[5] Jacimovic, J., Vaju, C., Gaal, R., Magrez, A., Berger, H., Forro, L., 2010. High-pressure study of anatase tio$_2$, *Materials*, 3:1509–1514

[6] Bajestani, ZG., Yurum, Z., Yurum, A., 2017. Synthesis of anatase TIO_2 with exposed (001) facets grown on n-doped reduced graphene oxide for enhanced hydrogen storage, *International Journal of Hydrogen Energy* 48(9):6096–6103.

[7] Dai, Y., Cobley, CM., Zeng, J., Sun, Y., Xia, Y., 2009. Synthesis of anatase TiO_2 nanocrystals with exposed 001 facets, *Nano Letters* 9(6):2455–2459.

[8] Ding, Y., Huangy, Z., Zhu, J., Kou, S., Zhang, X., Yang, H., 2015. Low-temperature synthesis of high-ordered anatase TiO_2 nanotube array films coated with exposed 001 nanofacets, *Science Reports* 5:17773.

[9] Edy, R., Zhao, Y., Huang, GS., Shi, JJ., Zhang, J., Solovev, AA., Mei, Y., 2016. TiO_2 nanosheets synthesized by atomic layer deposition for photocatalysis, *Progress in Natural Science: Materials International* 26:493–497.

[10] Wang, J., Bian, Z., Zhu, J., Hexing, Li., 2013. Ordered mesoporous TiO_2 with exposed (001) facets and enhanced activity in photocatalytic selective oxidation of alcohols, *Journal of Materials Chemistry A* 1 (4):1296–1302.

[11] Shirke, B.S., Korake, PV., Hankare, PP., Bamane, SR., Garadkar, KM., 2011. Synthesis and characterization of pure anatase TIO_2 nanoparticles, *Journal of Materials Science: Materials in Electronics*, 22:821–824.

[12] Mahdi, E., Hamdi, M., Meor-Yusoff, MS., Wilfred, P., 2013. Xrd and edxrf analysis of anatase nano-TIO_2 synthesized from mineral precursors, *Advanced Materials Research* 620:179–185.

[13] Reyes-Coronado, D., Rodrguez-Gattorno, G., Espinosa-Pesqueira, ME., Cab, C., de Coss, R., Oskam, G., 2008. Phase-pure TIO_2 nanoparticles: anatase, brookite and rutile, *Nanotechnology*, 19(14):10.

[14] Paola, A., Bellardita, M., 2013. Palmisano, Brookite, the least known TIO_2 photocatalyst, *Catalysts* 3:36–73.

[15] Malevu, TD., Ocaya, RO., 2015. Effect of annealing temperature on structural, morphology and optical properties of ZnO nano-needles

prepared by zinc air cell system method, *International Journal of Electrochemical Science*, 10:1752–1761.

[16] Jaafer, HI., Al-Samaraee, AA., Kadhum, AQ., Muslim, ZR., Naji, IS., Obaid, AH., 2015. Effect of annealing temperature on crystal size for the Cu(in,ga)se_2 powder, *International Journal of of basic and applied Science*, 4 (1):3036

[17] Manjula, N., Selvan, G., Ayeshamariam, A., Mohamed, SA., Geetha, N., Jayachandran, M., 2017. Effect of sputtering technique and properties of tio_2 doped with sno_2 thin films, *Fluid Mechanics: Open Access*, 4(5):1000177.

[18] Ohsaka, T., 1980. Temperature dependence of the raman spectrum in anatase TIO_2, *Journal of the Physical Society of Japan*, 48(5):1661–1668.

[19] Abidi, I.H., Cagang, A.A., Tyagi, A., Riaz, M.A., Wu, R., Sun, Q., Luo, Z., 2006. Oxidized nitinol substrate for interference enhanced raman scattering of monolayer graphene, *Royal Society of Chemistry* 6:7093.

[20] Chu, L., Qin, Z., Yang, J., Li, X.,2015. Anatase TIO_2 nanoparticles with exposed 001 facets for efficient dye- sensitized solar cells, *Science Report* 5 :12143.

[21] Aronne, A., Fantauzzi, M., Imparato, C., Atzei, D., De Stefano, L., D'Errico, G., Sannino, F., Rea, I., Pirozzi, D., Elsener, B., Pernice, B., Rossi, A., 2017. Electronic properties of tio_2-based materials characterized by high Ti^{3+} self-doping and low recombination rate of electronhole pairs, *Royal Society of Chemistry Advance* 7:2373–2381.

[22] Dhanalakshmi, J., Iyyapushpam, S., Nishanthi, T., Malligavathy, M., Padiyan, DP., 2017. Investigation of oxygen vacancies in ce coupled tio_2 nanocomposites by raman and pl spectra, *Advance Natural Science: Nanoscience Nanotechnology*, 8(015015):10pp.

[23] Zareen, A., Ali, S., Irfan, M., 2014. The effect of annealing temperature on phase and optical properties of TIO_2 nanoparticles for solar cell application, *European Scientific Journal*, 2:447–450.

[24] Lin, P., Chen, H., Nakaruk, A., Koshy, P., Sorrel, CC., 2013. Effect of annealing temperature on the photocatalytic activity of TIO_2 thin films, *Energy Procedia* 34:627–636.

Chapter 7

Thermal stability study of organic CH_3NH_3I material as perovskite solar cell precursor

7.1 Overview

In this chapter we report on a thermal stability study of perovskite solar cell precursor CH_3NH_3I synthesized by the precipitation method. This work contributes to the understanding of the thermal stability of the components of the bulk material, and also to establishing the range of temperature applicability of the resultant composite solar cell. The structure, morphology, mass loss, thermal and thermal stability of CH_3NH_3I material were investigated using X-ray diffraction (XRD), Scanning Electron Microscopy (SEM), Differential Scanning Calorimetry (DSC), Fourier Transform Infrared (FTIR) spectroscopy and Thermo-Gravimetric Analysis (TGA), respectively. XRD measurements indicated the presence of organic material. TGA analysis suggested that CH_3NH_3I component is stable at temperatures up to 244 ^oC. FTIR analysis identified the functional groups introduced through CH_3NH_3I components.

7.2 Introduction

Perovskites are economically important because of the wide availability of the minerals from which they are typically derived, which often includes rare-earth metals such as cerium, niobium, thorium, lanthanum, titanium, neodymium and others [2]. Rare earth metals further enhance the attractiveness for solar and industrial applications because they introduce defect levels in the energy level, leading to a host of interesting electronic properties. The most commonly used perovskite for photovoltaics is lead methylammonium tri-iodide ($CH_3NH_3PbI_3$). It has high charge carrier mobility and long charge carrier lifetimes, which implies that a photogenerated electron can travel much further to the electrode where recombination can occur. This improved carrier collection leads to more efficient charge extraction [3, 4]. Recent studies have shown that an interfacial metal-oxide layer, particularly zinc oxide (ZnO) and titanium dioxide (TiO_2) dopes the perovskite into an n-type act material. However, the presence of oxygen is generally thought to introduce undesirable interface states that adversely affect the performance of the junction device.

In a perovskite, the presence of oxygen can be eliminated by introducing a $CH_3NH_3PbI_3$ compound [5] with the requisite planarity to assure a polarization to n- or p-type. This planar heterojunction (PHJ) is composed of methylammonium lead iodide ($CH_3NH_3PbI_3$) with high charge carrier lifetimes. Pervoskites are also interesting also because of this tunability of their effective polarity to either n-type or p-type, leading to a wealth of possible bulk-heterojunction (BHJ) devices using numerous organic-inorganic blends. However, there is some confusion regarding the properties that are important in a particular perovskite and its suitability for a given solar application. It is therefore useful to ascertain such attributes, which appear to depend on several factors such as the precursors, the molecular structure and the constituent atoms.

This chapter investigates the role that the precipitation synthesis route plays on the thermal and structural properties of lead iodide perovskite. Recent studies suggest that thermal behaviour of solar cell materials can play a significant role in tuning the structure of the materials [6]. This raises the possibility to optimize the performance of the final device through thermal treatment [7, 8]. Furthermore, understanding the stability of the components of the composite bulk material is important for the application domain of the resultant device. In this study, we specifically analyze the effect of heat treatment on the precursor components of hybrid organic–inorganic/lead-based perovskites for BHJ application, with the overarching aim of fostering a clearer understanding of the thermal properties of the perovskite.

7.2.1 Results and Discussion

7.2.2 Structural analysis

Figure 7.1 shows XRD pattern of the synthesized CH_3NH_3 compound. However, a perusal of the JCPD library does not reveal a matching card for CH_3NH_3I.

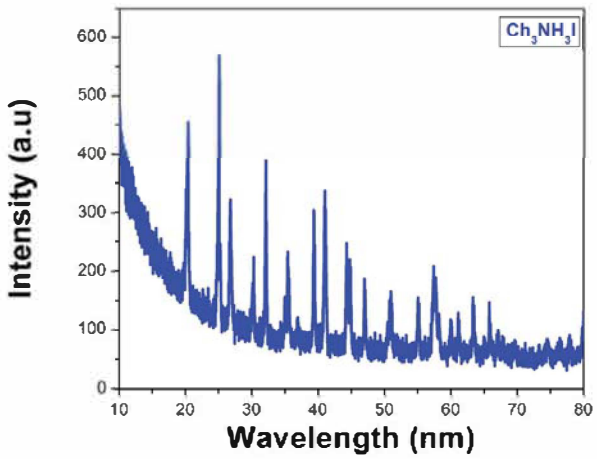

Figure 7.1: XRD patterns of the synthesised CH_3NH_3I

7.3 Surface Morphology

Figure 7.2 shows the SEM micrographs of the surface morphologies of the synthesized organic precursor. Comparisons between the materials show minor

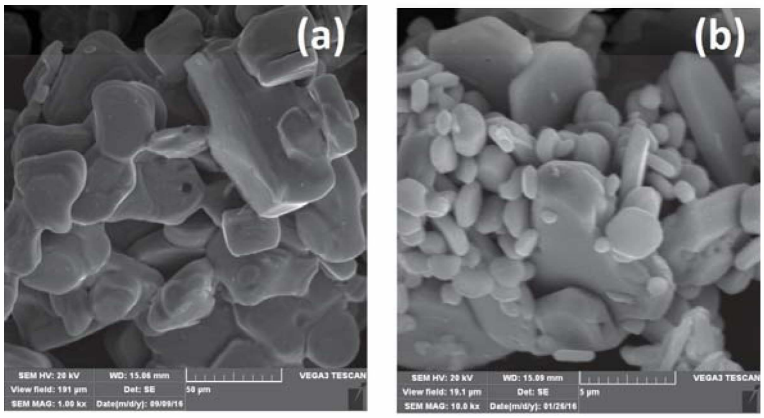

Figure 7.2: SEM micrographs of (a) organic CH_3NH_3I compound and (b) inorganic PbI_2 nanoparticles

differences in surface morphology. The preferred shapes are hemispherical, with varying diameters down to nanosizes, for both materials. This could indicate good spatial compatibility of both materials when blended together. For solution-processed organic BHJ solar cells, the morphology of the active layer is known to be critical to the device performance. Many previous studies have demonstrated significant influences of the third component as an additive on morphology and device performance [10]. The figure also shows evidence of agglomeration of nanoparticles into larger clusters.

7.3.1 Thermodynamic stability analysis

Figure 7.3 shows the result of TGA analysis to determine the mass loss versus temperature behavior of the organic component that make up the building blocks of $CH_3NH_3PbI_3$. The sublimation behavior of the isolated organic component is examined in depth and used to interpret the TGA data of various perovskite precursors. This result shows that the organic component CH_3NH_3I undergoes 100 % weight loss in one step, with the degradation curve showing

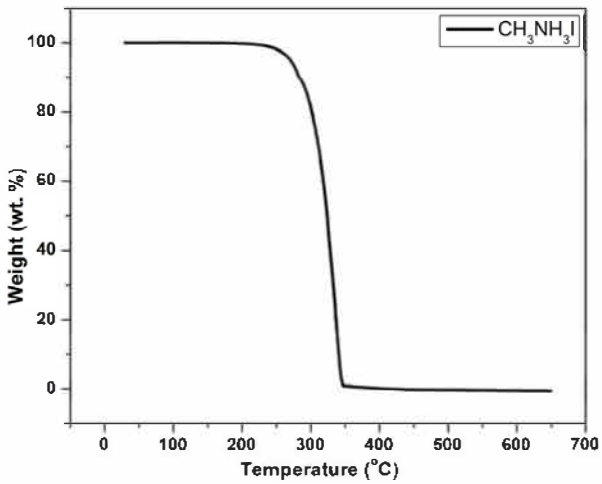

Figure 7.3: TGA heating curve of CH_3NH_3I powder corresponding to first derivative

no weight loss up to 244 ^{o}C. This suggests that the material is thermally stable up to this temperature. No coordinated water molecules or water of crystallization was observed in this organic compound. Figure 7.4 shows the result of differential TGA analysis. The sharpness of the transition step supports the observed thermal stability up to 244 ^{o}C in Figure 7.3.

7.3.2 Differential scanning calorimetry (DSC)

DSC is a foremost analysis technique that is central to thermal analysis. It is invaluable because of its ability to resolve the thermal transitions in the studied material. For perovskites these transitions include the melting, crystallization, and degradation or decomposition. In this work, the particular DSC results reported were obtained from a secondary DSC scan in order to eliminate the effect of thermal history from the results. Table 7.1 shows the normalized melting enthalpy, defined as ΔH_m^{norm}, for all the samples, according to Equation 7.3.1.

$$\Delta H_m^{\text{norm}} = \frac{\text{measured } \Delta H}{\text{measured mass}} \tag{7.3.1}$$

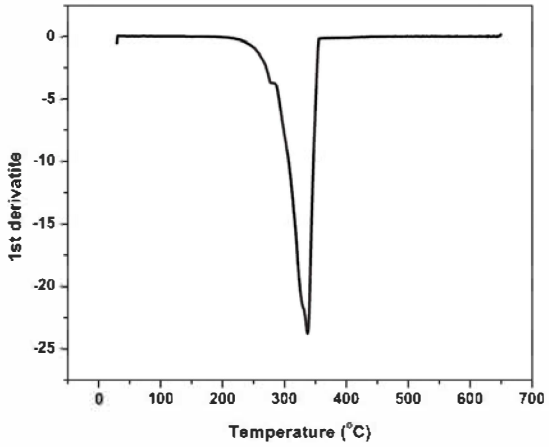

Figure 7.4: Derivative weight loss of CH_3NH_3I powder corresponding to first derivative

The DSC results for the organic CH_3NH_3I powder are summarized in Figures 7.5 and 7.6 respectively. The secondary DSC scans for methylammonium compound show two peaks at 108 and 108 ^oC for the cooling and heating scans, respectively.

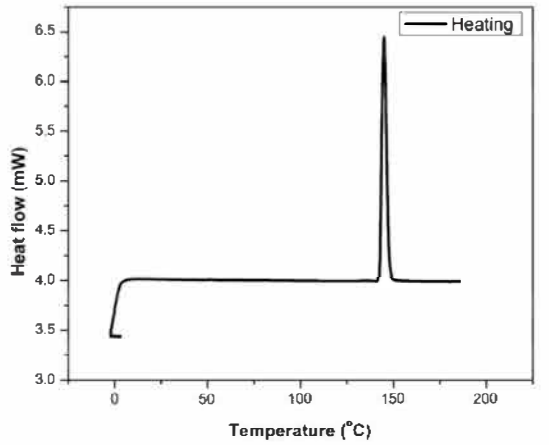

Figure 7.5: DSC heating curve of organic CH_3NH_3I

These results are in good agreement with the reported tetragonal-to-cubic martensitic transition of $CH_3NH_3PbI_3$. The asymmetry of the DSC peaks is thought to indicate the presence of a transient, intermediate phase,

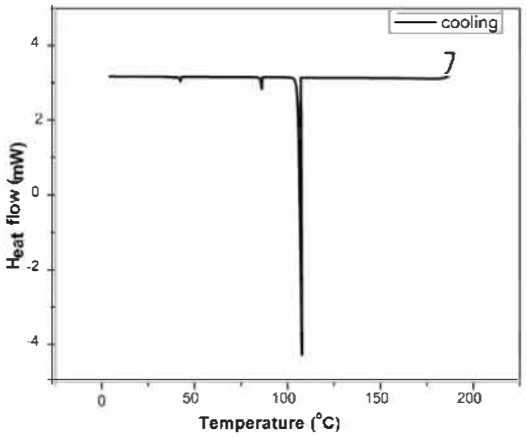

Figure 7.6: DSC cooling curve of organic CH_3NH_3I

Table 7.1: Summary of the DSC heating results for organic CH_3NH_3I samples

Summary of the DSC heating results		
Sample	First heating/ ^oC	Cooling/ ^oC
Onset Temperature	141.70	107.21
Peak Temperature	144.25	107.21
Delta H	44.28	39.06
X-axis	80 - 185	20 - 160

but further literature evidence is scant [25].

7.3.3 Fourier-transform infrared analysis (FTIR)

FTIR analysis was conducted to further confirm the structure and thermal stability of both organic and inorganic compounds. Figure 7.7 shows the FTIR spectrum of methylammonium compound. All the vibrational modes, appearing as peaks in the figure, are assigned either to NH_3 and CH_3 organic groups. All NH_3-related peaks are stronger than the corresponding CH_3 vibrations. This is a consequence of the positive charge that is located on the ammonium group that enhances the change in dipole moments related

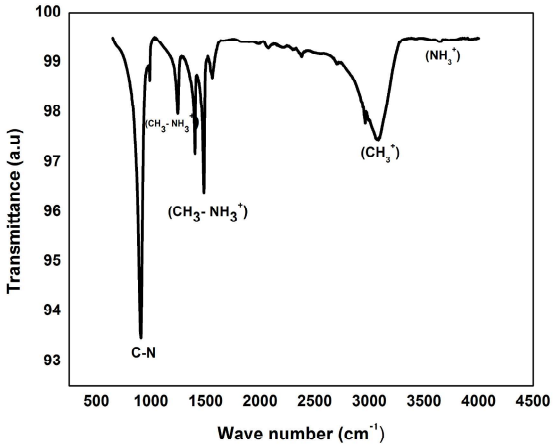

Figure 7.7: FTIR spectrum curve of organic CH_3NH_3I

to the NH_3 vibrations. The strong peak around 902/cm is attributed to C-N stretching, while (1237 and 1397/cm), (1480 and 3088/cm) and 3650/cm peaks are attributed to CH_3 - NH_3^+, symmetrical CH_3 bend, symmetrical NH_3^+ respectively.

7.4 Conclusion

We have reported on the thermal stability analysis of organic CH_3NH_3I perovskite solar cell precursor that were synthesized using a simple precipitation method. XRD, SEM, TGA, DSC and FTIR measurements confirm that the as-synthesized compounds have high purity and are stable at high temperatures. This work contributes to an understanding of the application temperature domains of the resultant perovskite BHJ solar cells by underscoring any potentially limiting thermal degradation effects within their constituent compounds which are directly part of the bulk. The investigations confirm that the precursors exist as organic CH_3NH_3I compound, that is stable at much higher than ambient temperatures and therefore potential candidates for harsher conditions.

References

[1] Attfield, J.P., Lightfoot, P., Morris, R.E., 2015. Perovskite, *Royal society of chemistry*, 44:10541

[2] Asif, A.A., Singh, R., Alapatt, G.F. 2015. Technical and economic assessment of perovskite solar cells for large scale manufacturing, *Journal of Renewable and Sustainable Energy*, 7(4):043120

[3] Zhao P, Bian L, Wang L, Xu J, Chang A, 2014. Enhanced open voltage of $BiFeO_3$ polycrystalline film by surface modification of organolead halide perovskite, *Applied Physics Letters*, 105(1):013901.

[4] Phillips, L.J., Rashed, A.M., Treharne, R.E., Kay, J., Yates, P. Mitrovic, I.Z., Weerakkody, A., Hall, S., Durose, K., 2016. Maximizing the optical performance of planar $CH_3NH_3PbI_3$ hybrid perovskite heterojunction stacks, *Solar Energy Materials and Solar Cells*, 147:327-333

[5] Tseng, Z.L., Chiang, C.H., Wu, C.C., 2015. Surface Engineering of ZnO Thin Film for High Effciency Planar Perovskite Solar Cells, *Scientiffc Reports*, 5:13211

[6] Malevu, T.D., Ocaya, R.O., 2015. Effect of Annealing Temperature on Structural, Morphology and Optical Properties of ZnO Nano-Needles Prepared by Zinc-Air Cell System Method , *Int. J. Electrochem. Sci.*, 10:1752–1761

[7] Brunetti, B., Cavallo, C., Ciccioli, A., gigli, G., Latini, A., 2016. On the Thermal and Thermodynamic (In)Stability of Methylammonium Lead Halide Perovskites, *Scientific Reports*, 6:31896

[8] Jung, M., Kim, Y.C., Jeon, N.J., Im, S.H., 2016. Thermal Stability of CuSCN Hole Conductor-Based Perovskite Solar Cells, *ChemSusChem*, 9:1–6

[9] Malevu, T.D., Ocaya, R.O., Tshabalala, K.G., Fernandez, C. 2016. Synthesis and characterization of high quality PbI_2 nanopowders from depleted SLA accumulator anode and cathodes, *Applied Physics A: Materials Science*: 122:630

[10] Mai, J., Lau, T., Li, J., Peng, S., Hsu, C., Jeng, U., Zeng, J., Zhao, N., Xiao, X., Lu, X., 2016, Understanding Morphology Compatibility for High-Performance Ternary Organic Solar Cells, *Chemistry of Materials*, 28:6186–6195

[11] Kaviyarasu, K., Sajan, D., Selvakumar, M.S., Thomas, S.A., Anand, D.P, 2012. A facile hydrothermal route to synthesize novel PbI_2 nanorods, *Journal Physics and Chemistry of solids*, 73(11):1396–1400

Chapter 8

Effect of 6R and 12R lead Iodide Polytypes on $MAPbX_3$ Perovskite Device Performance

8.1 Overview

We compare the structural, morphological and electrical properties of two variants on the ITO/ZnO/$CH_3NH_3PbI_3$/PEDOT:PSS/Au thin film perovskite device made using two structurally different forms of lead iodide. The first device was based on a commercially sourced, common 12R polytype. The second device uses the rarer 6R polytype, as recently synthesized by the authors from depleted sealed lead acid batteries. XRD measurements confirmed the presence of the orthorhombic 6R polytype and the tetragonal 12R polytype. Raman spectroscopy confirmed the presence of all organic-inorganic halide materials. Current–Voltage measurements for both samples show good rectifying behavior of the resulting heterogeneous Schottky diodes. The ideality factors and barrier heights were found to be 4.07/4.09 and 0.500/0.496 eV for the 6R/12R polytypes, respectively. The 6R polytype devices appeared to show improved I-V characteristics in comparison to the 12R polytype, thus suggesting an avenue to enhance the performance of MAPbX3 prevoskite devices.

8.2 Introduction

Methylammonium lead halide ($MAPbX_3$, where X = Br, I or Cl) devices have a demonstrated potential for photovoltaic applications although they are currently dogged by several implementation challenges. The first concerted attempts to deploy $MAPbX_3$ in solar cell applications was as dyes in bromine or iodine dye-sensitized solar cells. The earliest-reported power efficiencies were around 3.8%. This figure was quickly raised to around 6.5% by optimizing synthesis conditions such as coating solutions, annealing and electrolyte concentration [1].

By attempting other perovskite recipes [2], reported perovskite solar cell performances are approaching the predicted maximum power efficiency of 22.1%. For instance, record efficiencies have been reported for various configurations, such as deposition on TiO_2 coated ITO substrate, and halide based thin films [3] of the form $CH_3NH_3PbI_{3-x}Cl_x$. In such blends, the stochiometric ratio (x) of two halides is tuned for optimum solar cell performance and band gap. However, for many of these configurations few reports are available with respect to the absorber film. This has led to low reproducibility within the community at present, thus leaving much scope for continued research.
In this work, we report on the room-temperature fabrication and characterization of $MAPbI_3$ thin films based on the 6R and 12R distinct polytype precursors of PbI_2. The structural, morphological, optical and photovoltaic properties are investigated with the aim to optimize and improve photovoltaic performance. This work indirectly reports on room-temperature synthesis, although perovskite solar cells are typically fabricated in low-humidity atmospheres, such as inside dessicated glove boxes [4, 5].

8.2.1 Structural analysis

Figure 8.1 shows the XRD pattern of the synthesized ZnO nanorods. All the assigned peaks correspond to the standard JCPDS card no: 36-1451 with no external impurities observed. The observed diffraction peaks at 31.77, 34.42, 36.25 and 47.53^o correspond to the (100), (002), (101) and (102) planes. The figure shows that purely crystalline nanorods with a preferred (002) orientation were formed. Figure 8.2 shows the XRD pattern of $MAPbI_3$ films prepared

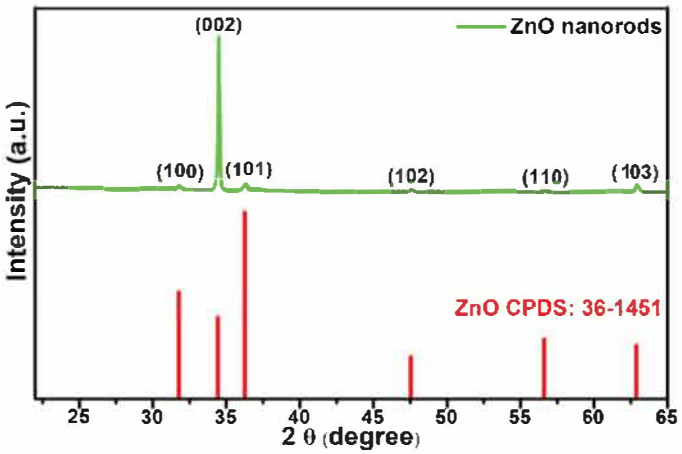

Figure 8.1: XRD patterns of the synthesized ZnO nanorods

from (a) commercial materials, and (b) synthesized materials, coated ontoZnO nanorods. For both materials, a series of additional diffraction peaks were observed at 12.69, 25.55, 26.02, 38.69 and 41.80^o. These peaks correspond to the (001), (002), (101), (003) and (111). They are due to residual PbI_2 (JCPDS No. 07-0235), suggesting an incomplete conversion of PbI_2 to $MAPbI_3$ during synthesis. The presence of unreacted lead iodide, which is observed for both 6R and 12R based synthesis, could lead to poor performance of the final device due to the introduction of interface states [8]. The diffraction peaks at 14.12, 40.40 and 43.99^o, which are seen in both routes, are indexed to the (110), (224) and (314) planes of orthorhombic $MAPbI_3$. The additional

peak at 28.51^o (220) with a shoulder peak at 28.19^o (004) is seen in the product based on the commercial precursor while the synthesized, 6R based material exhibits an additional peak at 20.01^o (112). All the diffraction peaks observed correspond to the tetragonal phase of $MAPbI_3$ [9, 3, 11, 13]. The XRD results for both the synthesized and the commercially based sources do not exhibit the characteristic peaks of PEDOT:PSS, suggesting that the spin-coated PEDOT:PSS remained amorphous and did not affect the $MAPbI_3$ product crystallinity [14].

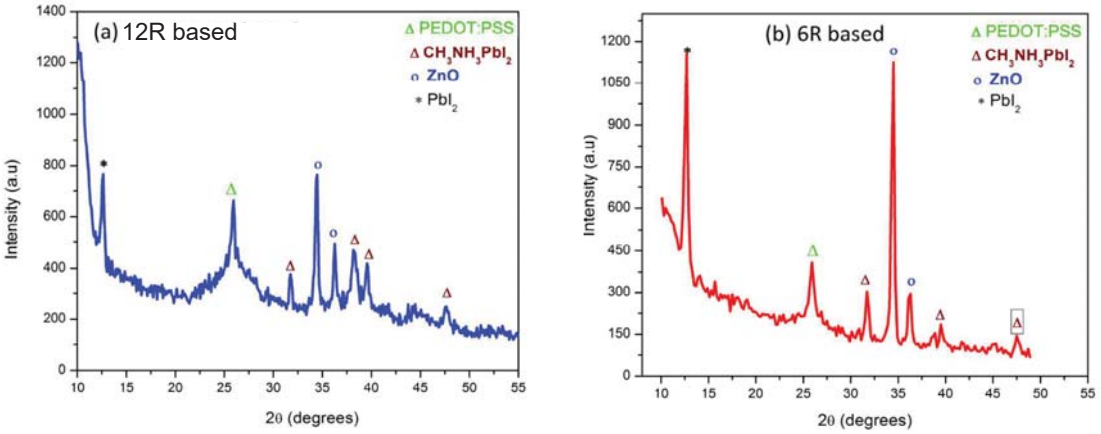

Figure 8.2: XRD patterns of the synthesized $MAPbI_3$ from (a) commercial sources, and (b) synthesized materials

8.2.2 Raman analysis

Raman spectroscopy was used to characterize chemical bond vibrations and to identify different materials in the synthesized $MAPbI_3$ thin films. Figures 8.3 and 8.4 respectively show the Raman spectrum for 6R and 12R polytype originated $MAPbI_3$ perovskites. The dominant PEDOT:PSS peak is observed around 1434.79/cm. This peak corresponds to the symmetrical stretching mode of the atomic C=C bond [15]. The peaks around 1507.66/cm are attributed to thiophene rings of PEDOT:PSS that arise from C=C bonds. The peak at 1577.09/cm is associated with the splitting of asymmetrical vibrations. The peaks around 1356.28/cm and 1261.66/cm are attributed to C_α-C_α inter-ring, asymmetric and C_β-C_β stretching deformations, respectively

[14]. The Raman scattering measurements also indicate the presence of ZnO

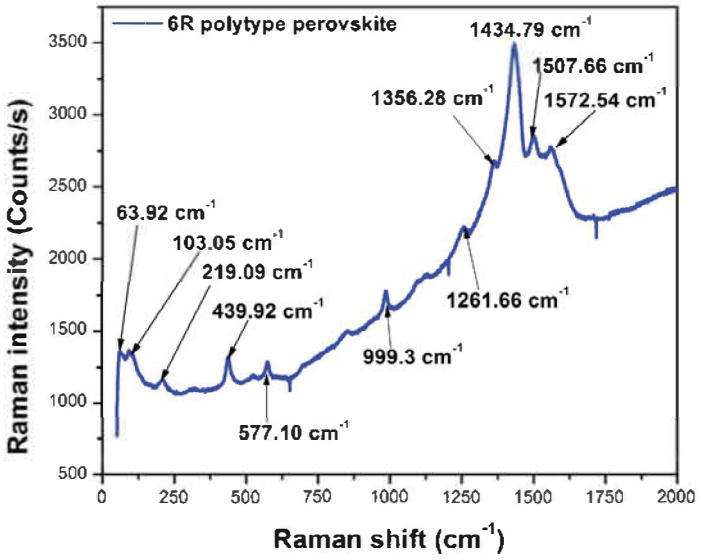

Figure 8.3: Raman spectrum for 6R polytype based perovskite excited at 514 nm wavelength

nanorods. The peaks at 439.92/cm and 577.10/cm respectively correspond to the E_2 (high) and E_1(low) modes of the wurtzite structure of ZnO [15], [16]. Furthermore, the presence of inorganic-organic halide material is also indicated. The peak at 68/cm reveals a major component from the vibrations of organic cations and also Pb-I bending. The peak at 103/cm corresponds to Pb-I stretching, which are the characteristic modes of the inorganic cage in the perovskite crystal structure [16, 17, 18]. Finally, the bands at around 211 and 219/cm are assigned to the torsional modes of the methylammonium cation [19].

8.2.3 Surface morphology

Figure 8.5 shows vertically well-aligned hexagonal-shaped ZnO nanorods with diameters ranging from 30 nm to 100 nm grown on the seeded ITO substrate. Such nanorods are thought to facilitate the movement of charge carriers to the

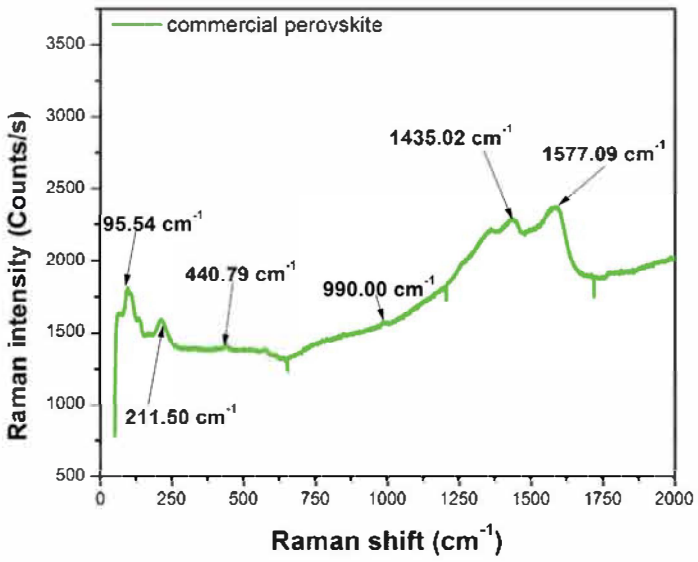

Figure 8.4: Raman spectrum for commercial 12R polytype based perovskite excited at 514 nm wavelengths

electrodes through the optimal arrangement without any recombination losses at nanorod boundaries. It has been reported in transient photo-current/voltage studies that recombination losses during electron transport through ZnO nanorods are negligible [21, 22].

Figure 8.6 shows the top and lateral views of the SEM morphology of both perovskites. Figure 8.6 (a) depicts the 6R polytype PbI_2 based perovskite. Small spherical particles are visible from the tip of ZnO nanorods comprising of layers of perovskite and PEDOT:PSS. Figure 8.6 (b) depicts commercially based perovskite, which has a morpology that is similar to the synthesized 6R polytype based product. The uniform distribution of spherical crystals observable in both micrographs implies that both methods realize high quality perovskite films on the ZnO nanorods substrate. Figure 8.6 (c) shows a rough cross section indicating similar, vertically well-aligned ZnO nanorods. Nanorod geometry provides a higher interfacial surface area between the perovskite and ZnO. This is thought to increase electron transport towards the conducting substrate [23, 24].

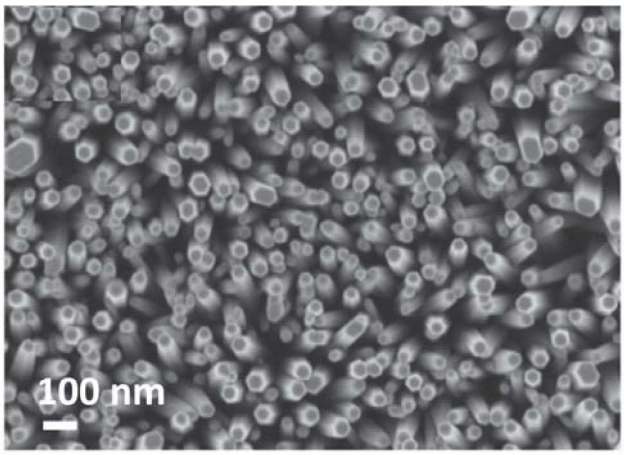

Figure 8.5: SEM images of the synthesized ZnO nanorods

Figure 8.6 (d) shows a cross section of the thin film which indicates how perovskite layer embeds itself in the nanorods. In the figure there is no evidence of either PbI_2 and MAI capping layers which indicates that PbI_2 and MAI were completely converted to perovskite during the deposition, as confirmed by XRD. Also, the absence of voids on the perovskite surface indicates a smooth deposition during spin coating. Figure 8.7 is a cross-section showing a thick perovskite absorber layer sandwiched between an electron transporting layer (ETL) and hole transporting layer (HTL). Figure 8.7 shows the structure of the final device. It can be seen in Figure 8.7(a) that the thickness of the layers, particularly PEDOT:PSS varies from the top to the bottom of the figure, due to solution dropping variations during spin-coating. The different layers are recognizable in the inset. Figure 8.7(b) is the schematic of the completed device.

8.2.4 Electrical characterization

The resultant heterogeneous metal-semiconductor thin-film solar cells have the structure ZnO:$MAPbI_3$/PEDOT:PSS, where $MAPbI_3$ is either 6R or 12R polytype based, as presented in the foregoing sections. The electrical performance of the devices were investigated using I-V measurements. Several samples

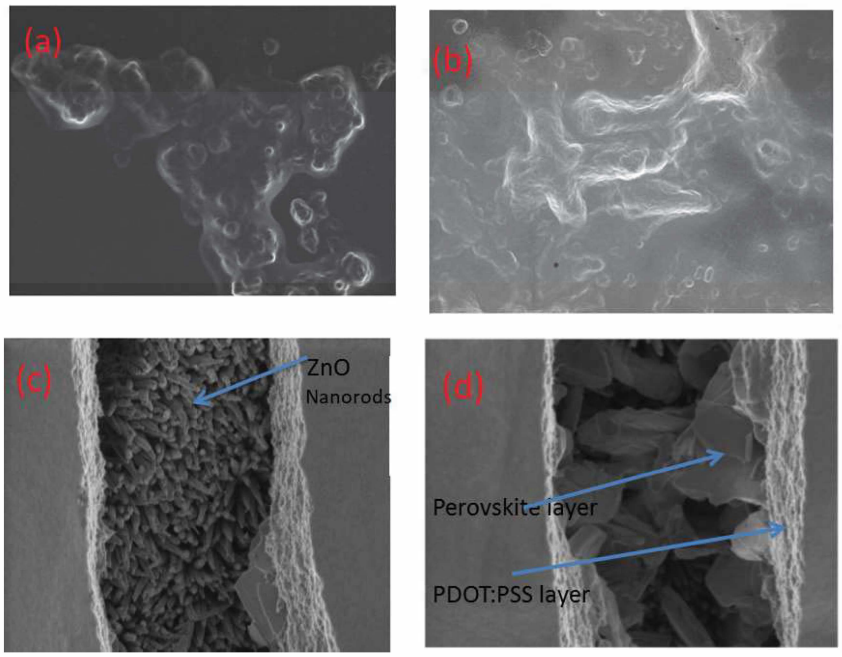

Figure 8.6: SEM micrographs showing (a) 6R-based perovskite (b) 12R-based perovskite (c) rough cross-section (d) perovskite/ZnO nanorods interfaces

of each device were constructed and the measurements described below were repeated on all of them. Figure 8.8 is a semilog I–V plot under dark conditions. Both devices exhibit similar rectifying behavior, due to the formation of Schottky junction between the Au metal contact and the perovskite. The dark current is seen to be marginally higher for the 6R based diode at any bias voltage. According to the thermionic emission theory, the current in a Schottky diode of series resistance R_s and applied voltage V is given by

$$I = I_0 \left[1 - \exp\left(\frac{-q(V - IR_s)}{k_B T} \right) \right], \tag{8.2.1}$$

where q is electronic charge, k_B is Boltzmann's constant, T is absolute temperature. The term I_0 is the zero-bias saturation current:

$$I_0 = AA^{**}T^2 \exp\left(\frac{-q\Phi_{B0}}{\eta k_B T} \right), \tag{8.2.2}$$

where A is the diode contact area, A^{**} is Richardson's constant, Φ_{B0} is the zero-bias barrier height. The term η is the ideality factor, which equals unity in a purely thermionic emission regime. The measurements were done at room

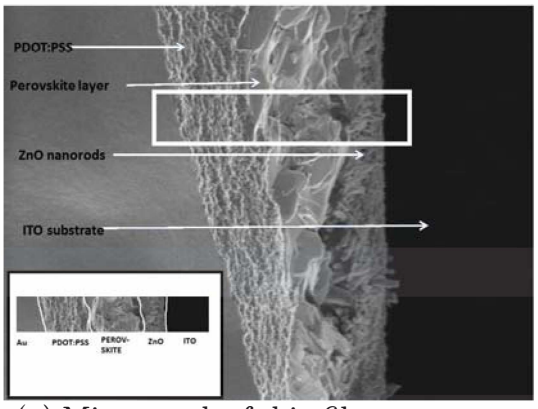

(a) Micrograph of thin film structure

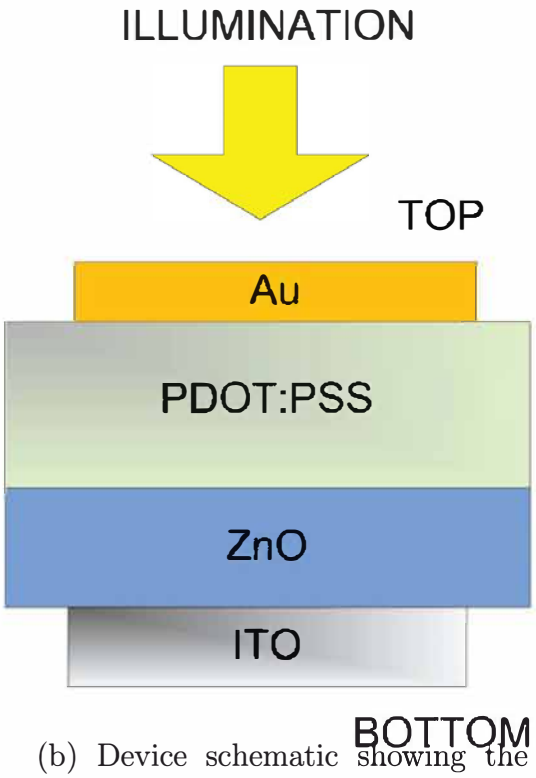

(b) Device schematic showing the layer stack

Figure 8.7: he structure of the completed perovskite solar cell. The inset in (a) shows the layer boundaries in the white boxed region.

temperature (300K). Equation 8.2.1 is a reasonable approximation provided that $V \geq k_B T/q$. The calculated η are summarized in Table 8.1.

Table 8.1: Calculated ideality factor of 6R and 12R polytype perovskite.

Phase	6R Ideality Factor (c)	12R Ideality Factor (η)	Ref.
η	4.06	4.1	[25]
η	4.07	4.1	[26]
η	4.07	4.09	This experiment

Using Equation 8.2.2 the estimated Φ_{B0} was found to be 0.500±0.008 eV (6R) and 0.496±0.008 eV (12R). The values are equal within the limits of measurement error, indicating that both materials have the same work function. Figure 8.9 shows the dark and illuminated I–V characteristics of the final 6R and the 12R polytype based solar cells.

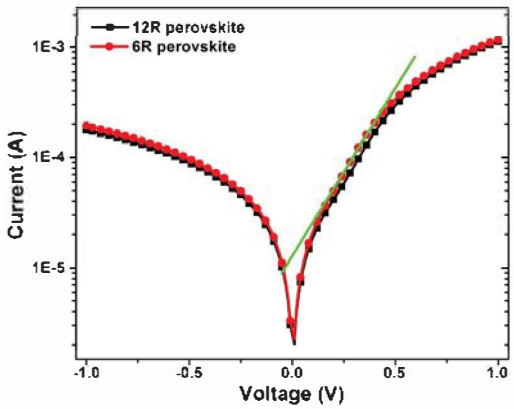

Figure 8.8: Semi-logarithmic I–V characterization of 6R and 12R polytype perovskite polystye

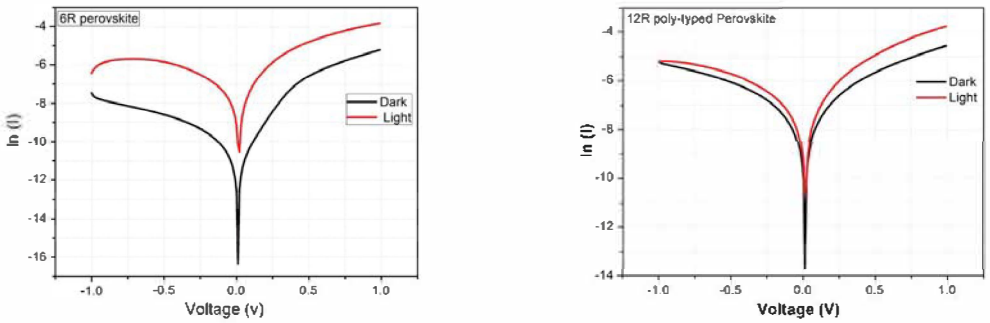

(a) 6R (b) 12R

Figure 8.9: I–V characteristics of the fabricated perovskite solar cells under dark and 100 mW/cm^2 illumination.

Both devices clearly exhibit photoconductive and photovoltaic response. Under 100 mW/cm^2 illumination and 1.0V bias voltage the photocurrent measured for the 6R polytype based device (1.40 mA) is 77% higher than for the 12R polytype based device (0.79 mA). This significant difference can only be attributed to the polytype used in the given device. Hence, the polytype used differentiates the current responses of the device.

8.3 Conclusions

This study has focused on establishing a link between two lead iodide polytype precursors (6R and 12R) and the performance of the resultant methylammonium lead iodide perovskite solar cells fabricated from them. The 6R and 12R polytypes are known to arise from the synthesis route taken for the lead iodide precursor in the fabrication of perovskite. The polytype used in the final perovskite Schottky diode is shown to significantly affect the photocurrent. The electrical, photoconductive and photovoltaic responses of the final device appear to favour the use of the 6R precursor over the 12R polytype, suggesting that such devices would in general benefit from 6R lead iodide. In future studies it would be instructive to investigate the precursor structure of the lead halide precursors, particularly with respect to chlorine or bromine compounds, and even mixes. Furthermore, more detailed photo-transient and impedance capacitance-voltage studies can be conducted.

References

[1] Im, J.H., Lee, C.R., Lee, J.W,. Park, S.W., Park, N.G., 2011. 6.5 percent efficient perovskite quantum-dot-sensitized solar cell, *Royal Society of Chemistry*, 3:4088-4093.

[2] Giustino F, Snaith H.J., 2016. Toward lead-free perovskite solar cells, *ACS Energy Letters* 1:1233–1240.

[3] Lee, M., Teuscher, J., Miyasaka, T., Murakami, T.N., Snaith, H.J., 2012. Efficient hybrid solar cells based on meso-superstructured organometal halide perovskites, *Science* 2(338):643-647.

[4] Wang, W.T., Das, S.K., Tai, Y., 2017. Fully ambient-processed perovskite film for perovskite solar cells: Effect of solvent polarity on lead iodide, *Applied materials and interfaces* 9:10743–10751.

[5] Zhou, Q., Jin, Z., Li, H., Wang, J., 2016. Enhancing performance and uniformity of $CH_3NH_3PbI_3Cl_x$ perovskite solar cells by air-heated-oven assisted annealing under various humidities, *Science Report*, 6:21257.

[6] Mwankemwa BS, Nambala FJ, Kyeyune F, Hlatshwayo TT, Nel JM, Diale M, 2017. Influence of ammonia concentration on the microstructure, electrical and Raman properties of low temperature chemical bath deposited ZnO nanorods, *Materials Science in Semiconductor Processing* 71:209-216.

[7] Malevu, T.D., Ocaya, R.O., Tshabalala, K.G., Fernandez, C. 2016. Synthesis and characterization of high quality PbI_2 nanopowders from depleted SLA accumulator anode and cathodes, *Applied Physics A: Materials Science*: 122:630

[8] Wang, K., Liu, C., Du, P., Zhang, H., Gong, X., 2015. Efficient perovskite hybrid solar cells through a homogeneous high-quality organolead iodide layer, *Material Views*, 11(27):3369-3376.

[9] Yu, J., Chen, X., Wang, Y., Zhou, H., Xue, M., Xu, Y., Li, Z., Ye, C., Zhang, J., van Aken, PA., Lund, P.D., Wang, H., 2016. A high-performance self-powered broadband photodetector based on a $CH_3NH_3PbI_3$ perovskite/ZnO nanorod array heterostructure, *Journal of Materials Chemistry C* 4:7302-730.

[10] Zhao, P., Bian, L., Wang, L., Xu, J., Chang, A., 2014. Enhanced open voltage of $BiFeO_3$ polycrystalline film by surface modification of organolead halide perovskite, *Applied Physics Letters*, 105:013901.

[11] Rahman, M.M., Uekawa, N., Shiba, F., Okawa, Y., Sakai, M., Yamamoto, K., Kudo, K., Konishi, T., 2016. Effect of the filtration of PbI_2 solution for zinc oxide nanowire based perovskite solar cells, *Japanese Journal of Applied Physics*, 55:01AE09.

[12] Hutter, E.M., Glvez-Rueda, M.C., Osherov, A., Bulovi, V., Osherov, F.C., Stranks, S.D., Savenije, T.J., 2016. Directindirect character of the bandgap in methylammonium lead iodide perovskite, *Nature Materials* 16:115-121.

[13] Zou, X., Fan, H., Tian, Y., Yan, S., 2014. Synthesis of Cu_2O/ZnO hetero-nanorod arrays with enhanced visible light-driven photocatalytic activity, *CrystEngComm*, 16(6):1149–1156

[14] Singh, V., Arora, S., Arora, M., Sharma, V., Tandoh, R.P., 2014. Characterization of doped PEDOT:PSS and its influence on the performance and degradation of organic solar cells, *Semiconductor Science and Technology*, 29(045020): 8pp.

[15] Zamiri, R., Rebelo, A., Zamiri, G., Adnani, A., Kuashal, A., Scott Belsley, M., Ferreira, J.M.F., 2014. Far-infrared optical constants of ZnO and ZnO/Ag nanostructures, *Royal Society of Chemistry* 4:20902-20908.

[16] Das, D., Mondal, P., 2014. Photoluminescence phenomena prevailing in c-axis oriented intrinsic ZnO thin films prepared by rf magnetron sputtering, *Royal Society of Chemistry* 4:35735-35743.

[17] Ledinsky, M., Loper, P., Niesen, B., Holovsky, J., Moon, S., Yum, J., De Wolf, S., Fejfar, A., Balli, C., 2015. Raman spectroscopy of organicinorganic halide perovskites, *The Journal of Physical Chemistry Letters* 5:401-406.

[18] Quarti, C., Grancini, G., Mosconi, E., Bruno, P., Ball, J.M., Lee, M.M., Snaith, H.J., Petrozza, A., Angelis, F.D., 2014. The Raman spectrum of the $CH_3NH_3PbI_3$ hybrid perovskite: Interplay of theory and experiment, *The Journal of Physical Chemistry Letters*, 5:279-284.

[19] Liang, Z., Zhang, S., Xu, X., Wang, N., Wang, J., Bi, Z., Xu, G., Yuan, N., Ding, J., 2015. A large grain size perovskite thin film with a dense structure for planar heterojunction solar cells via spray deposition under ambient conditions, *Royal Society of Chemistry* 5:60562-60569.

[20] Pistor, P., Ruiz, A., Cabot, A., Izquierdo-Roca, V., 2016. Advanced Raman spectroscopy of methylammonium lead iodide: Development of a nondestructive characterization methodology, *Scientific Reports* 6:35973.

[21] Kislyuk, V.V., Dimitriev, O.P., 2008. Nanorods and nanotubes for solar cells, *Journal of Nanoscience and Nanotechnology* 8:131-148.

[22] Yang, L., Barrows, A.T., Lidzey, D.G., Wang, T., 2016. Recent progress and challenges of organometal halide perovskite solar cells, *Reports on Progress in Physics* 79(026501):26pp

[23] Valls, I.G., and Cantu, M.L., 2009. Vertically-aligned nanostructures of ZnO for excitonic solar cells: a review, *Energy and Environmental Science*, 2:19–34

[24] Ravirajan, I.G., Peiro, A.M., Nazeeruddin, M.K., Graetzel, M., Bradley, D.D.C., Durrant, J.R., Nelson, J., 2006. Hybrid Polymer/Zinc Oxide Photovoltaic Devices with Vertically Oriented ZnO Nanorods and an Amphiphilic Molecular Interface Layer, *Journal of Physical Chemistry B*, 110(15):7635–7639

[25] Agarwal, S., Seetharaman, M., Kumawat, N.K., Shaibal, A.S., Sarkar, S.K., Kabra, D., Namboothiry, M.A.G., Nair, P.R., 2014. On the uniqueness of ideality factor and voltage exponent of perovskite-based solar cells, *The Journal of Physical Chemistry Letters*, 5(23):4115-4121.

[26] Kanda, H., Uzum, A., Baranwal, A.K., Nirmal Peiris T.A., Umeyama, T., Imahori, H., Segawa, H., Miyasaka, T., Ito, S., 2016. Analysis of sputtering damage on iv curves for perovskite solar cells and simulation with reversed diode model, *The Journal of Physical Chemistry Letters*, 120(50):28441–28447.

Chapter 9

Effect of annealing temperature on $MAPbX_3$ perovskite solar cell performance fabricated in ambient atmosphere

9.1 Overview

A major issue when fabricating a perovskite solar cells is that some processes must be done using a high vacuum or an inert atmosphere inside a glove box. This results in an increased production cost due to the fact that vacuum related equipment are very expensive. We report on work that was done in ambient air environment in order to facilitate the fabrication process of perovskite solar and further reduce their cost. A perovskite solar cell based on TiO_2 nanocrystalline and PbI_2 nanoparticles synthesized from old sealed acid battery was prepared and its photovoltaic performance as a function of annealing temperature was investigated. The optical properties and morphology of the perovskite films were correlated with changes in device performance. It was shown that device efficiency is strongly dependent on annealing temperature. Increasing annealing temperature of perovskite films from 60 ^oC to 100 ^oC led to agglomeration of perovskite island in perovskite films, thus increasing the efficiency of the cells from 1.59 % to 2.63 %. At the temperature of 100 ^oC, ITO/TiO_2/$CH_3NH_3PbI_3$/PEDOT:PSS/Au solar cell was found to have power

efficiency of 2.62 %.

9.2 Introduction

The photovoltaic properties of solar cells are strongly dependent on the fabrication process, hole transport layers, electron transport layers, nanoporous layers, interfacial microstructures, and crystal structures of the perovskite compounds. Especially, the crystal structures of the perovskite-type compounds, strongly affect the electronic structures such as energy band gaps and carrier transport, and a detailed analysis of them is mandatory [4]. Different parameters such as annealing temperature, solvent, and composition of precursor play significant role to achieving efficient perovskite solar cells [5, 6]. Thermal annealing and precursor composition play critical roles in crystallinity and morphology of perovskite thin films for efficient charge transport, thus improving the fill factor (FF) of the cells. So far little research has been done on thermal treatment to investigate its influence on photovoltaic performance of perovskite solar cells.

In this chapter, high-quality perovskite solar cells were fabricated in the same ambient conditions and annealed at different temperatures. A series of experiments correlating annealing temperatures to solar cell performance were conducted which highlights the critical importance of annealing temperature on achieving high performance perovskite solar cells with large fill factor ordinary conditions. The features of the solar cells were characterized by SEM, XRD, Photoluminescence (PL) and solar simulator equipped with keithly. By varying the temperature, PCE of 2.63% was achieved in ordinarily condition

9.3 Results and discussion

The heterojucntion perovskite solar cells compose of a conductive substrate, electron transport layer, absorber material, hole transport layer and metal

electrodes. In general, $Ti0_2$ is commonly employed to transports the electron and inhibits recombination. To accomplish a high efficiency, a $Ti0_2$ permeable film with a good pore size and thickness ought to be loaded up with the perovskite film. Moreover, to stay away from contact with Au anode specifically, the perovskite-sharpened $Ti0_2$ permeable layer is secured with a thin opening transporting layer (poly(3,4-ethylenedioxythiophene) polystyrene sulfonate). In particular, the opening transporting layer favors gap infusing to the Au anode and obstructing the electron exchange from the perovskite film to the Au cathode, which will prompt a high FF and $V_{oc.}$ Figure 9.1 demonstrates a device structure of the planar perovskite solar cells, (b) the energy diagram of each layer and (c) Low resolution photograph of the fabricated perovskite solar cell.

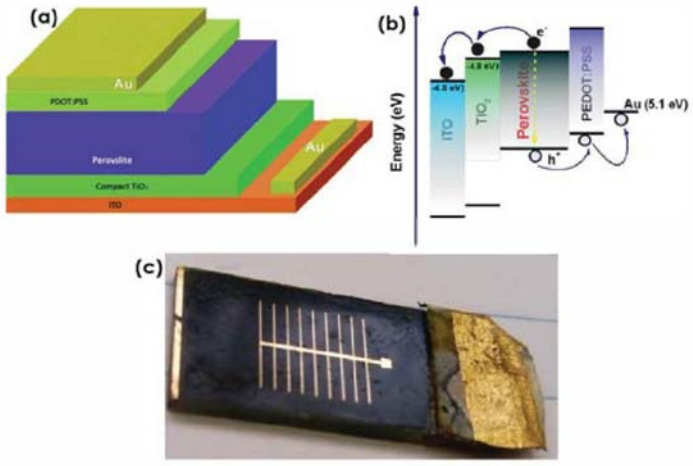

Figure 9.1: Device structure of the planar perovskite solar cells fabricated in this work. (b) The energy diagram of each layer. (c) Low resolution photograph of the fabricated perovskite solar cells

9.4 Structural analysis

Figure 9.2 shows the XRD pattern for ITO/TiO_2/$CH_3NH_3PbI_3$ perovskites solar cells as a function of annealing temperature. From the figure, we observe intense and sharp peaks at appropriate diffraction angles, ensuring a tetragonal phase with lattice parameters a = b = 0.8883 nm and c = 1.2677 nm. By

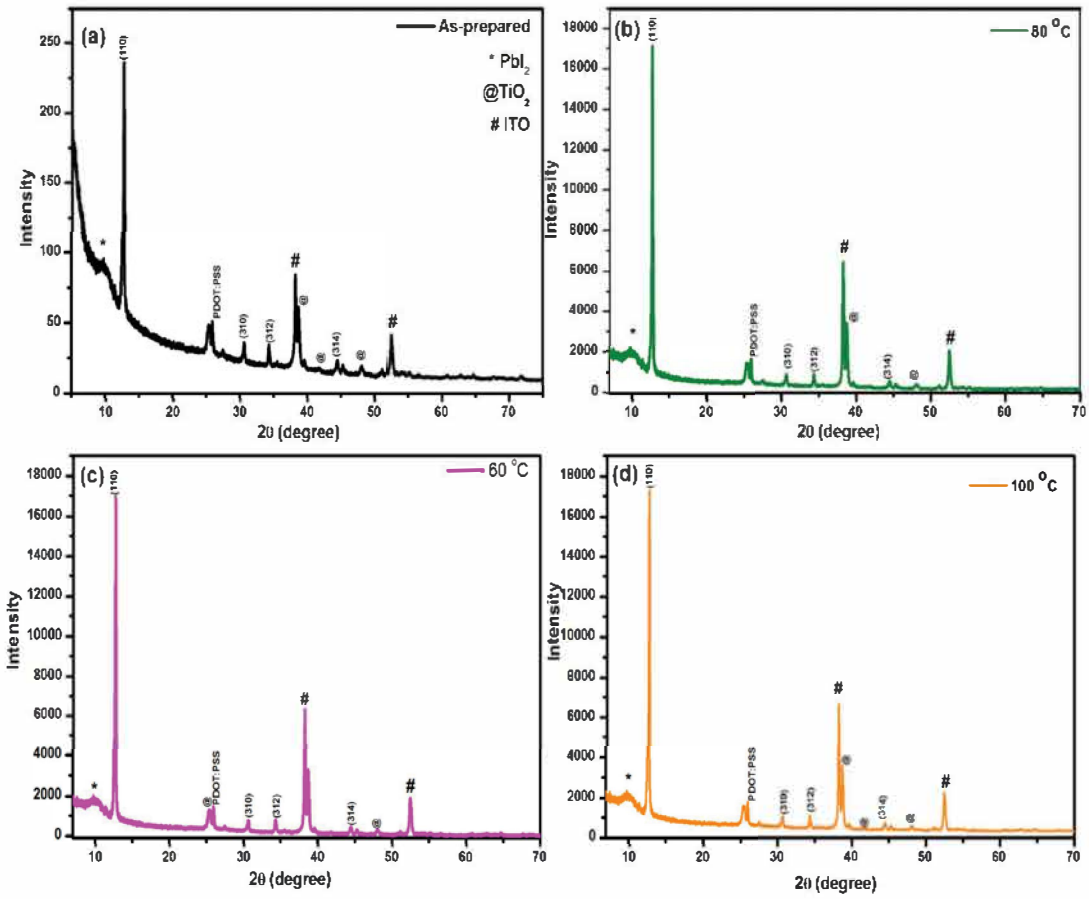

Figure 9.2: XRD patterns of the fabricated $CH_3NH_3PbI_3$ solar cells

looking at most intense peak (110), It is evident that the annealing temperature improves the crystalline nature of the perovskites material from 235.71 to 17403.36 a.u. The diffraction peaks for TiO_2 nanocrystalline are also appearing at 25.39 and 48.11 ^{0} corresponding to A(101) and A(200) planes, respectively. The diffraction peaks appearing at 26.08 ^{0} is assigned to a (020) plane of a hole transporting layer PEDOT:PSS [14]. A broad peak at around 10.20 ^{0} is indexed to PbI_2 residues, this is an indication that PbI_2 was not fully converted into $CH_3NH_3PbI_3$ during the synthesis process.

9.5 Surface Morphology

Figure 9.3 shows the evolution of perovskite structure as a function of annealing temperature. It is evident from the figure that perovskite islands becomes larger and furthermore internal structuring becomes more visible as the annealing temperature increase from 60 to 100 ^{o}C. It can be assumed that as the

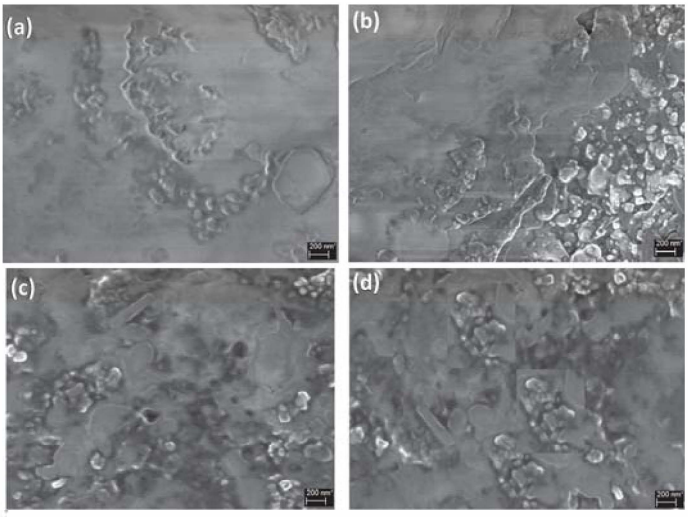

Figure 9.3: SEM images of TiO_2 films with deposited perovskite solution heat treated at a) As-prepared b) 60 ^oC, c) 80 ^oC, d) 100 ^oC

annealing temperature increases, the rate of perovskite crystallization is also increased. This can be further explained by the fact that high temperatures result in the rapid growth from a few nucleation sites leading to the formation of large crystalline islands and the associated large gaps in between, which improves surface quality and increase film uniformity with high surface coverage. In addition, larger grains and the compact morphology of the embedded perovskite films minimize the negative impact of oxygen and moisture, which favors the long-term stability of the corresponding films and devices [20]. This results suggest that there will be a superior contact between photo-active layer and top electrode which enhance optical absorption. Liang *et al* [21] pointed out that the surface quality of active materials can lead to improved photo-voltaic properties of the solar cell devices. This is in agreement with the results shown by XRD results. Figure 9.4 shows a top-view SEM image of the perovskite film capped with well distributed PEDOT:PSS hole transporting layer.

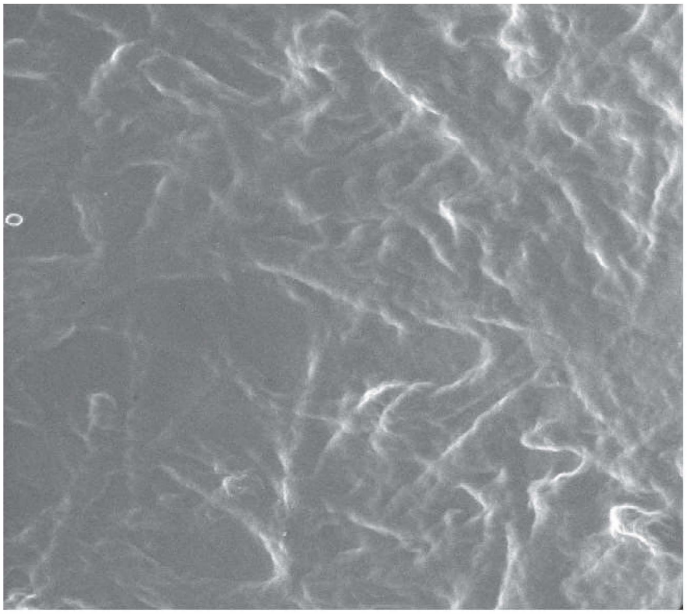

Figure 9.4: Top-view SEM image of perovskite capped with PDOT:PSS

9.5.1 Photoluminescent analysis

Figure 9.5 shows the photoluminescence spectra of the $MAPbI_3$ perovskite films coated on a TiO_2 film as an effect of annealing temperature. The photoluminescence peak at around 780 nm is entirely consistent with previous reports of emission from $CH_3NH_3PbI_3$ and the spectral position of the emission is consistent among all of the samples [22]. However, from the peak positions, it can be seen that there is a substantial quenching effect as the annealing temperature is increased this is known to be beneficial for photovoltaic solar cells [23, 24]. As temperature increases, peak intensity decreases because increased temperature improves diffusion length and charge transport properties of the active material thus enhancing recombination. Furthermore, this suggests that there are more phonon as the temperature is raised. Moreover, the slight redshift observed in the photoluminescence peak of the annealed films as compared to the as-prepared film, in fact, the observed redshift, which involve enhanced conjugation length, definitely implies an enhancement of the light absorption ability of $CH_3NH_3PbI_3$ with increasing temperature, similar results reported by Yao *et al* [25].

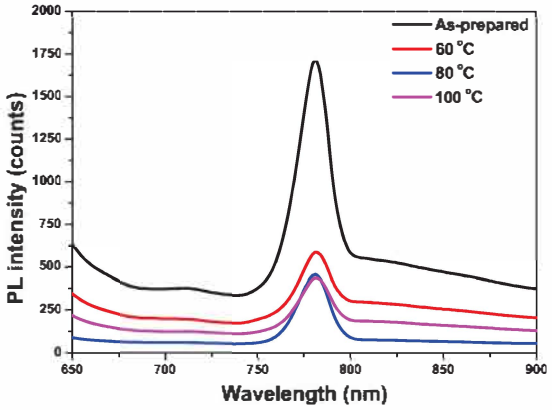

Figure 9.5: Pl spectra of perovskite $CH_3NH_3PbI_3$ on the TiO_2 films as a function of annealing temperature

9.6 Electrical characterization

Current–Voltage curves were recorded under AM 1.5 1000mW/m^2 simulated sunlight (Oriel Cornerstone, Newport) with Keithley 2400 series meter. The light intensity was previously calibrated using a standard silicon cell. Figure 9.6 present I–V characteristics of $MAPbI_3$ solar cells annealed at different temperatures. From the data, it is immediately apparent that device efficiency

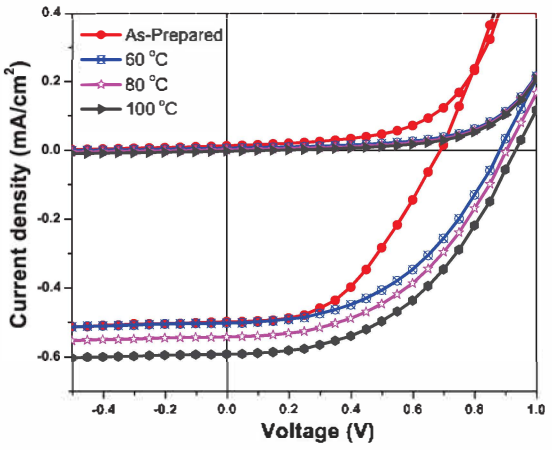

Figure 9.6: Current–Voltage characteristics of $MAPbI_3$ solar cells as a function of annealing temperature

is strongly dependent on annealing temperature and the results are correlated with the changes in optical properties and morphology presented in PL and surface section. Again it can be concluded that due to the superior contact, perovskite films annealed at 100 ^oC serve as a better active material that prevent parasitic looses compared to other films. The extracted photovoltaic parameters of TiO_2/$MAPbI_3$ solar cells as a function of annealing temperature are presented in Table 9.1. The highest efficiency was obtained for the solar cells annealed at 100 ^oC, which provided a photoconversion efficiency (η) of 2.62%, a short circuit current density (J_{sc}) of 0.54 mA/cm^{-2}, an open circuit voltage (V_{oc}) of 0.95 V and a fill factor of 0.47.

Table 9.1: Solar cell parameters as a function of annealing temperature.

Sample	V_{oc} (V)	J_{sc} (A)	FF	η (%)	P_{Max} (W)
As-prepared	0.7	0.49	0.456	1.59	0.16
Annealed at 60^oC	0.9	0.5	0.461	2.08	0.21
Annealed at 80^oC	0.9	0.54	0.476	2.33	0.23
Annealed at 100^oC	0.95	0.59	0.466	2.62	0.26

Apart from these solar cells parameters, I–V curves were further analyzed to determine series resistance (R_{series}) and shunt resistance (R_{shunt}) as junction properties. It is worth mentioning that an efficient solar cell should have a very low series resistance and high shunt resistance. Since planar solar cells are generally treated as single-junction diode, we can use the fundamental equation (9.6.1) of diodes to describe I–V curves for perovskites.

$$J(v) = J_{photo} - J_o \exp\left[\frac{-q(V + JR_s)}{k_B T}\right] - 1 - \frac{(V + JR_s)}{R_{sh}}, \qquad (9.6.1)$$

where J is the current density measured at the cell electrodes, V is the voltage measured across the cell, J_{photo} is the photogenerated current density, J_0 is

the reverse saturation current density, q is the elementary charge, R_s is the series resistance, R_{sh} is the shunt resistance, k_B is the Boltzmann constant, T is the absolute temperature, and n is the ideality factor. By neglecting the contribution R_{sh}, Equation 9.6.1 reduces to equation 9.6.2

$$ln(J_{photo} - J_o) = lnJ_o + \frac{q(V + JR_s)}{k_B T}, \tag{9.6.2}$$

From the first derivative of equation 9.6.2, R_s of the devices can be estimated as

$$-\frac{dV}{dJ} = R_s + \frac{nk_B T}{q(J_{photo} - J_o)}, \tag{9.6.3}$$

Therefore, equation 9.6.3 allow us to determine series resistance of our own perovskite solar cell devices. Shunt resistance could also be determined using equation 9.6.1, by neglecting the contribution of series resistance equation 9.6.1 reduces to equation 9.6.4.

$$-\frac{dV}{dJ} = \frac{1}{R_{sh}} + \frac{q}{nk_B T} J_o \exp \frac{q(V)}{nk_B T}, \tag{9.6.4}$$

The junction properties are calculated are presented in table 9.2. The low series resistance and high shunt resistance observed is entirely consistent with in all the solar cells and this represent the charge recombination of the solar cells as a function of temperature.

Table 9.2: Junction properties of perovskite cell as a function of annealing temperature

Sample	R_s (ohm.cm^2)	J_{photo}	J_0 mA/cm^2	R_{sh}(ohm.cm^2)
As-prepared	7142.8	0.498	0.456	41666
Annealed at 60 °C	2000	0.502	0.461	50000
Annealed at 80 °C	2000	0.542	0.476	50000
Annealed at 100 °C	2000	0.592	0.466	49 999

9.7 Conclusions

In summary, ITO/TiO_2/$MAPbI_3$/PEDOT:PSS/Au solar cells were fabricated in the same ambient conditions and annealed at different temperatures. The optical properties and morphology of the perovskite films were measured as a function of annealing temperature, and the results were correlated with changes in device performance. At the temperature of 100 ^oC, ITO/TiO_2/$MAPbI_3$/PDOT:PSS/Au solar cell was found to have power efficiency of 2.62 %. This is not the highest value reported in the body of perovskite solar cells but worth reporting since the solar devices were fabricated in the ordinary atmosphere. Therefore, it is expected that by better working environment the device can be improve.

References

[1] Du, Y, Cai, H., Wu, Y., Xing, Z., Li, Z., Xu, J., Huang, L., Ni, J., Li, J., Zhang, J., 2017. Enhanced planar perovskite solar cells with efficiency exceeding 16 percent via reducing the oxygen vacancy defect state in titanium oxide electrode, *Physical Chemistry Chemical Physics*, 19:13679–3686.

[2] Troughton, J., Hooper, K., Watson, T.M., 2017. Humidity resistant fabrication of $CH_3NH_3PBI_3$ perovskite solar cells and modules, *Nano Energy*, 39:60–68.

[3] Zhao, Y., Habibu, A., Javaid, S.S., 2015. Perovskite solar cells: Potentials, challenges, and opportunities, *International Journal of Photo energy*, (592308):13 pages.

[4] Ahmed, M.I., Zhu, K., 2014. Solution chemistry engineering toward high–efficiency perovskite solar cells, *Journal of Physical Chemistry Letters* 5:4175–4186.

[5] Oku, T., Matsumoto, T., Suzuki, A., Suzuki, K., 2015. Fabrication and characterization of a perovskite-type solar cell with a substrate size of 70 mm, *Coating* 5:646-655.

[6] Jung, H.S., Park, N.G., 2015. Perovskite solar cells: From materials to devices, *Small* 11(1):10–25.

[7] Huynh, T.P., Hoanq, T.T., Nguyen, P.H., Tran, T.N., Nguyen, T.V., 2009. Preparation of TiO_2 thin film using modified doctor-blade method for improvement of dyesensitized solar cell Conference Pap, *Conference Paper in Conference Record of the IEEE Photovoltaic Specialists Conference*. DOI: 10.1109/PVSC.2009.5411405 Source: IEEE Xplore

[8] Okamoto, Y., Suzuki, Y., 2016. Mesoporous $batio_3/TiO_2$ double layer for electron transport in perovskite solar cells, *Journal of Physical Chemistry* 120:13995–14000

[9] Shirke, B. S., Korake, P. V., Hankare, P. P., Bamane, S. R., Garadkar, K. M., 2011. Synthesis and characterization of pure anatase TiO_2 nanoparticles, *Journal of Materials Science: Materials in Electronics* 22:821-824

[10] Mahdi, E., Hamdi, M., Meor-Yusoff, M.S., Wilfred, P., 2013. XRD and EDXRF Analysis of Anatase Nano-TiO_2 Synthesized from Mineral Precursors, *Advanced Materials Research* 620:179-185

[11] Reyes-Coronado, D., Rodrguez-Gattorno, G., Espinosa-Pesqueira, M.E., Cab, C., de Coss, R., Oskam, G., 2008. Phase-pure TiO_2 nanoparticles: anatase, brookite and rutile, *Nanotechnology* 19(14): 10 pages

[12] Di Paola, A., Bellardita, M., Palmisano, L., 2013. Brookite, the Least Known TiO2 Photocatalyst, *Catalysts*, 3: 36–73

[13] Singh, T., Udagawa, Y., Ikegami, M., Kunugita, H., Ema, K., Miyasaka, T., 2017. Tuning of perovskite solar cell performance via low-temperature brookite scaffolds surface modifications, *APL Materials*, 5(1):016103

[14] Baibarac, M., Smaranda, I., Scocioreanu, M., Mitran, R.A., Enculescu, M., Galatanu, M., Baltog, I., 2015. Exciton-phonon interaction in PbI_2 revealed by Raman and photoluminescence studies using excitation

light overlapping the fundamental absorption edge, *Materials Research Bulletin*, 70:762–772

[15] Stavytska Barba M, Kelley M, 2010. Surface-enhanced Raman study of the interaction of PEDOT:PSS with plasmonically active nanoparticles, *The Journal of Physical Chemistry C* 14(14):6822-6830.

[16] Ledinsky, M., Loper, P., Niesen, B., Holovsky, J., Moon, S., Yum, J., De Wolf, S., Fejfar, A., Balli, C., 2015. Raman spectroscopy of organicinorganic halide perovskites, *The Journal of Physical Chemistry Letters*, 5:401–406.

[17] Quarti, C., Grancini, G., Mosconi, E., Bruno, P., Ball, J.M., lee, M.M., Snaithm, J., Petrozza, A., Angelis, F.D., 2014. The Raman spectrum of the $CH_3NH_3PbI_3$ hybrid perovskite: Interplay of theory and experiment, *The Journal of Physical Chemistry Letters*, 5: 279–284.

[18] Liang, Z., Zhang, Q., Wiranwetchayan, O., Xi, J., Park, K., Li, C., Cao, G., 2012. Effects of the morphology of a zno buffer layer on the photovoltaic performance of inverted polymer solar cells, *Advanced Functional Materials*, 22(10): 2194–2201.

[19] Pistor, P., Ruiz, A., Cabot, A., Izquierdo-Roca, V., 2016. Advanced Raman spectroscopy of methylammonium lead iodide: Development of a non-destructive characterization methodology, *Scientific Reports*, 6:35973.

[20] Wei, D., Ji, J., Song, D., Li, M., Cui, P.M., Li, Y.M., Mbengue, J.M.M., Zhou, W.M., Ning, Z.M, Park, N.G., 2017. A Tio_2 embedded structure for perovskite solar cells with anomalous grain growth and effective electron extraction, *Journal of Materials Chemistry A*, 5:1406–1414.

[21] Liang, Z., Zhang, S., Xu, X., Wang, N., Wang, J., Bi, Z., Xu, G., Yuan, N., Ding, J., 2015. A large grain size perovskite thin film with a dense

structure for planar heterojunction solar cells via spray deposition under ambient conditions, *Royal Society of Chemistry* 5: 60562–60569.

[22] Liu, X., Niu, L., Wu, C., Cong, C., Wang, H., Zeng, Q., He, H., Fu, Q., Fu, W., Yu, T., Jin, C., Liu, Z., Sum, T.C., 2016. Periodic organicinorganic halide perovskite microplatelet arrays on silicon substrates for room-temperature lasing, *Materials views* 3(1600137): 1–9.

[23] Tvingstedt, K., Malinkiewicz, O., Baumann, A., Deibel, C., Snaith, H.J., Dyakonov, V., Bolink, H.J., 2014. Radiative efficiency of lead iodide based perovskite solar cells, *Scietific Reports*, 4:6071

[24] Singh V, Arora S, Arora M, Sharma V, Tandoh RP, 2014. Characterization of doped PEDOT:PSS and its influence on the performance and degradation of organic solar cells, *Semiconductor Science and Technology* 29(045020): 8pp.

[25] Yao, Z., Wang, W., Shen, H., Zhang, Y., Luo, Q., Yin, X., Dai, X., Li, J., Lin, H., 2017. $Ch_3nh_3pbi_3$ grain growth and interfacial properties in meso-structured perovskite solar cells fabricated by two-step deposition, *Science and Technology of Advanced Materials* 18(1): 253–262.

Chapter 10

Conclusions

For the first time, highly pure and crystalline lead(II) iodide nanopowders were successfully prepared using two separate approaches on the anode and the cathode materials obtained from a depleted SLAG accumulator. The powders exhibit good thermal stability, which is needed for the final solar cell to be stable in use over varied environmental temperatures. The crystallite size was found to be 13.70, 11.59, 12.49 and 14.32 nm. SEM micrography revealed grain-like surface morphologies with grain sizes ranging between 1.5 and 3.5 μm. Spectral PL emissions were observed in blue region from 400 to 500 nm, attributed to the well-known excitonic band. The band gap was found to be in the range of 2.69 and 2.75 eV for both methods. The study of post-melting point annealing temperature and time on the crystallinity, phase transformation and thermal stability of PbI_2 nanoparticles was also conducted. Measurements confirmed that the high-purity synthesized product consisted of the rare 6R polytype form of PbI_2. This polytype is thought to hold considerable promise in perovskite photovoltaic applications because of its higher electron/hole mobility. Measurements using XRD, PL, TGA, DSCand FTIR techniques confirm that the as-synthesized hexagonal PbI_2 exhibits increased emission intensity with increased annealing time. Higher temperature phase transformations were confirmed by the presence of a single endothermic peak in DSC and the slight shift to lower wave numbers in FTIR, attributable to stretching vibrations. Thermal stability analysis confirmed

that the precursors exist as organic CH_3NH_3I and inorganic PbI_2 compounds, that are stable at much higher than ambient temperatures and therefore potential candidates for harsher climes. Furthermore, the link between lead iodide polytype precursors and the performance of the resultant methylammonium lead iodide perovskite devices was established. The 6R and 12R polytypes are known to arise from the synthesis route taken for the lead iodide precursor in the fabrication of perovskite. The performance of perovskite devices is shown to depend on the polytype used. The electrical, photoconducting and photovoltaic response of the final device appears to favor the use of the 6R precursor over the 12R polytype, suggesting that such devices would in general benefit from 6R lead iodide. In future studies it would be instructive to investigate the precursor structure of the lead halide precursors, particularly with respect to chlorine or bromine compounds, and even mixes. Furthermore, more detailed phototransient and impedance capacitance-voltage studies can be conducted. Finaly, ITO/TiO_2/$MAPbI_3$/PDOT:PSS/Au solar cells were fabricated in the same ambient conditions and annealed at different temperatures. The optical properties and morphology of the perovskite films were measured as a function of annealing temperature, and the results were correlated with changes in device performance.

At the optimal temperature of 100 ^oC, ITO/TiO_2/$MAPbI_3$/PDOT:PSS/Ag solar cell was found to have power efficiency of 2.62 %. This is not the highest value reported in the body of perovskite solar cells but worth reporting since the solar devices were fabricated in the ordinary atmosphere. It is important to mention that we have demonstrated to realize and characterize this kind of solar devices in ordinary atmosphere. Therefore, it is expected that by better working environment the device can be improve. This work outlines an attractive, low-cost synthesis method for an important component of perovskite solar cells from an abundance of discarded lead-acid accumulators

10.1 Scope for future work

A number of questions regarding perovskite solar cells from the synthesis and fabrication of perovskite devices have been addressed in this thesis. However there are still issues associated with perovskites that can be implemented on a widespread level. Firstly, some of the components of the photovoltaic degrade quickly in the presence of water. These perovskites are particularly sensitive to moisture, so they need to be very well sealed from the atmosphere to prevent premature degradation. In addition, the efficiency of perovskite solar, though relatively high, is uncertain. To determine the efficiency of a solar cell, a current-voltage (I-V) curve showing the current vs. the voltage is measured, and the point of maximum power is found. This power is compared to the incident light to determine the power conversion efficiency. In perovskite cells, however, the I-V curve changes depending on how quickly the voltage is varied and whether the voltage is scanned from high to low or low to high, hence the true performance of a perovskite photovoltaic in a long-term practical scenario unclear. Therefore, further studies needed to address the known challenges and hope to add to the body knowledge of perovskite solar cells. The outline of the proposed future work is as follows:

1. The nature of metal oxide-hybrid perovskite interface is identical to conventional p-n junction and free from complexities of semiconductor-electrolyte junction as in DSSC one may expect the positive effects of doping in metal oxide nanoparticles over the undoped metal oxide-perovskite junction. Therefore, influence of various dopants (trivalent or pentavalent) ZnO or TiO_2 matrix on the performance of hybrid perovskite solar cell can be important from scientific and technological point of view. Replacement of expensive hole transport material (Spiro-MeOTAD) with cheaper p-type metal oxide semiconductors (e.g. Cu_2 O or NiO) are matters of immediate scientific interest.

2. As indicated, the performance of perovskite solar cells depends highly on tuning different parameters of both Electron transporting layer (ETL), Active layer and Hole transporting layer (HTL). By controlling the concentration and depositing time we can be able to control for instance, a diameter and length of ZnO or TiO_2 nanorods. This will also help and expand the knowledge and the role played by morphology in this electron transport layer, or thickness of active layer.

3. It is difficult to deposit a large area of continuous perovskite film with the traditional methods described above and so other methods should be improved to prepare high-quality and large-area perovskite solar cells for commercial production in the future

10.1.1 Publications

1. T.D Malevu, B.S Mwankemwa, K.G Tshabalala, M Diale, R.O Ocaya, 2018. *Effect of 6R and 12R lead iodide polytypes on $MAPbX_3$ perovskite device performance*, Journal of Material Science: Material in Electronics,29(15):13011–13018

2. B Hosnedlova, M Kepinska, S Skalickova, C Fernandez, B Ruttkay-Nedecky, *T.D Malevu*, J Sochor, M Baron, M Melcova, J Zidkova, R Kizek, 2017. *A Summary of New Findings on the Biological Effects of Selenium in Selected Animal SpeciesA Critical Review*, International Journal of Molecular Sciences 18(10): 2209

3. T.D Malevu,RO Ocaya, KG Tshabalala, C, Fernandez. 2016. *Synthesis and characterization of high-quality PbI_2 nanopowders from depleted SLA accumulator anode and cathode*, Applied Physics A 122 (7), 1-7

4. T.D Malevu,RO Ocaya, KG Tshabalala. 2016. *Phase transformations of high-purity PbI_2 nanoparticles synthesized from lead-acid accumulator anodes*, Physica B: Condensed Matter 496, 69-73

5. T.D Malevu and R.O Ocaya, KG Tshabalala 2015. *Effect of post-melt annealing on phase transformations in high-purity PBI_2 nanoparticles from lead-acid accumulator anodes* Entech conference proceedings, ISBN: 978-605-9207-20-1

6. T.D Malevu and R.O Ocaya 2015. *An investigation of Nanostructure Morphology in the Zinc-air Cell Method as a Function of Electrolyte Concentration*, Int. J. Electrochem. Sci. Vol.10pp 4097-4104.

7. T.D Malevu and R.O Ocaya 2015. *Effect of Annealing Temperature on Structural, Morphology and Optical Properties of ZnO Nano-Needles Prepared by Zinc-Air Cell System Method*, Int. J. Electrochem. Sci., Vol. 10(2) pp. 1752-1761.

8. T.D Malevu and R.O Ocaya 2014. *Synthesis of ZnO Nanoparticles Using a Zinc-Air Cell and Investigation of the Effect of Electrolyte Concentration*, Int. J. Electrochem. Sci., Vol. 9(12) pp. 8011-8023.

9. T.D Malevu and R.O Ocaya 2014. *Poster presented at The 59th Annual Conference of the SA Institute of Physics (SAIP2014)*, University of Johannesburg. *Best M.Sc poster award.*

10. T.D. Malevu, N.F. Molefe, K.G. Tshabalala, and R.O. Ocaya. Title: Thermal stability of perovskite precursor. Article submitted to Materials Research Express 2018.

11. TD Malevu, BS Mwankemwa, KG Tshabalala, SV Motloung, RO Ocaya. Title: Effect of annealing temperature on TiO_2 nanocrystals for solar cell application. Article submitted to Journal of Physics and Chemistry of Solids. 2018

12. T.D. Malevu, B.S. Mwankemwa, K.G. Tshabalala, R.O. Ocaya, M. Diale. Title: Effect of annealing temperature on $MAPbX_3$ perovskite solar cell performance fabricated in ambient atmosphere. To be submitted.